Aus dem Universitätsklinikum Münster
Institut für Medizinische Biochemie
-Direktor: Prof. Dr. Volker Gerke-

ERM Proteins - Regulators of Mitosis?

INAUGURAL – DISSERTATION
zur
Erlangung des doctor medicinae
der Medizinischen Fakultät
der Westfälischen Wilhelms-Universität Münster

vorgelegt von Bissen, Philippe
aus Luxemburg
2019

Gedruckt mit Genehmigung der Medizinischen Fakultät der Westfälischen Wilhelms-Universität Münster

Dekan: Univ.-Prof. Dr. med. Mathias Herrmann

1. Berichterstatter: Univ.-Prof. Dr. Volker Gerke

2. Berichterstatter: Univ.-Prof. Dr. med. Hermann Pavenstädt

Tag der mündlichen Prüfung: 08.02.2019

Aus dem Universitätsklinikum Münster
Institut für Medizinische Biochemie
Direktor: Univ.-Prof. Dr. Volker Gerke
Referent: Univ.-Prof. Dr. Volker Gerke
Koreferent: Univ.-Prof. Dr. med. Hermann Pavenstädt

ZUSAMMENFASSUNG

ERM Proteins - Regulators of Mitosis?

Bissen, Philippe

Morphologische Veränderungen einer Zelle benötigen einen anpassbaren Zellkortex. Hierfür setzt das Zytoskelett sich aus selbst organisierenden Komponenten zusammen, welche neben den Bewegungsformen durch Bläschen, Lamellipodien und Lobopodien die Ausbildung von Mikrovilli, die Abrundung der Zelle in der Pro- und Metaphase und die Zytokinese ermöglichen. Für die Deformationen der Plasmamembran muss diese in dem darunterliegenden Zellkortex verankert sein. Anillin und ERM Proteine sind einige bekannte Verteter solcher verankernden Proteine.

Diese Studie untersucht mögliche Rollen der ERM Proteine in der Mitose. ERM Proteine stellen eine Proteinfamilie gebildet von ezrin, radixin und moesin dar.

Die Resultate zeigen nach Depletion der ERM Proteine keine signifikant erhöhte Zahl an Zellen mit unphysiologisch vermehrtem DNA Gehalt, was in diesen Zellen keine gravierenden Fehler in der Zellteilung vermuten lässt. Allerdings bringt eine detailliertere Analyse der Mitoseschritte in den ERM-defizienten Zellen im Vergleich zu ERM-haltigen Zellen einige Veränderungen zu Tage. Weniger Zellen beginnen die Zytokinese und parallel verbleiben mehr Zellen für eine längere Zeit in der Metaphase. Schließlich provoziert die fehlende Verbindungsfunktion der ERM Proteine kortikale Instabilitäten und Bläschenbildung unter dem Mikroskop. Ebenso stellt man eine kürzere Distanz zwischen den segregierenden Chromosomen und dem Zellkortex fest.

Kombiniert zeigen diese Resultate, dass ERM Proteine die Progression der Zytokinese positiv beeinflussen. Diese Wirkung basiert entweder auf kortikalen Interaktionen und/oder auf der Ebene der Spindelorganisation, welche die chromosomale Segregation reguliert.

Tag der mündlichen Prüfung: 08.02.2019

ERKLÄRUNG

Ich gebe hiermit die Erklärung ab, dass ich die Dissertation mit dem Titel:

ERM Proteins - Regulators of Mitosis?

in der/im (Klinik, Institut, Krankenanstalt):

Institut für Medizinische Biochemie

unter der Anleitung von:

Prof. Dr. V. Gerke

1. selbständig angefertigt,
2. nur unter Benutzung der im Literaturverzeichnis angegebenen Arbeiten angefertigt und sonst kein anderes gedrucktes oder ungedrucktes Material verwendet,
3. keine unerlaubte fremde Hilfe in Anspruch genommen,
4. sie weder in der gegenwärtigen noch in einer anderen Fassung einer in- oder ausländischen Fakultät als Dissertation, Semesterarbeit, Prüfungsarbeit, oder zur Erlangung eines akademischen Grades, vorgelegt habe.

Münster, den 21.April 2018

Ort, Datum

Philippe Bissen Bissen Ph.

Name/ Unterschrift

Contents

1 Introduction

1.1 ERM proteins

THE proteins of interest in this study are ezrin, radixin and moesin. All three together form a family of membrane-associated proteins, the ERM family [1]. They are linker proteins between the plasma membrane and the actin cytoskeleton [2]. Another member that was later discovered is merlin (moesin-ezrin-radixin-like protein) [3, 4].

ERM proteins (ERMs) and their interactions will be introduced in this first section. The second section will deal with the actin cyoskeleton, in particular the cortical actin cytoskeleton, before the third and last section will highlight the potential role of ERMs in mitosis.

1.1.1 The structural composition of the members of the ERM family

The amino acid structure of ERMs is very closely related and implies thereby a similar size. A conserved amino-terminal FERM (Four point 1, Ezrin, Radixin, Moesin) domain indicates their membership in the band 4.1 superfamily [5–7]. ERM proteins have respectively a size of 80kDa [8], 82kDa [9] and 77kDa [6]. Their calculated molecular mass is $\sim 69\,kDa$ [5, 7], with the difference due to their highly charged nature. At their carboxy-terminal end 34 amino acid residues are conserved [10]. This carboxy-terminus is linked to the amino-terminus by an α-helical domain [11].

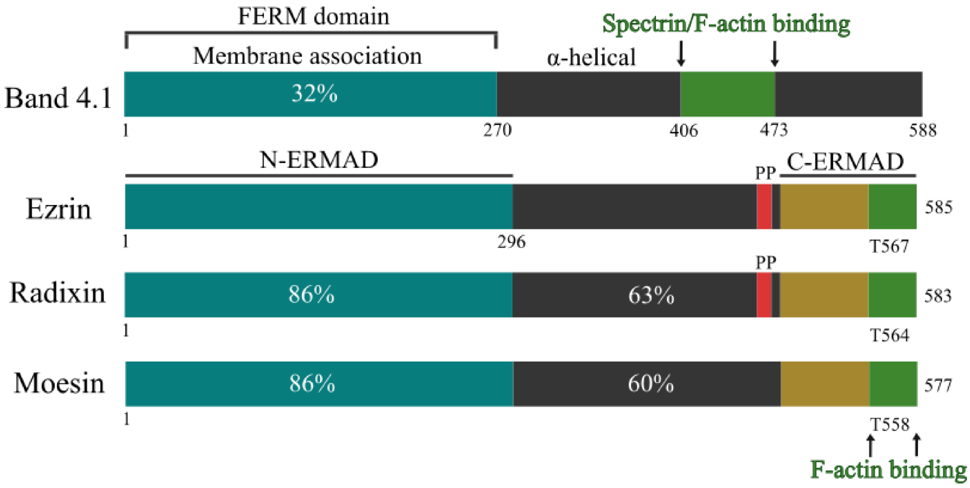

Figure 1.1: Schematic structure of the ERM family.
The sequence identity of radixin, moesin and Band 4.1 compared to ezrin is shown. Ezrin and radixin present a region rich in prolines (PP), while moesin does not. Image modified from [12].

The schematic structure, shown in Figure 1.1, delineates further characteristics of the domains that are needed to understand the function of ERMs.

The FERM domain consists of 300 amino acid residues that form three lobes (F1, F2 and F3) in the shape of a clover structure [12–14]. F1 (residues $4-82$) is built of a β-sheet and an α-helix, F2 (residues $96-195$) of 5 helices with interactions between helices B and C and F3 (residues $204-297$) of a β-sheet and a long helix (residue numbers specific for moesin) [13]. Each of the cloverleaves is structuraly similar to other proteins. F1 shows resemblance to ubiquitin [15], F2 to acyl-CoA binding protein [16] and F3 to phosphotyrosine binding (PTB), pleckstrin homology (PH) and Enabled/VASP homology 1 (EVH1) domains [17] [13]. Importantly, the FERM domains of ERM proteins have binding sites for membrane lipids and proteins [18].

Located between the C- and the N-terminal regions is a central α domain of ~ 200 residues [19]. In the C-terminal domain, each ERM contains a phosphorylatable threonine residue. In ezrin, it is at Thr^{567}, in radixin at Thr^{564} and in moesin at Thr^{558} [20, 21]. The C-ERMAD (C-terminal ERM Association Domain) contains $\sim$ 100 residues [19] of which the last 6 residues of the conserved 34 are required for F-actin interaction [10].

The closely related structures indicate the emergence of ERMs by gene duplication within the vertebrates. Thus, they might have similar and/or redundant roles (see Table 1.1) [12].

Conservation of N- and C-terminal domains		
Protein	**N-terminal (in %)**	**C-terminal (in %)**
Ezrin	100	100
Radixin	86	60
Moesin	85	58

Table 1.1: Conservation of N- and C-terminal domains.
Image amended from [19].

Conformational Autoinhibition:

The finding that ezrin and moesin are capable of homo- and heterodimerizing [22] led to the discovery that the N-terminal domain can bind with high affinity to the C-terminal domain. This led to the nomenclature N-ERMAD (N-terminal ERM Association Domain) and C-ERMAD comprising the 80-carboxy-terminal residues required for the binding [13, 19]. This interaction between the N- and the C-terminal domains masks the binding sites for other proteins and results therefore in the dormant or autoinhibited form of ERM proteins (see Figure 1.4) [19, 23].

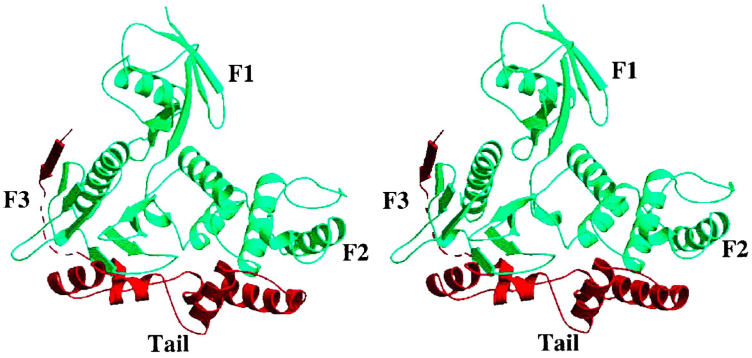

Figure 1.2: FERM/tail complex in the overall crystal structure.
Image amended from [13].

The C-ERMAD consists of a β-strand and four major α-helices, capable of masking parts of the F2 and F3 domains (see Figure 1.2) [13]. To achieve the dormant form, residues $488-494$ extend the second β-sheet of F3 in a way that an antiparallel β-strand alongside strand 5 of F3 is formed. Moreover residues $495-501$ connect to residues $502-577$ in a way that the C-terminal tail is folded and aligns next to 4 major helices (named A, B, C and D) also 2 short helices. These 2 short helices interact with F2 and F3 of the N-ERMAD (residue numbers specific for moesin). Finally 36 % of the tail surface takes part in the autoinhibition and covers 2700 $\mathring{A}$ of the FERM domain [13]. Interestingly the reaction between the amino- and the carboxyterminus has a favorable enthalpy (ΔH) and an unfavorable entropy (ΔS), so that only 1 molecule in $\sim$ 20.000 would adopt the open conformation without being activated. The macroscopic stability of C-ERMAD is given by the α-helices

αC and αD. A nuclear magnetic resonance (NMR) study has proved that the FERM domain is independantly bound by helices of C-ERMAD [24].

The intramolecular autoinhibited form of ERM proteins resides in the cytosol [25]. The molecule changes into the active open conformation after a sequence of two activation steps. The first step is the recruitment and binding to membrane regions with phosphatidylinositol-4,5-bisphosphate ($PI(4,5)P_2$)[26, 27]. This establishes a recruitment of the open form of ERM proteins to the membrane [25]. Secondly the carboxy-terminal threonine residue (Thr^{567} in ezrin, Thr^{564} in radixin and Thr^{558} in moesin) is phosphorylated [28] after its placement near Rho kinase or protein kinase CΘ [12].

Two evolutionarily conserved residues in the 4.1 protein and in the ERMs also enable the direct association with microtubules [29]. Furthermore, the membrane-associated ezrin could locally modulate cortical organization and contractility, because its diffusion at the membrane is quite slow [30].

1.1.2 Interaction partners

The manifold functions of ERM proteins (see 1.1.3 below) require numerous interaction partners (see Table 1.2).

For their activation several kinases are able in vertebrate cells to phosphorylate the respective regulatory threonine (Thr^{567} in ezrin, Thr^{564} in radixin and Thr^{558} in moesin), including Rho Kinase (ROCK), Protein Kinase C (PKC) α, PKCθ, NF-kappa-B-inducing kinase (NIK), mammalian STE20-like protein kinase 4 (Mst4) and lymphocyte-oriented kinase (LOK) [21, 31–34].

In leucocytes it could be shown that ERMs function both upstream and downstream of Rho GTPases (see Figure 1.3) [35]. Rho GDP dissociation inhibitor (Rho GDI) inhibits the activation of G proteins belonging to the Rho family by building a complex with the isoprenyl group of the GDP-bound form. ERM proteins can regulate Rho proteins through direct binding or by binding Rho GDI via the FERM domain. Thereby the inhibitory regulation is reduced and Rho family members are activated [36, 37]. Moreover, ERMs are capable of binding stimulatory GDP/GTP exchange proteins for Rho family members such as Db1. Db1 can bind to FERM but not to an ERM in a complex with Rho GDI. Rho GDI even displaces Db1 from ERMs [38]. ERMs also work as protein kinase (A) anchoring proteins (AKAP). The type II A-kinase regulatory subunit, called R_{II}, comprises a binding region to ERMs between the FERM and the C-terminal domain. In this α-helix 14 amino acids build an amphipathic helix, essential for R_{II} binding [39]. Furthermore, direct inhibition of RhoA was shown to dramatically reduce the activity of ERMs. ERM proteins are thereby regulated downstream Rho GTPases as well [26].

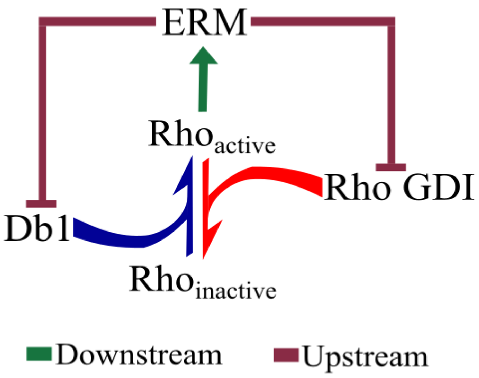

Figure 1.3: ERM proteins function both upstream and downstream of Rho GTPases. Image based on [35].

In vertebrates ERMs can also be phosphorylated at other residues. CDK5 is capable of phosphorylating Thr^{235} in ezrin, which lies topologically directly opposite Thr^{567}. Thereby ezrin also becomes activated [13, 40]. Tyrosines 145 and 353 in ezrin can also be phosphorylated through multiple kinases, such as EGF receptor [41]. The unconserved Tyr^{353} that only exists in ezrin is phosphorylated in B cells to couple JNK signaling with the BCR signalosome. This role of Tyr^{353} is independant of Thr^{567} [42]. For Tyr^{145} no role has been described until today.

In Drosophila the sterile 20-like kinase (SLK) seems to be responsible for the phosphorylation of the important Thr residue [43–46]. Studies tested mutations in the threonine residue of ERMS. TxxxD (for moesin T559D) should mimic the phosphorylation and TxxxA (for moesin T559A) should abolish the phosphorylation. The transfection with TxxxD was shown to be capable of rescuing an insertion mutation in the moesin gene (*P{lacW}l(1)G0323*), which disrupts the function of moesin [47]. Two other studies obtained different results, but Fehon et al deduced from another study [48] that C-terminal-tagged GFPs could interfere in the intramoleculare binding. That way studies that could not reproduce the rescue with TxxxD should not rely on results obtained with C-terminal tagged GFPs [49].

ERM proteins can bind to juxta-membrane cytoplasmic domains of integral membrane proteins with their FERM domain. These include CD43, CD44 and intercellular adhesion molecule (ICAM)-2 [50]. The binding of CD44 happens in a PI$(4,5)$P$_2$-dependent manner [28]. Another binding of ERMs to membrane proteins can be observed for the Na^+, H^+-exchanger (NHE)1. NHE1 has 12 transmembrane domains and the FERM domain binds to the positively charged carboxy-terminal cytoplasmic tail [51].

Proteins binding to FERM domains
Membrane proteins
1.Intercellular adhesion molecule-1 (ICAM-1)
2.Intercellular adhesion molecule-2 (ICAM-2)
3.CD44
4.CD43
5.L-selectin
6.CD95 (APO-1/Fas)
7.Na^+, H^+-exchanger 1 (NHE1)
8.P-glycoprotein (ERM)
9.Multidrug resistance protein 2 (MRP2) (*radixin)
10.$Na^+K^+2Cl^-$ cotransporter (NKCC2) (*moesin)
Scaffold proteins
1.NHERF1 (EBP50)
2.NHERF2
Rho-related proteins
1.Rho-GDP-dissociation inhibitor (Rho-GDI)
2.Db1

Table 1.2: Proteins binding FERM domains
Image adapted from [25]

The ERM-binding phosphoprotein 50 (EBP50), which comprises 357 residues, is widely distributed, in particular in liver, kidneys, small intestine and placenta. The protein presents two $\sim$ 90-residue repeats in the amino-terminal half of the molecule, that show 74 % identity and are called PDZ domains (named after the first three proteins that were found with such a domain: Post synaptic density protein, Drosophila disc large tumor suppressor and Zonula occludens-1 protein). The latter domains are involved in the formation of multiprotein complexes at the plasma membrane [52]. The rabbit scaffold protein NHE-RF (NHE regulatory factor) shows 84 % identity to human EBP50 [53]. Dormant ERMs can be activated to bind EBP50/NHERF through their N-ERMAD and F-actin through their C-ERMAD, linking thereby the plasma membrane to the cytoskeleton [54]. NHERF and ERMs colocalize in membrane ruffles, microvilli and filopodia in cells [55] and NHERF2 (also called TKA-1, E3KARP or SIP-1) is present in podocytes maintaining the intact epithelium [56]. NHERF and NHERF 2 have 52 % sequence identity [57]. While the first PDZ domain of the NHERF family binds to proteins with D-S/T-x-L at their C-terminus, including CFTR (Cystic Fibrosis Transmembrane Regulator) and purinergic P2Y1 receptor, the second PDZ domain can also bind to CFTR with lower affinity [58]. Interestingly scaffold proteins like NHERF family members are conformationally regulated by intramolecular associations as it is the case for ERMs [59, 60].

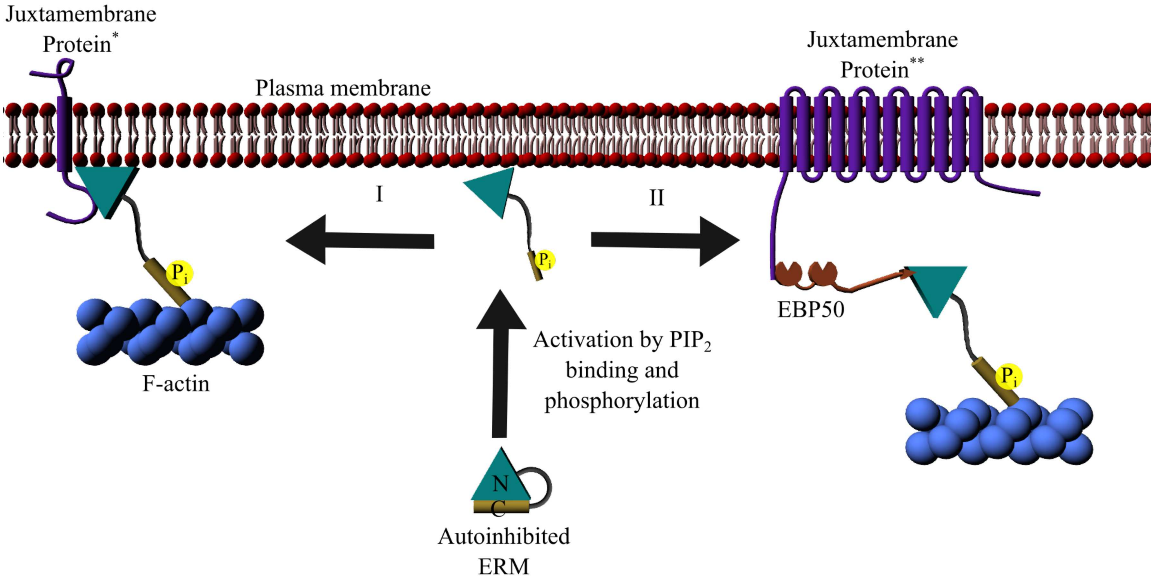

Figure 1.4: ERM proteins are linkers between the plasma membrane and the actin cytoskeleton.
After their activation through PI(4,5)P_2 binding and phosphorylation, ERMs either bind the membrane directly **(I)** or indirectly (**II**) to the cell cortex. Examples for the juxtamembrane proteins in both binding scenarios are *****) CD44, ICAM-1, NHE-1, Syndecan-2 and ******) NHE-3, CFTR, PDGF-R, Podocalyxin. Image adapted from [12].

In addition to microvilli and membrane ruffles, ERM proteins are also enriched in cell–cell junctions and cleavage furrows of dividing cells [61–63].
ERMs are also implicated in the hedgehog signaling [49, 64] and in membrane receptor signalling [65], either through direct interactions with membrane receptors or through scaffold protein binding.

1.1.3 Function in cells & physiology

An organism that is often used to study the function of ERMs is Drosophila melanogaster because it has a single ERM protein called dmoesin [66].
In other organisms each organ and tissue has its specific ERM expression profile (see Table 1.3).
Studies could show that ezrin is prominantly expressed in the intestines and in the stomach. Also the renal proximal tubules and corpuscules express ezrin [61, 67]. Knockouts of ERMs are only lethal for ezrin and these mice die before weaning. A reduction of ezrin expression in the apical microvilli in the retinal pigment epithelium and in the Müller cells leads to substantial retardation in the development of photoreceptors [68]. Ezrin conditional knockout mice showed phenotypes including achlorhydria [69], a dysregulation of phosphate and calcium homeostasis [70] and intrahepatic choleostasis [71].

In physiology the secretion of gastric acid requires ezrin. On the apical canalicular membranes ezrin is predominantly expressed in parietal cells [72]. Histamine stimulation leads to PKA-mediated phosphorylation of ezrin at Ser^{66}. Then ezrin interacts with ACAP4, an Arf-GTPase-activating protein. The result is membrane fusion between intracellular tubulovesicles containing gastric proton pumps and the apical plasma membrane [73].

Moesin shows high expression levels in the lungs, spleen, kidneys and in endothelial cells and lymphocytes [61, 67]. Chemokines are capable of inducing rapid dephosphorylation of ERMs and thereby trigger a rapid loss of microvilli and polarization [74]. Moesin has a non-redundant role in the egress of both T and B cells from lymphoid organs. It is the major protein to regulate cell migration and cell shape changes in lymphocytes [75]. Neutrophils were also shown to need moesin for the regulation of transmigration and chemotaxis. Constitutively active moesin masks through its FERM domain the PH/DH domain of GEFs, so that Rho GTPases (Rac, RhoA, and Cdc42) can't be activated. To initiate directed cell polarization and migration myosin phosphatase abolishes the moesin-mediated masking at the would-be leading edges (see also Chapter 1.2.3) [76].

Radixin was originally found in the liver [9] and later to be the major ERM protein in hepatocytes [77, 78]. It is also the major ERM protein in cochlear stereocilia [79]. A further role was shown through a link to $GABA_A$ receptors in the hippocampus [80] and therefore in abilities like reversal learning and short-term memory [81].

ERM Proteins expressed in Cultured Cell lines

Cell line	**ezrin**	**radixin**	**moesin**
Epithelial cells			
Caco-2 (human intestinal epithelial cells)	+++	+++	-
HT-29 (human colon adenocarcinoma)	+++	+	++
LLC-PK1 (porcine kidney epithelial cells)	+++	+++	+++
MDCK (dog kidney epithelial cells)	+++	+	++
HepG2 (human hepatocellular carcinomas)	+++	+++	++
A431 cells (human squamous carcinomas)	+++	+	++
Fibroblasts			
L cells (mouse fibroblasts)	+++	+++	+++
NIH 3T3 (mouse fibroblasts)	+	+++	+++
Neuronal cells			
PC12 (rat pheochromocytomas)	++	+	+++
Lymphoid cells			
CCRF-CEM cells (human lymphoid cells)	+++	++	+++

Table 1.3: ERM protein expression
Image adapted from [25]

In vertebrate embryos the polarity is established by silencing Hippo signaling in the nucleus [82]. In the course of these events a Par complex phosphorylates ezrin that subsequently inactivates Hippo, thereby supressing the pluripotency gene Oct4 by different molecular interactions [83, 84].

1.2 The cell cortex

1.2.1 Cortex - a complex construct

In the early 20^{th} century the underlying structures of the cell membrane were already the core of research studies, which led to the description of an hyaline cortex of amoebae in 1926 [85], which was thereby the first cell cortex to be mentioned. Another name for the cell cortex that came up is membrane skeleton [86]. Research needed time until the 1970s to acquire some evidence that the underlying filaments are built of actin [87, 88] and that the cortex constitutes a cross-linked network of actin, myosin and associated proteins. Later, electron microscopy showed an actin filament [filamentous actin (F-actin)] network adjacent to the plasma membrane, which has mesh sizes ranging from 20 to $250\,nm$ and a thickness of about $50 - 100\,nm$ [89, 90], although the latter size calculation could be falsified by the electron microscopy method, as this leads to distortions [91].

1.2.2 Cortex in motion

The actin filament network implicates many proteins that provide the cortex with its abilities. Myosin motor proteins enable the filaments to move and actin binding proteins such as cofilin and gelsolin control the assembly and disassembly of F-actin. Furthermore, cross-linkers between the cortex and the plasma membrane such as the ERM proteins and cross-linkers between the actin filaments themselves such as fascin help organize the structure of the cortex. The next lines describe the roles and interactions of these protein families.

Today two major distinct pathways of actin nucleation are known, the formin (m)Dia1/Diaph1 and the Arp2/3 (actin-related protein 2 and 3) complex dependant one [92], which also regulate cortical actin. Formin-nucleated filaments represent $10\,\%$ of F-actin and are on average 10 times longer than those nucleated by Arp2/3. Diaph1 accelerates growth at the barbed ends [also called positive (+) end], while the Arp2/3 complex prevents actin disassembly from the pointed end [also called minus (-) end], so that there is a constant growth of filaments at their barbed ends and at the pointed ends the filaments shrink [93]. The same author was recently able to show that the association of actin filaments into greater actin patterns from vortices to stars and asters is driven by the nucleation of the Arp2/3 complex and not by myosin II (see Figure 1.5) [94].

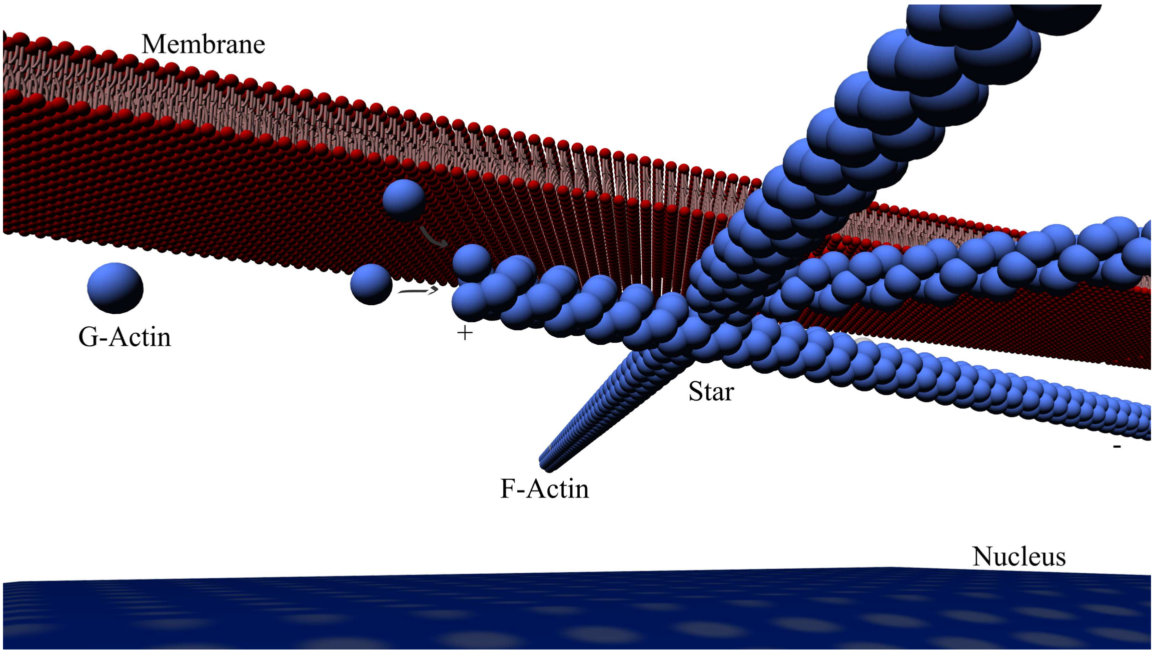

Figure 1.5: Sketch of the actin cortex.
The bilayer is stabilized by underlying actin patterns [94]. The association of F-actin into greater actin patterns is driven by nucleation through the Arp2/3 complex.

There exist two distinct mechanisms for the formation of macromolecular structures (see Figure 1.6): Self-assembly is the physical association of molecules into an equilibrium structure [95], whereas self-organization represents a physical molecular interaction resulting in a steady-state structure with constant input of energy [96].

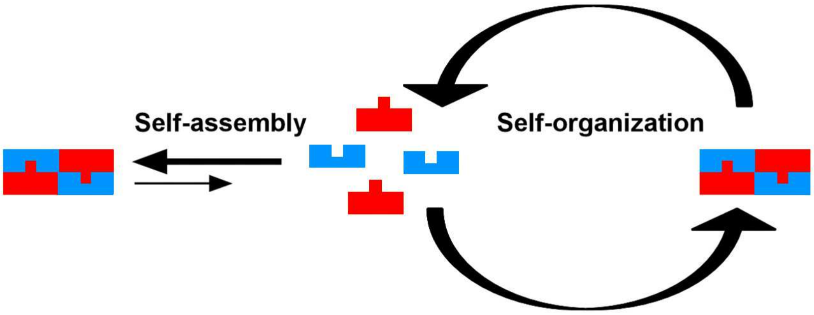

Figure 1.6: The mechanism of self-organization.
Image modified from [97].

The cortical actin cytoskeleton forms by self-organization (see Figure 1.6) [97–99] with an established physical model [100]. The cortical F-actin is highly dynamic with an assembling-disassembling half-time of about $T_{1/2} \sim 25\,s$ [101]. Myosin influences the turnover of actin by regulating the disassembly of actin filaments into shorter filaments and globular actin monomers [101, 102] and α-actinin favoring its assembly [103]. Other cell cortex proteins such as gelsolin and cofilin lead to a reduced tension, thus a thinner cortex [104]. In comparison the drosophila turnover rate of myosin II is of about $\sim 10\,s^{-1}$ [105]. The cross-link turnover rate between

actin and myosin determines the duration of stresses in the cortex [106] and when the cross-links are released, the motor proteins can influence the filaments again to slide past one another [107]. Furthermore, there have been two different subpopulations of F-actin identified: one with formins bound to their barbed ends and one population with free barbed ends, which shows a faster turnover, a greater abundance and according to the hypothesis of the author, shorter filaments [107]. That way cofilin could sever formin-capped filaments and consequently replenish the population with free barbed ends [107].
Physical property investigation showed that the cortex has both elastic and viscous characteristics: The lipid bilayer of the plasma membrane, for which the actin cortex provides resilience against deformation [108] and the 'cortex stiffness', which represents the elastic response to deformation by indentation [109]. That way the polymer network can be stretched and responds elastically while the detachment of actin cross-linkers provides viscous characteristics. Moreover the cortex enables the cell to oppose intracellular osmotic pressure [110].
Research was able to find several proteins that bind the membrane to the barbed ends of actin filaments, among others gelsolin, villin [111, 112], ponticulin [113] and the ERM family (see Chapter 1.1 above). The ability to cap the barbed ends led to the name capping proteins.

Analyses of F-actin and myosin have revealed much more of their interaction.
F-actin builds the structural matrix upon which the myosin motors move, using hydrolysis of ATP. These myosin II motors assemble into a multimeric complex to generate sustained gliding of actin filaments past one another[114–116]. Therefore contraction of actin networks by myosin II needs F-actin cross-linkers in cells, such as filamin A or fascin [117–120]. Large forces by myosin II can only be exerted when these cross-links exist [121]. Contractility defines the pulling by myosin filaments on neighbouring actin bundles without significantly changing the sizes of the bundles [122]. The traction of myosin II on actin anchored by filamin A causes internal stress, resulting in a stiffening of the network by more than two orders of magnitude [123] with a force per motor bundle estimated at $\sim 1\,piconewton$.
Depending on the timescale of deformations the membrane and the underlying cortex generate different physical behaviors; rapid deformation (seconds) leads to high stress in the actomyosin network upon which the cortex will store energy and react elastically. But long-term deformations ($>$ tens of seconds) allow the restructuring of F-actin and the turnover of crosslinkers, because the energy in the cortex will dissipate in a fluid-like manner, giving it a viscous property [124]. These viscoelastic properties are influenced by: 1) Crosslinks rigidifying the cortex and increasing the stiffness of the system [125–127]. 2) Myosin II motor activity increasing stiffness in

highly and fluidity in poorly crosslinked networks [128]. 3) Increasing turnover rates of the cortical components also increasing fluidity [129].
The hexamer formed by myosin II consists of two heavy chains (MHC), two essential light chains and two regulatory light chains (MRLC) (reviewed in [130]). The N-terminal globular domain of the heavy chain is called 'head region', which contains actin and ATP binding sites and whose ATPase activity is coupled to the cyclic detachment and attachment of myosin to F-actin. After the hydrolysis of ATP, one phosphate (P_i) is released, which provides myosin with the energy for the 'powerstroke', the conformational change that induces actin movement (see Figure 1.7). The dissociation of ADP and the replacement by ATP detaches the motor protein from actin (see Figure 1.7) [131]. Via the C-terminal domain myosin II can form homodimers through α-helical coiled-coil domains [130].

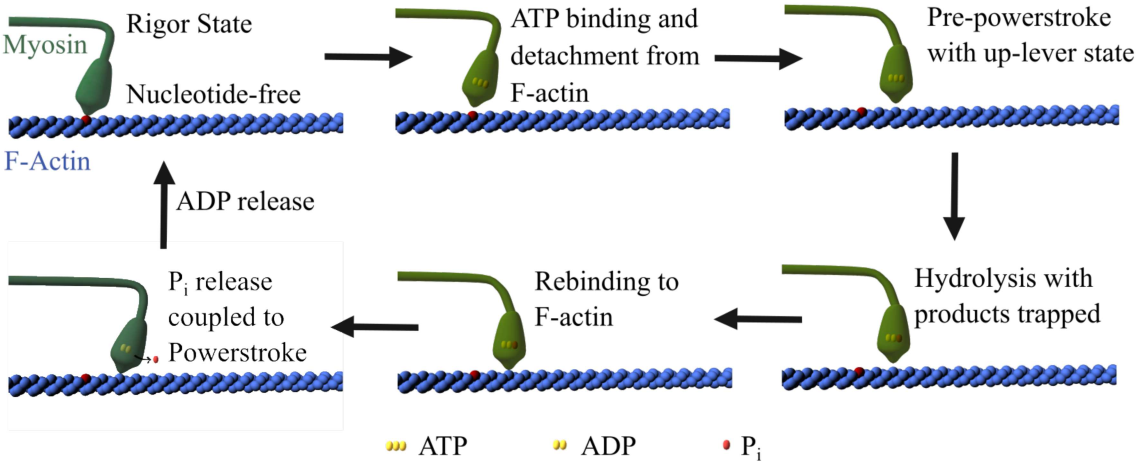

Figure 1.7: Myosin 'Powerstroke'.
The red stained actin marks the starting spot for myosin interaction on the actin filament. While the myosin head is stained in light green when it is weakly- or un-bound to actin, the head is colored in dark green in its force-generating state. Image modified from [132]

To fulfill its contractile activity the tail-to-tail associated myosin II hexamers can assemble into bipolar minifilaments [133, 134].
The activation of Myosin II occurs through phosphorylation of the MRLC at highly conserved residues (Thr^{18} and Ser^{19} [135]) by multiple kinases such as ROCK (Rho-associated coiled-coil containing kinase), citron kinase, MRCK (myotonic dystrophy kinase-related Cdc42-binding kinase) or MLCK (myosin light chain kinase) [136]. A change in the heavy chains (MHC) head-to-tail interaction is induced by the phosphorylation of the MRLC. The resulting extended conformation allows F-actin binding, ATPase activity and minifilament assembly [137, 138]. There exist other observed regulation mechanisms such as the phosphorylation of the heavy chains by MHCK in *Dictyostelium* [139] or by casein kinase II and protein kinase C (PKC) in mammalian cells [140–142].

Three deformation types of the cell cortex will be discussed in the following sections.

1.2.3 Deformation I: Locomotion

In 1970 fibroblasts were first filmed during migration to study their function [143]. Since then three different movement types depending on the cell type and the substrate have been discovered. The next chapters will describe these types.

1.2.3.1 Lamellipodia/Filopodia

'Lamellipodia are broad, flat, sheet-like structures,whereas filopodia are thin, cylindrical, needle-like projections' [144] with their abundant content being actin and associated proteins. They are capable of extending in three dimensions around the cell. Two phases can be distinguished: 1) the protrusion of the leading edge and 2) the retraction of the rear (reviewed in [144]). The retraction of the tail relies on myosin II, being present in stress fibers (reviewed in [145, 146]), bundles built of $\sim 10-30$ actin microfilaments [147]. Mainly α-actinin holds these bundles together [146, 148]; it shows a periodic pattern along the actin fibers, alternating with the localization of myosin II [149] and tropomyosin [150]. The formation of stress fibers is triggered by activation of the small GTPase RhoA [151]. The activation of its downstream effector ROCK can maintain this activation [152]. As the inhibition of ROCK significantly reduces stress fiber tension [153], a main role in contractility of the rear can be assigned to the phosphorylation state of myosin II controlled by the RhoA-ROCK pathway [154]. Not only myosin II has to be organized for the regulation of contractility, but also actin plays its role (see Chapter 1.2 above). Even if constitutive activation of ROCK also results in the formation of stress fibers, this pathway cannot fully replace the features of the RhoA induction. Fully functional stress fibers are built only when GTP-bound RhoA activates Dia by disrupting the intramolecular interactions of the effector. ROCK-induced actin fibers are then rebuilt after the triggering by the active Dia [155].

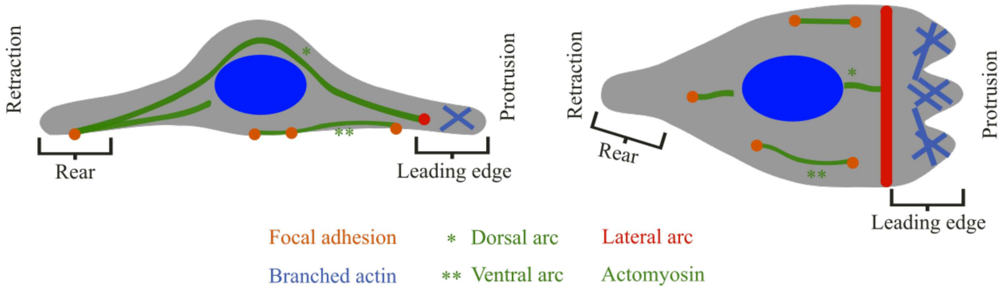

Figure 1.8: Lamellipodial driven locomotion.
On the left a protruding cell is drawn from a lateral view and on the right from a top view. Image amended from [154, 156].

Different stress fiber types with distinct properties exist (see Figure 1.8): ventral stress fibers, dorsal stress fibers and transverse arcs. At the ventral surface ventral stress fibers are located, actin filament bundles that are associated at both ends to focal adhesions. Cell adhesion and contractions rely mainly on these stress fibers. Dorsal stress fibers are actin bundles that are associated at one end to ventral focal adhesions, then rise toward the dorsal part of the cell and finally end primarily with a connection to a transverse arc. Transverse arcs are actomyosin bundles without a direct association to focal adhesions [157–160]. The major family of the receptors for cell-matrix adhesion are integrins [161]. The growth of ventral and dorsal stress fibers generally depends on Dia1 while lateral arcs only depend on ARP2/3 for actin polymerization (see Chapter 1.2.2) [162].
The protrusion of the cell is guided by the anterograde pushing forces from polymerizing actin filaments, opposed by the tension of the plasma membrane. Thus, the filaments that are repelled into the cell body constitute a visible retrograde actin flow. The focal adhesions couple the cytoskeleton to the substrate in a way that these retrograde forces are converted into anterograde protrusion and resulting forward locomotion, a mechanism regulated by actomyosin contraction [160].

To guarantee a directed movement, cells have to establish a polarity. All animal cells use Rho family GTPases therefore [84]. Cell direction is then regulated by the spatial activation pattern of the Rho GTPase Cdc42 and the orientation of microtubules [163, 164].

1.2.3.2 Blebs

Blebbing is a phenomenon that is not only charateristic for the execution phase of apoptosis [165], but is also seen in migrating cells (see below) and in cytokinesis (see Chapter 1.2.5.2 below).
Examples where bleb-driven migration was shown are primordial germ cells (PGCs)

in zebrafish [166] and PGCs in Drosophila melanogaster [167]. Even chemotaxis was shown to use blebs in Dictyostelium [168, 169].

The inner hydrostatic pressure and the cytoplasmic flow lead to cellular protrusions. These are seen as spherical expansions, initially devoid of F-actin and called blebs (reviewed in [170]). In comparison to lamipedial locomotion, bleb-based migration is far more frequent in three-dimensional (3D) environments [171] as blebbing motility needs less or no specific adhesive interactions with the environment [172].

A local decline in membrane-to-cortex attachment [173, 174] or a breakage of the cortex itself [175] both constitute mechanisms for blebs to be formed. Gaps in the cytoskeleton exceeding the critical size of $\sim 0,5 - 1,0\,\mu m$ lead with observed intracellular pressures to such blebs [176]. Formula (1) shows the parameters that influence bleb formation:

$$E = (\kappa * \frac{2}{R^2} + \sigma) * A(R,a) - p * V(R,a) \quad (1)$$

Here p means the internal excess pressure, σ the membrane tension, κ the bending elasticity of the membrane, R the radius of a spherical cap, a the hole radius and E the total energy. A corresponds to the area of the membrane segment and V to the excess volume of the bulge.

Three different phases constitute the life cycle of blebs: initiation, growth and retraction.

1.2.3.2.1 Initiation

The initiation phase functions through the two above mentioned processes. Either the membrane-to-cortex attachment decreases or the cortex ruptures itself. Another possibility is that one mechanism enhances the other one. In this context a small cortex rupture could encourage the membrane to delaminate from the cortex by breaking intermediate links. Thus, a bleb expands close to the initital region of tearing [177, 178].

The underlying system where the bleb initiation occurs is still unknown. Nevertheless, several observations are discussed. It was hypothesized that a downregulation of membrane-cytoskeleton crosslinkers such as ERM proteins (see Chapter 1.1 above) could result in bleb formation [179]. It was also shown that bleb formation requires the contractility of myosin [180, 181]. Either a local activation of myosin could promote delamination of the membrane from the cortex or facilitate cortex tearing [175], or myosin could provoke a local increase in intracellular pressure, simplifying that way the separation of the membrane from the cortex [182].

1.2.3.2.2 Growth

Initially a growing bleb is devoid of F-actin [173] and expands $\sim 5 - 30\,s$ [171]. The pressure leads to an increase of the surface followed by a flow of lipids through the bleb neck [183].

1.2.3.2.3 Retraction

The last step is defined by the reformation of an actomyosin cortex, followed by the retraction of the stabilized bleb [171].

ERMs are capable of binding and regulating Eps8 (Epidermal growth factor receptor pathway substrate 8) [184]. In developing blebs ERMs and Eps8 also colocalize at the plasma membrane [185]. The receptor tyrosine kinase Eps8 is an actin barbed-end capping protein capable of bundling actin [186, 187].

Ezrin does not show a restricted distribution pattern at the blebbing membrane [90], while mDia1 [92] and Eps8 [188] accumulate in multiple foci in a speckle pattern at the blebbing membrane.

These findings led to a hypothesis from Aoki et al suggesting Rnd3 (see Figure 1.9) (also known as RhoE) as a constitutively active GTP-binding Rho family protein. When ROCK phosphorylates Rnd3, the latter changes its localization from the membrane to the cytoplasm, where it binds to 14-3-3 protein [189, 190]. Rnd3 antagonizes RhoA signaling by activating p190-Rho-GAP [191]. That way, in expanding membrane blebs, Rnd3 and p190-Rho-GAP are present in a large number at the plasma membrane and inhibit RhoA activation. As the surface of the bleb increases, the concentration of Rnd3 per area decreases, enabling sporadic RhoA activation. This activation could be amplified and stabilized by RhoA-ROCK phosphorylation of Rnd3. Subsequently Rnd3 sequestrates in the cytoplasm. Thus, p190-Rho-GAP can't be activated any longer. The activity of ROCK increases constantly and results in the phosphorylation of ERM and the subsequent recruitment of Eps8. ERMs and Esp8 then promote the reassembly of the actin cortex and induce that way the rapid retraction of the protruded membrane. Active RhoA could also activate mDia1 for the regrowth of F-actin [188, 192]. Finally myosins accumulate at these actin filaments and the actomyosin contraction results in the retraction of the bleb [90]. Recently myosin II-interacting guanine nucleotide exchange factor (MYOGEF) has been proposed to be transported by activated ezrin to the retracting blebs and to stimulate the activation of RhoA. Thereby an amplifying cycle of activation is introduced [193].

Actin in retracting blebs has $\sim$ 10-fold higher turnover rate compared to the mature cortex [107]. However these processes could involve unidentified molecules. Further studies are needed to understand the whole process of blebbing.

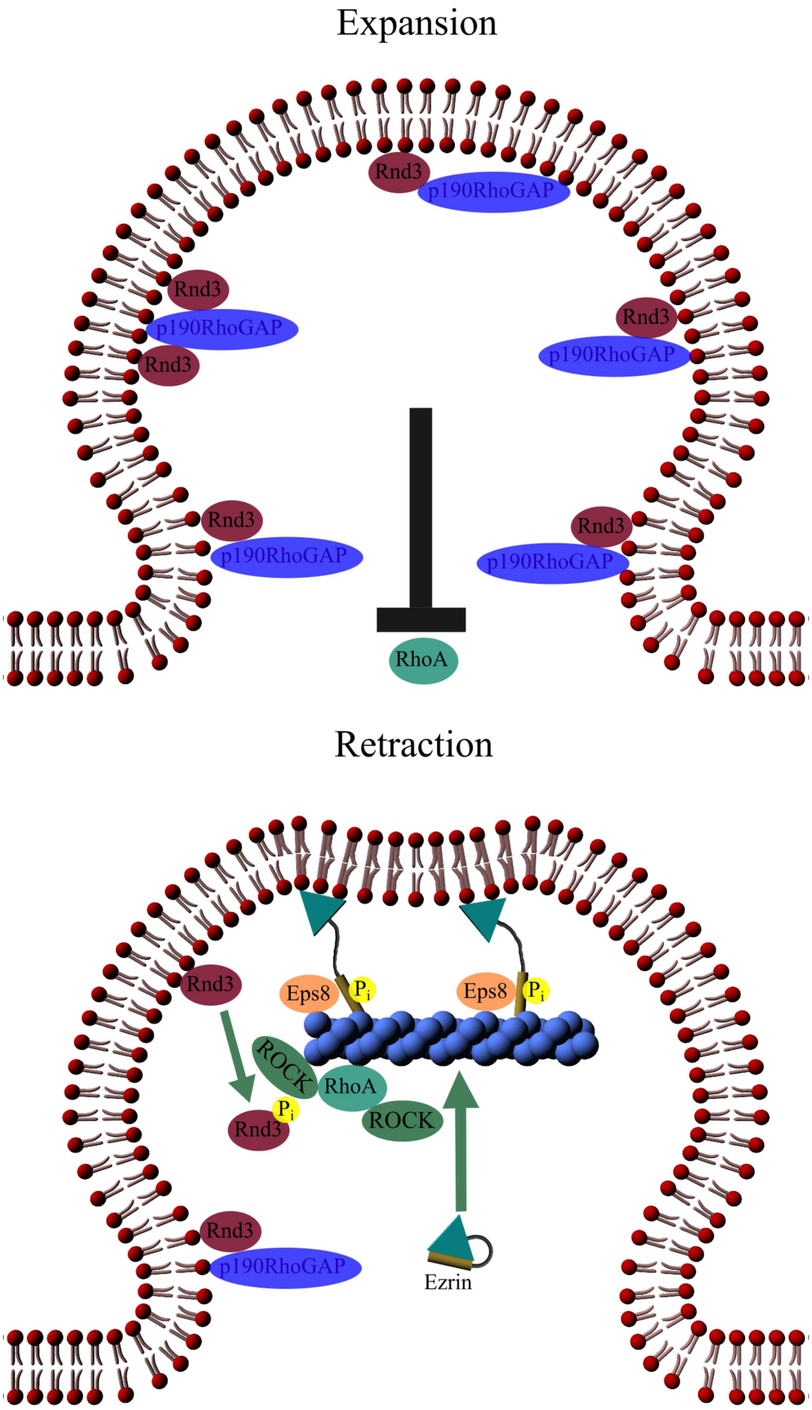

Figure 1.9: The retraction of a bleb as a topological mechanism.
While the bleb expands RhoA can't be activated because of Rnd3 and p190B-Rho-GAP. Then the increasing surface of the bleb decreases the concentration of Rnd3, leading to sporadic RhoA activation. Thus, the retraction is induced by ROCK, further phosphorylating Rnd3 and ezrin. The latter also attracts Eps8 and the cortex starts to be rebuilt. Image modified from [188].

1.2.3.3 Mixed Forms including Lobopodia

In the previous two chapters the motility mechanisms have been strictly separated. In reality, many cells possess the ability to switch between both types of locomotion.

Depending on the environment the best fitting option is chosen [172, 194]. Malignant transformation in cancer cells even allows poorly characterized crossover locomotion strategies [195].

In 3D environments with linear elastic features fibroblasts were shown not to use lamellipodial migration or blebbing, but a mixture, called lobopodial migration. Blunt ended protrusions are formed with small lateral blebs. Unlike lamellipodia, lobopodia don't use active GTPases such as Rac and Cdc42, but they still form focalized adhesions and like blebs are sensitive to actomyosin contractility [156, 196].

1.2.4 Deformation II: Epithelial Morphogenesis

Epithelia are characterized by an apicobasal polarity. The establishment of this polarity includes the formation of zonula adherens junctions on lateral membranes just below the apical surface generating a belt-like band of F-actin, that connects adjacent cells through cell adhesion proteins and complexes (reviewed in [197]), including desmosomes and tight junctions in vertebrate cell-cell interfaces [198].

The formation of the apicobasal polarity is driven by the dynein-dependant transport of the Par complex protein Par3 (in vertebrates) to adherens junctions [199]. At the apical membrane Par3 is locally activated, while it is inhibited at the basal membrane (see Figure 1.10) [200, 201]. This division of the membrane allows key processes at both sides to happen only locally such as increase of $\mathrm{PI}(4,5)\mathrm{P}_2$ at the apical side and subsequent binding of annexin and Cdc42 [202, 203]. Once established, this apicobasal polarity is stabilized by mutual antagonisms or negative feedback regulations between the implicated complexes [200, 204, 205].

Microvilli:

Microvillus was erroneously defined as being 'a membrane-enclosed, finger-like cell surface projection that is supported by a core bundle of actin filaments', because it implies a single type of structure [206]. In reality there are different types of microvilli with distinct cytoskeletal and protein compositions [207, 208].

An actin bundle consists of both β and γ actin isoforms, which are tightly packed together in 20 polarized actin filaments and form thereby the core of the brush border microvillus. The growing end of the actin filaments is facing the plasma membrane at the microvillus tip [209], whereas the pointed ends of the actin filaments grow below the plasma membrane where they are rooted in the actin network, called terminal web. Underlying protein associations in this terminal web still need further research [206]. In the microvilli cores F-actin is bundled by three major proteins: espin, villin and fimbrin [210–212].

Several regulator proteins are under discussion as controling the length of microvilli [206]. Eps8, an F-actin capping and bundling protein, also located at the tip of micrvilli [186], was shown to control the length of microvilli in several studies. Another candidate is Cordon Bleu (Cobl). Located at the base of microvilli, it possesses a COBL domain at the amino-terminus and three WH2 (Wiskott-Aldrich syndrome protein Homology 2) domains toward the carboxy-terminus [213]. The regulation remains unknown, but Cordon Bleu's WH2 domains are capable of nucleating and severing F-actin [214].

Different myosin types are present in microvilli, where they attach the plasma membrane to the actin core (reviewed in [206]). However they have also been described in trafficking cargo inside microvilli [215, 216].

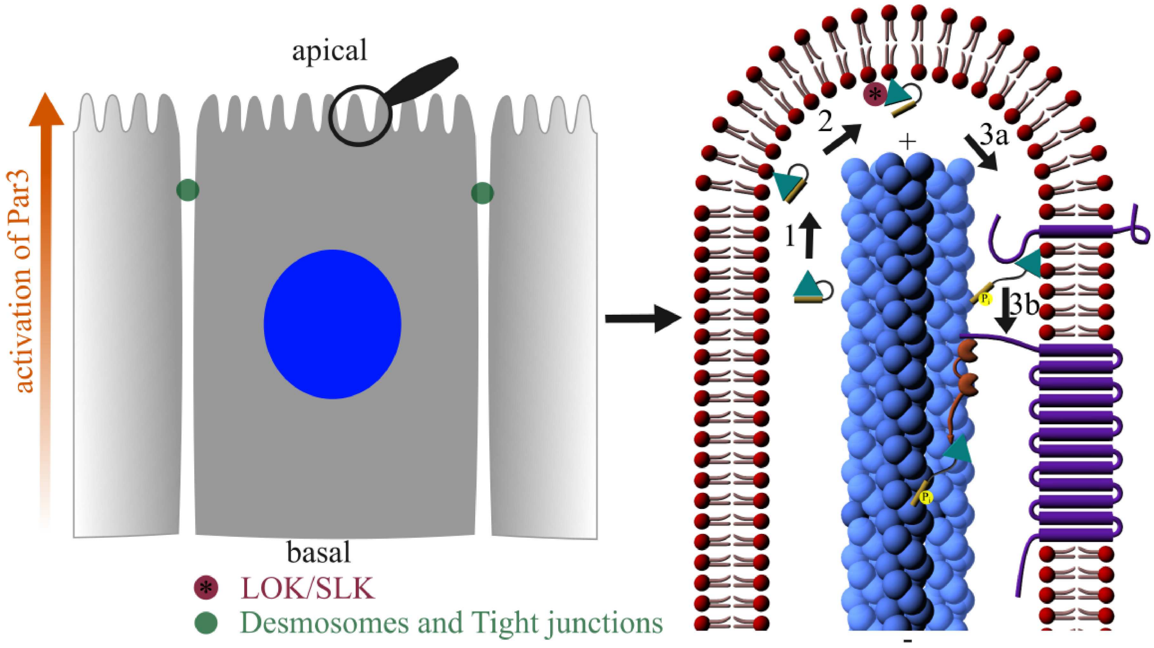

Figure 1.10: Apicobasal polarity of epithelial cells and phosphocycling of ezrin. The activation of the Par3 complex at the apical membrane and its inhibition at the basal membrane establishes the cellular polarity. At its apical membrane the phosphocycling of ezrin is essential for the generation of microvilli. **(1)** First ezrin is activated by $PI(4,5)P_2$ binding, **(2)** followed by a phosphorylation of its T567 by LOK/SLK. This results in the open active conformation, which crosslinks the plasma membrane either **(3a)** directly to the core actin bundle of a microvillus or **(3b)** indirectly. Phosphatases are capable of reverting this conformation and thereby excluding ezrin from stabilizing microvilli. Image based on [200, 201, 206].

ERM proteins (see Figure 1.10 and Chapter 1.1 above) are also located in the microvilli and fulfill their anchoring function to link the plasma membrane to the actin cytoskeleton [2]. In retinal pigment epithelium the knockout of ezrin leads to substantial reduction of apical microvilli [68]. Later it was shown that not only the presence of ezrin, but the cyclic phosphorylation and dephosphorylation of ezrin are essential for microvilli formation. This mechanism is called phosphocycling. In the same study lymphocyte-oriented kinase (LOK) and the sterile 20-like kinase (SLK) were identified as the kinases that activate ERMs in the microvilli [217]. Moreover an interaction between ezrin and Eps8 was shown [184].

1.2.5 Deformation III: Division

In this study the main focus of attention lies on cortex proteins. Therefore, two processes in cell division are of major interest and will be discussed in the next two chapters: mitotic entry with cell rounding and cytokinesis.

1.2.5.1 Mitotic Entry

1.2.5.1.1 Transition Checkpoints

To commit itself to division a cell has established checkpoints that arrest it at the end of G2 in the case of damaged DNA [218]. If no damage is detected, the entry into mitosis is triggered by a network of mitotic kinases. Activation of cyclin-dependant kinase 1 (CDK1, also known as Cdc2) and the simultaneous repression of its opposing phosphatases allow the formation of a complex of CDK1 with cyclin B, which is activated via the phosphorylation by a CDK-activating kinase (CAK) at the G2/M transition [218, 219]. Initially the cyclin B1-CDK1 is activated in the cytoplasm, but next it accumulates rapidly in the nucleus and promotes a spatially controlled positive feedback mechanism in the nucleus, allowing a switch-like start for mitosis [220, 221]. The phosphorylation of cyclin B1-CDK1 substrates increases from the onset of prophase into prometaphase, with its maximum shortly after nuclear envelope breakdown, taking in total a time window of $\sim 30\,min$ [222].

1.2.5.1.2 Cell Rounding

While entering mitosis, substrate or matrix attached cells change their shape from a flat to a spherical geometry. This rounding process starts in early prophase [223] and involves several mechanisms: disassembly of focal adhesions, retraction of the cell margin and formation of a rigid actomyosin cortex [224] (see Figure 1.11a and b):

The entry into mitosis is accompanied by an increase in hydrostatic pressure and a volume enlargement of up to 30 % [225–227]. To retract the cell margin and to allow cellular rounding, the focal adhesions have to be dismantled by actin remodeling. An important actor in the disassembly of focal adhesions is the small GTPase Rap1 [228]. During interphase, active Rap1 stimulates the assembly of focal adhesions by forming a complex with its effector RIAM (Rap1-Interacting Adhesion Molecule) and the integrin activator talin [229, 230]. As a constitutively active form of Rap1 inhibits the disassembly and forces mammalian cells to undergo mitosis at a flatter morphology, a yet unknown inactivator of Rap1 has to become activated at the onset of mitosis [228, 231].

Failure in mitotic rounding leads to defects in spindle assembly, pole splitting, and a delay in mitotic progression. These defects are often associated with dysregulation of mitotic centrosome-nucleated microtubules. Thus, the balance between cell dimension and microtubule reach has to be guaranteed for proper mitosis [231]. Further the geometry during mitosis influences spindle positioning, the axis of division, and thereby cell fate and tissue morphogenesis [232, 233].

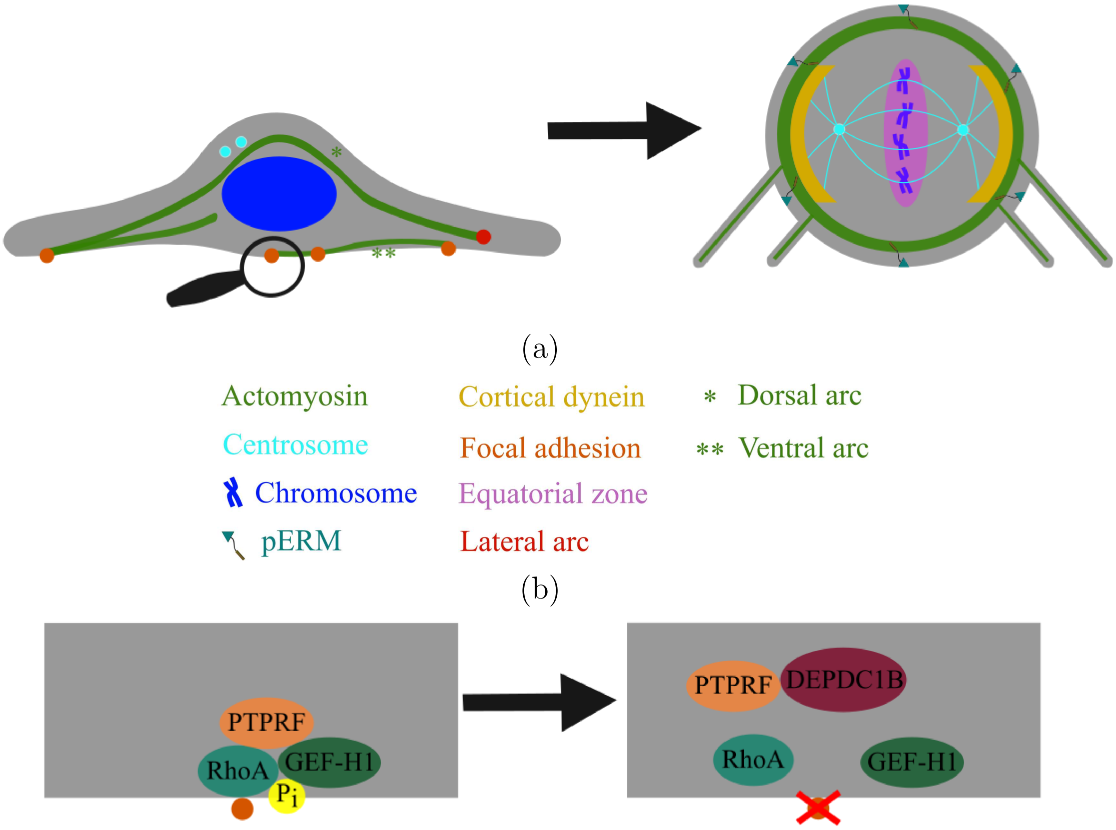

(c)

Figure 1.11: The rounding up mechanism.
(a & b) The entry of mitosis is accompanied by focal adhesion disassembly, and an increase in both the rigidity of the actin cortex and in hydrostatic pressure. The lateral arc can better be seen in Figure 1.8. (c) DEPDC1B prevents the integrity of focal adhesions by binding PTPRF and thereby inhibting the interaction between RhoA and its nucleotide exchange factor GEF-H1. Image based on [224].

A mechanism leading to the disassembly of focal adhesions using the transmembrane tyrosine phosphatase PTPRF, DEPDC1B, RhoA and its nucleotide exchange factor GEF-H1 has been described (see Figure 1.11c). During interphase the integrity of focal adhesions is sustained by the binding of RhoA and GEF-H1 by PTPRF and the subsequent local activation of RhoA. During late G2, DEPDC1B accumulates, binds to PTPRF and pushes RhoA aside. That way Rho is separated from GEF-H1, is inactivated and cannot contribute any longer to the integrity of focal adhesions [234]. DEPDC1B, being a cell-cycle-regulated gene [235], allows the cell to initiate mitotic reshaping, respectively delaying the progression into M phase until the reshape is completed [234].

For cell rounding, the cell margin retracts along thin, actin-rich fibers that maintain some attachment points to the substratum and originate at remnants of interphase focal adhesions [236]. In parallel, actin structures like stress fibers disassemble and the dense actomyosin-rich cortex is remodeled ([237],reviewed in [109] and see Chapter 1.2 above). Astral microtubules attach to this moving actomyosin network and promote the separation of centrosomal microtubule asters for spindle formation [238]. Under confinement the contribution of the actomyosin cortex to a stiffer cortex and subsequent correct cell rounding and spindle assembly is essential. However in isolated cells this role is dispensable [223, 231, 239].

RhoA plays a major role in the remodeling of the actomyosin cortex. At the beginning of prophase the RhoGEF Ect2 becomes active and is transported from the nucleus into the cytoplasm, where it activates RhoA. Thus the retraction of the cell margin and the cortical enrichment of F-actin and myosin II are induced [223, 225, 237]. Two mechanisms allow Ect2 to act on RhoA. First, Ect2 is nuclear during interphase and can therefore only act during prophase [223, 240]. Second, cyclin B1-CDK1 and polo-like kinase 1 (PLK1) hyperphosphorylate Ect2 in mitosis to promote its GEF activity [223, 240, 241]. Furthermore, the inactivation of p190RhoGAP, the inhibitor of RhoA, increases the activity of RhoA [237].

Differently to actin, myosin II only progressively enriches at the cell cortex during prometaphase, accompanying an increase in cortical tension with a peak reached during metaphase [225]. This gradual adaptation probably helps the cell in rigidifying the cortex for rounding against confinement. Another activated regulator of spindle orientation and organizer of the mitotic actin network by Ect2 is Cdc42 [242, 243], even if the pathways are not fully explored.

Other crucial members of the mitotic cell cortex are ERM proteins ([43, 44, 244], reviewed in [49] and see Chapter 1.1). The sterile 20-like kinase (SLK) activates ERMs in mammalian cells at mitotic entry. At the cortex these active ERMs promote the polarized association of leucine-glycine-asparagine repeat protein (LGN) and nuclear mitotic apparatus (NUMA) protein at the cortex facing the spindle poles, both essential for spindle orientation (see Chapter 1.2.5.1.3 below) [244]. For the polarity the cortical actin network defines an enrichment zone for dynein [245, 246]. Furthermore, the crosslinking ability of ERMs ensures the distribution of cortical tension, avoiding local contraction or deformation.

Moreover, Eps8, an actin end-capping and bundling protein already discussed in bleb retraction (see Chapter 1.2.3.2.3 above), was shown to influence the time for cell rounding. In G2, the Ubiquitin E3 ligase SCF^{Fbxw5} is necessary to degrade Eps8, so that the cell can pass through the following pro- and prometaphase in a regulated time period [247].

1.2.5.1.3 Spindle Assembly and Orientation

In polarized cells the cortical actin network helps define the spindle positioning by determining zones of enrichment for dynein [245, 246]. For this positioning junctional adhesion molecule-A (JAM-A) transiently activates Cdc42 and PI(3)K, inducing a gradient of phosphatidylinositol 3,4,5-triphosphate (PIP$_3$) at the cortex [246]. ERM proteins not only stabilize the interaction of astral microtubules with the cortex, but also promote the polarized association of LGN and NUMA protein [29, 244, 248]. Combined, the finding that ERM proteins change location according to adhesion geometry and their ability to orientate the spindle, indicate that ERMs are potential translators of adhesion regulation into intracellular processes for correct spindle orientation [224, 244, 249]. Even in Drosophila embryos, in which mitosis occurs without a cell cortex, mitotic spindle assembly and function require moesin. Effective localization of moesin to the spindle zone needs the full length protein and is only possible in the inactive, autoinhibited form. The localization is probably due to $\mathrm{PI}(4,5)\mathrm{P}_2$ binding. That way a fine balance between the activated, phosphorylated and the inactive, non-phosphorylated form is needed for proper mitosis [250]. This is consistent with observations that neither a permanent active, nor a constantly inactive isoform of moesin can substitute alone for wildtype moesin [251]. The accumulation of the closed form of moesin at the site of future spindle formation implies a yet unknown function [250].

1.2.5.2 Cytokinesis

The process of cytokinesis starts in early anaphase, right after chromosome segregation, when a cleavage furrow forms in the equatorial plane and ingresses inward, and ends in telophase with the physical separation of two daughter cells [252]. Asymmetrical cell division can lead to polyploidy or aneuploidy. Thus, many diseases with cytokinesis deregulation were described, including cancer, infertility and age-related macular degeneration [253].

Division plane

After the onset of anaphase a cell has to define the division plane for further processes. There spindle microtubules play an important role [254]. At anaphase onset the mitotic spindle is structurally reorganized into an array of interdigitating, antiparallel, nonkinetochore microtubules, called central spindle. It originates to a great extent in interpolar microtubules of the mitotic spindle, which get tightly bundled at their plus ends, a region known as spindle midzone (see Figure 1.12).

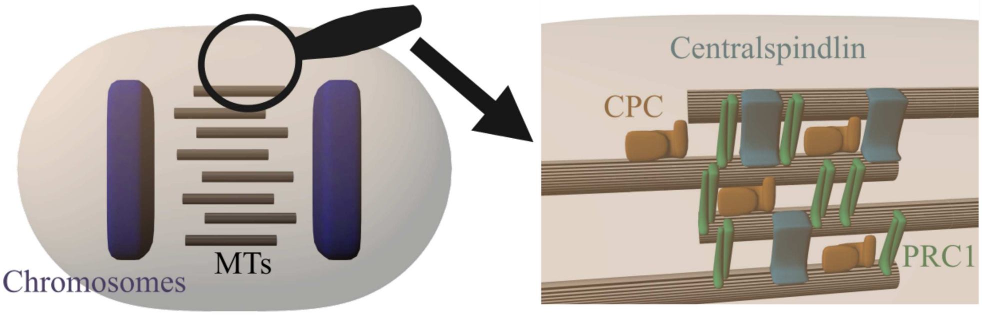

Figure 1.12: The spindle midzone - Part 1.
PRC1 bundles microtubule (MT) bundles (10-30 MTs each) in an antiparallel formation. MT bundling requires the recruitment of CPC and the centralspindlin complex. Image amended from [255].

Not only reorganization, but also de novo microtubule polymerization come into consideration for central spindle formation (reviewed in [256]). To guide this central spindle assembly many cytoskeletal and signaling proteins are required. Among them are the chromosomal passenger complex (CPC), the microtubule-associated protein (MAP), the protein regulator of cytokinesis 1 (PRC1) and at least three kinesin-like motors (KIF4A, KIF20A and KIF23) [257–259]. CDK1 (see Chapter 1.2.5.1.1 above) phosphorylates PRC1 and thereby prevents the interaction between the latter and KIF4 until the transition into anaphase. Then the interaction is promoted by the enzymatic component of the CPC, Aurora B kinase [258–260]. The microtubules of the central spindle are crosslinked by PRC1 [261, 262], whereas microtubule dynamics is suppressed by KIF4, which also inhibits the elongation of the central spindle at a certain period after cytokinesis onset (see Figure 1.13) [260, 263]. A microtubule bundling complex for the central spindle is centralspindlin. Centralspindlin is a heterotetramer built of dimers of KIF23 (also known as MKLP1) and the Rho family GTPase-activating protein RacGAP1/MgcRacGAP. The complex is conserved in many organisms and essential for central spindle formation [264–266]. The inactivation of its KIF23 in metaphase requires a CDK1 phosphorylation, whereas in cytokinesis the CPC localizes KIF23 to the spindle midzone. The constitutive phosphorylation of centralspindlin in mitotic entry causes it to bind to 14-3-3 and prevents targeting to the midzone. Thus, microtubule bundling activity of centralspindlin is promoted by Auora B phosphorylation [267–270]. Finally, the recruitment of the CPC to the spindle midzone is performed by KIF20A [also called Mitotic Kinesin-Like Protein 2 (MKLP2)]. Thereby a local pool of active Aurora B is generated, subsequently regulating KIF4A and KIF23 [271, 272].

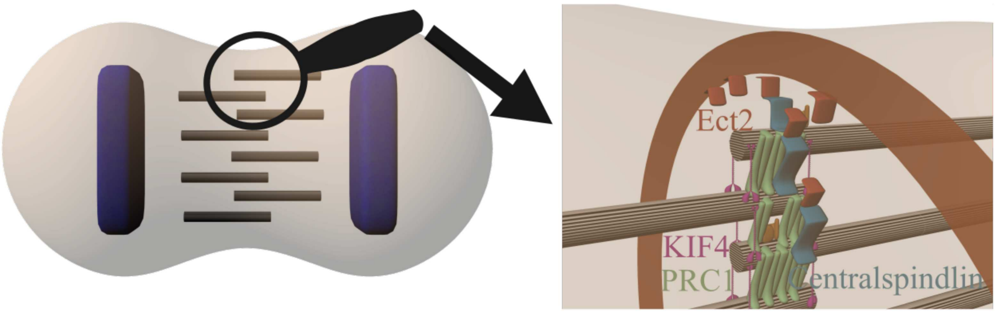

Figure 1.13: The spindle midzone - Part 2.
KIF4 is recruited by PRC1 and limits MT growth to a narrow overlap zone. Ect2 binds centralspindlin and is loaded onto the equatorial membrane. Image amended from [255].

The cleavage plane positioning underlies a combination of two models. According to the 'astral relaxation' model, astral microtubules inhibit furrow formation. Therefore constriction would be only allowed at the equator. The other 'equatorial and central spindle stimulation' model proposes particularly stable astral microtubules as contacting the equatorial cortex and in combination with signaling from the central spindle, thereby inducing furrow ingression at this localization [273–275]. Asymmetric divisions seem to include signals from microtubules for correct cleavage plane determination [276]. However in Drosophila asymmetric cell division is enabled by an established apico-basal concentration difference of phosphorylated moesin [277].

Cleavage furrow ingression

A 'contractile ring', an annulus built of actomyosin filaments, assembles in many animal cells at the cleavage furrow. The major driving force for furrow ingression is supposed to be the contraction of this actomyosin network [278]. At the equatorial cortex the formation of an active zone of RhoA is assumed to be the trigger for cleavage furrow formation and ingression [274, 279]. Then RhoA activates two distinct signaling pathways for the assembly and the constriction of the contractile ring. On the one hand, RhoA stimulates profilin-mediated actin polymerization by binding to diaphanous members of formin-homology proteins. On the other hand, RhoA activates Rho-associated kinase (ROCK). Then ROCK phosphorylates the myosin regulatory light chain (MRLC), which initiates myosin contractility (reviewed in [280, 281]). At the polar cortical regions, astral microtubules were shown to inhibit Rho activation, suppressing the contractility in these regions [282, 283]. In contrast, RhoA is activated at the equatorial region. The kinesin component KIF23 of the centralspindlin complex allows the movement of centralspindlin to the plus end of equatorial and central spindle microtubules [284], where the other component of the complex, MgcRacGAP/RacGAP1, interacts with the RhoGEF ECT2 to guarantee the transport of ECT2 [285, 286]. A guanine nucleotide exchange factor (GEF) accelerates the GDP exchange for GTP in GTPases, whereas a GTPase-activating protein (GAP) enhances the intrinsic GTPase activity. Finally the activated RhoGEF ECT2 is able to be transported to the equatorial cortex, associates with the plasma membrane to phosphoinositide lipids and activates RhoA (see Figure 1.14).

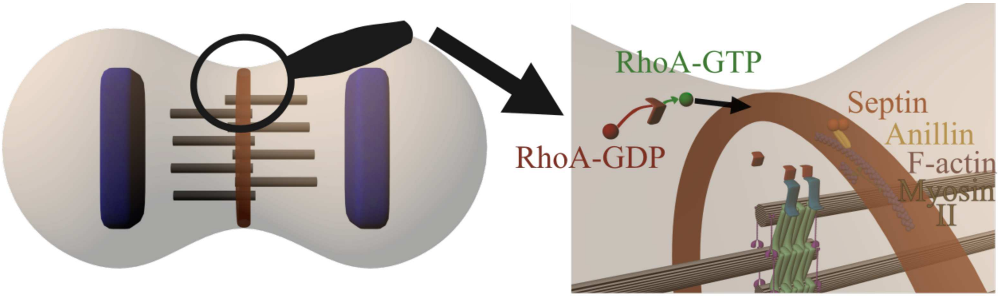

Figure 1.14: The spindle midzone - Part 3.
RhoA-GDP is converted to RhoA-GTP by Ect2 and triggers the assembly of the contractile ring. Image amended from [255].

The locally active RhoA triggers a signaling cascade that assembles the proteins for actomyosin contraction [286–290]. Next to the topological there is a precise time control. In this regard Polo-like kinase 1 (Plk1) can only promote the interaction between ECT2 and RacGAP1 by phosphorylation of the latter in anaphase/telophase, because ECT2 is inhibited in metaphase by Cdk1-mediated phosphorylation [286, 291–294]. Cdk1 phosphorylates ECT2 on two different sites, turning ECT2 unable to bind to the plasma membrane [290]. The declining Cdk1 activity in anaphase/telophase allows the dephosphorylation of ECT2 and Plk1 generates a binding site for ECT2 at the midzone by phosphorylating the N-terminus of RacGAP1 [286, 292, 294].

In vivo RacGAP1 was shown to inactivate Rac GTPases [295, 296]. As a reduced stiffness is required for contractility at the furrow position, the equatorial cortex is inhibited in the formation of a branched actomyosin web by this Rac inactivation via Arp2/3 activity reduction [274, 296]. Whether the role of RacGAP1 is conserved in organisms has still to be elucidated [297].

For cytokinesis the contractile ring has to be properly scaffolded and connected to both the central spindle and the cell membrane. Two proteins of the contractile ring fulfill this function: anillin and citron kinase (CIT-K). Both interact directly with RhoA, probably not as RhoA effectors, and they associate with actin and myosin (CIT-K:[298, 299], anillin:[299] and reviewed in [300]). CIT-K was even described to be a RhoA regulator, that is necessary for the correct localization of RhoA. Furthermore, CIT-K can interact with anillin [299, 301], which binds to $PI(4,5)P_2$ and links not only the plasma membrane with the contractile ring, but also recruits septins to the cleavage site [302, 303]. These septins are conserved GTP-binding proteins. Then septins can be assembled into hetero-oligomeric filaments (reviewed in [304]). Septins are responsible for myosin II localization. In mammalian cells, septin2 provides a molecular platform for myosin II and the kinases ROCK and CIT-K in cytokinesis [305]. Depletion of membrane linkers such as anillin leads to numerous cortical blebs [295]. Additionally loss of anillin leads to lateral oscillations, because the contractile ring becomes instable [306].

Membrane Formation:

During furrowing the total membrane surface increases massively. Therefore membrane vesicles have to be transported and inserted at the cleavage site (reviewed in [307]). To some extent this is realized by endocytic vesicles that bud at the plasma membrane, are routed to early endosomes and then return through recycling endosomes back to the plasma membrane (reviewed in [308]). Moreover secretory vesicles move toward the cleavage furrow, where they dock and fuse [309, 310]. F-actin and vesicles are transported as a unit to the cleavage furrow [311]. A variety of cell types require the recycling of trafficking regulators for completion of cytokinesis, specifically the three small GTPases Rab11, Arf6 and Rab35 (reviewed in [312, 313]). Furthermore, successful cytokinesis most likely requires a special lipid composition at the furrowing plasma membrane, including very long chain fatty acids, allowing shape deformation during furrow ingression [314]. Another mechanism for facilitating membrane curvature is the recruitment of members of the F-BAR protein family to $\mathrm{PI}(4,5)\mathrm{P}_2$ at the ingressing plasma membrane [315]. Additional processes are reviewed in [297].

The Midbody:

In 1891 Flemming was the first to describe the midbody, the intracellular bridge, between two dividing cells. In 1977, one of the first ultrastructural characterizations of the intracellular bridge revealed two parts: one central stem body, with a diameter of $\sim 1,5\,\mu m$ and two narrowed secondary ingression sites on either side of this stem body, with a diameter of $\sim 0,2\,\mu m$ [316]. The midbody derives from the spindle midzone and furrow ingression is essential for midbody assembly [317]. During the constriction of the contractile ring the components of the central spindle are regrouped in three different regions of the maturing midbody (see Figure 1.15) [317, 318].

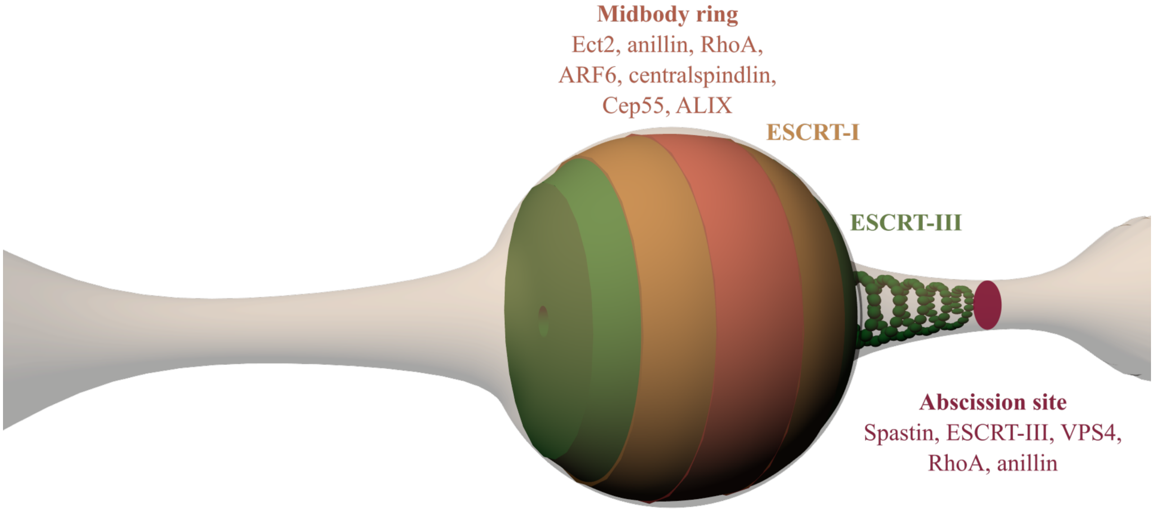

Figure 1.15: The midbody.
Remnants of the former central spindle build the midbody. Image amended from [255].

1) At the centre of the microtubule overlap KIF4 and PRC1 stay associated [317]. 2) Some proteins of the central spindle are released into the midbody ring, among them centralspindlin and Ect2 [317, 318], where they colocalize with proteins such as anillin, RhoA and ARF6. 3) At the midbody flanks, central spindle proteins like CENP-E, MKLP2 and Aurora B colocalize with tightly packed, parallel microtubules. The positioning of the central spindle components into these areas is controlled by Plk1 [317].

The development of the midzone into the midbody is accompanied by the conversion of the contractile ring into the midbody ring [319]. Several contractile ring elements such as anillin, the septins, CIT-K and RhoA are retained in the midbody ring [301, 317, 319, 320]. Here anillin is essential for midbody ring assembly and anchoring it to the plasma membrane [319, 321, 322]. This linking function is assured by its amino-terminal binding to actin and its carboxy-terminal binding of septin-binding-domains [300, 323], while the localization of anillin is dictated by RhoA [301].

The Abscission:

Complexes known to be important in membrane scission during viral budding and budding of vesicles into late endosomes were also shown to possess a key role in abscission and are called endosomal sorting complexes required for transport (ESCRTs) (reviewed in [324–327]. Cep55, a protein of the midbody ring, directs the ESCRT recruitment [318, 328, 329]. On either side of the midbody ring ESCRT-I and ESCRT-III are recruited sequentially to form partially overlapping, membrane-juxtaposed rings [318]. High resolution live and fixed imaging reveal helical filaments of a diameter of 17nm, situated between the stem body and the abscission site [330]. Ripples that were already observed in 1977 correspond to the locations of these ESCRT-III filaments [316]. At the peak of ESCRT-III localization at the abscission site, the midbody experiences an abrupt loss of midbody microtubules, followed by the cell separation [330]. This microtubule depolymerizing is thought to be realized by spastin, which is recruited by ESCRT-III [331–333].

The timepoint of abscission is defined by the inactivation of Plk1 and Aurora B. On the one hand, Plk1 phosphorylates Cep55, so that it cannot interact with centralspindlin and be located to the midbody [334–336]; however at mitotic exit Plk1 is degraded. On the other hand, Aurora B phosporylates a regulatory region of ESCRT-III, called CHMP4C, and thereby avoids premature abscission [337, 338].

Furthermore, some actin capping and nucleating proteins seem to be implicated in abscission. After metaphase, including cytokinesis, the capping activity of Eps8 is required for cortical stability. A lack of Eps8 leads to membrane blebbing and cell shape deformations [247]. Also mDia1 depletion leads to division failure [92].

1.3 ERMs in mitosis

ERMs were already mentioned in the chapters above with respect to their roles during cell division. Here some parts will be reemphasized and expanded by recent research data.
ERM proteins accumulate at the cleavage furrow [63], constitute organizers of the mitotic cell cortex and the mitotic spindles [43, 44, 244], potentially link adhesion formation to correct spindle orientation [224, 244, 249], and the closed form of dmoesin resides at the future site of mitotic spindle formation in Drosophila [248]. After all a fine balance is needed for cell shape transformations [339, 340].

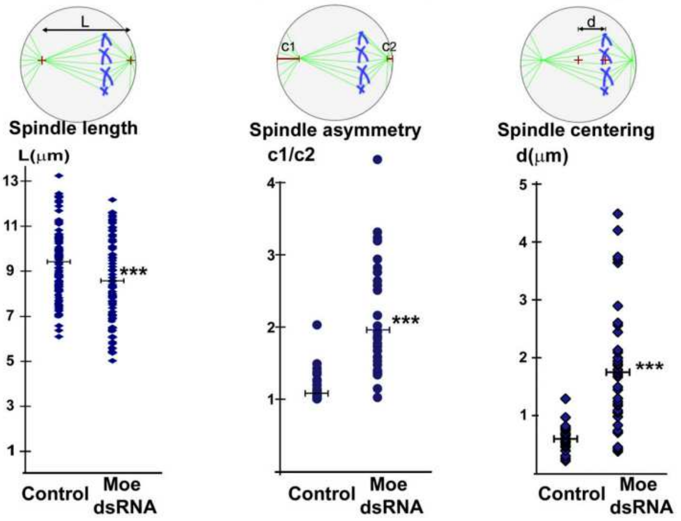

Figure 1.16: Analysis of mitotic spindles.
L = mitotic spindle length, c1/c2 = ratio between distances of the centrosomes to their respective polar cortex, d = distance between the geometrical center of the cell and the center of the spindle. Image from [43].

It could be shown that after inactivation of dmoesin in Drosophila, the spindle length, symmetry and positioning were effected (see Figure 1.16). In metaphase the regulation of spindle organization and the cell shape transformation in anaphase require the interaction between ERMs and microtubules, whereas the connection between F-actin and the metaphase cortex is independant of this interaction [29].
Recently, Vilmos et al revised their observations and were able to specify their findings. In fact, the structure built by dmoesin co-localizes with the mitotic spindle, but the structure exhibits a compact, dense texture with no apparent filaments and differs thereby significantly from the spindle. Furthermore, the dmoesin containing structure reaches its peak fluorescence intensity shortly after prophase, whereas the spindle is formed by microtubules until metaphase. Finally, the presence of this newly discovered dmoesin-containing structure after the inhibition of microtubule formation lead the authors to the conclusion that dmoesin plays a yet unknown role

in spindle formation.

Additionally, next to the primary Ect2 pathway a second signaling that induces the relaxation of the polar cell cortex in anaphase has been found. This includes a movement via the segregating chromosomes of the kinetochore-localized PP1 phosphatase and its regulatory subunit Sds22 to the polar regions, where they trigger the dephosphorylation of ERMs and subsequently the softening of the cortex, so that elongation of the cell in anaphase is facilitated [341].

While the proteins are dephosphorylated at the poles, ezrin is recruited to the cleavage furrow through its membrane-association domain. This transport is cholesterol dependant but almost Rho independant [342] and associated with the local microvilli [342, 343]. Furthermore, the ingression of the furrow is not dependant on ERMs. However when other membrane cytoskeleton crosslinkers (anillin and supervillin) are depleted, ERMs substantially assist the furrow ingression, even if they are unable to recover the loss of the other proteins. Moreover the transient knockdown of ERMs does not heavily influence the progression of furrow ingression [342].

2 Scope of the Thesis

Previous data obtained by Dr.Rathangadhara Chakrapani Nammalwar in the lab had revealed the already known enrichment of ezrin at the cleavage furrow in live cell imaging and his work included the generation of an HeLa ezrin knockout cell line. The aim of this thesis was thereby to use this epithelial cell line lacking the major ERM member for the analysis of the roles and redundancies of ERMs in mitosis and specifically in cytokinesis. Dynamic methods should be included to allow the investigation of roles of ERM proteins for the rounding-up and the correct sharing of the chromosomal content between the nascent daughter cells.

3 Materials and Methods

3.1 Materials

3.1.1 Bacterial Strains

Bacteria	Genotype
Escherichia coli DH5α	F^+, deoR, endA1, gyrA96, hsdR17, $(r_k{}^-, m_k{}^+)$, gInV44, thi-1, recA1, relA1, supE44, φ80Δ lacZ Δ M15, thi-1, Δ(lacZYA-argF)U169

Table 3.1: Bacterial strains

3.1.2 Cell Lines

Cell line	Description/Cultivation
HeLa	From cervical adenocarcinoma derived epithelial cells. Cultivation in a DMEM (Dulbecco's Modified Eagle Medium) solution with 10% FCS (Fetal Calf Serum), 1% L-Glutamine, 1% Penicillin/Streptomycin at 37 °C and 7% CO_2 atmosphere.
HeLa ezrin$^{-/-}$ knockout, clone B	HeLa cell line that Dr.Rathangadhara Chakrapani Nammalwar generated with CRISPR/CAS9 technique. Cultivation in a DMEM (Dulbecco's Modified Eagle Medium) solution with 10 % FCS (Fetal Calf Serum), 1 % L-Glutamine, 1 % Penicillin/Streptomycin at 37 °C and 7 % CO_2 atmosphere.

Table 3.2: Cell lines

3.1.3 DNA Constructs

Name	Insert	Vector	Restriction Enzymes	Reference
GFP-ezrin	Human ezrin full length cDNA	pEGFP	EcoRI/SalI	A.Heil [344]
GFP-N-ERMAD	Human ezrin cDNA coding for AA 1-296	pEGFP	EcoRI/SalI	A.Heil
GFP-ezrin PIP2-binding mutant	Human ezrin cDNA with K63N, K64N, K253N, K254N, K262N and K263N mutations	pGEX-T2	XmaI/AatII, Cfr9I/KpnI, Asp718/Cfr9I, NcoI/Cfr9I	C.Barret [345]

Table 3.3: DNA constructs

3.1.4 Small interfering RNAs (siRNAs)

Description	Company
siEzrin Smart Pool	Dharmacon
ON-Target plus Smart pool human Moesin	Dharmacon
ON-Target plus Smart pool human Radixin	Dharmacon

Table 3.4: Small interfering RNAs

3.1.5 Antibodies

Antigen	Species	Dilution	Company
Ezrin	Rabbit	WB: 1:5.000	Millipore
Ezrin	Mouse	IF: 1:100	BD Biosciences
Moesin	Mouse	IF: 1:100 WB: 1:5.000	BD Transduction Laboratories
Radixin	Rabbit	WB: 1:1.000	Cell Signaling
α-Tubulin	Mouse	WB: 1:10.000	Sigma
Phospho-Ezrin(Thr567)/ Radixin(Thr564)/ Moesin(Thr558)	Rabbit	IF: 1:100 WB: 1:1.000	Cell Signaling

Table 3.5: Primary antibodies

Description	**Dilution**	**Company**
IRDye 680 RD goat anti-mouse	1:10.000	LI-COR
IRDye 800 donkey anti-rabbit	1:10.000	LI-COR

Table 3.6: Secondary antibodies used in western blots

Description	**Dilution**	**Company**
Alexa-Fluor-488 donkey anti-mouse	1:1.000	Molecular Probes
TRITC-phalloidin	1:1.000	Sigma

Table 3.7: Secondary antibodies used for immunofluorescence staining

3.1.6 Chemicals

Chemical/Reagent	**Company**
Ammonium persulfate (APS)	Carl Roth
Ampicillin	Carl Roth
β-Marcaptoethanol	Applichem
Bromphenol blue	amresco
BSA Fraction V	Carl Roth
Complete Protease Inhibitor Cocktail	Roche
DAPI	Sigma
Dimethylsulfoxide (DMSO)	AppliChem
distilled water DNase/RNAse free	gibco
Dulbecco's Modified Eagle Medium (DMEM)	Sigma
Ethanol	AppliChem
FACS Clean	BD
FACS Flow	BD
FACS Rinse	BD
Fetal Calf Serum (FCS)	Biochrom (SO115/0435A)
GeneJammer Transfection Reagent	Agilent
Glycerin/Glycerol	AppliChem
Glycine	AppliChem
Hoechst 33342 5mL (20mM)	Thermo Scientific
Imidazole	Carl Roth
L-Glutamine	LONZA (BE17-605E)
Lipofectamine 2000	Invitrogen
Methanol	AppliChem

Chemical/Reagent	Company
Mowiol 4-88	Calbiochem
Nocodazole powder	Sigma-Aldrich
Non-fat dried milk	AppliChem
OptiMEM	Gibco
Paraformaldehyde (PFA)	Sigma
PBS$^{(-/-)}$	Sigma
PBS$^{(+/+)}$	Sigma
Penicillin/Streptomycin	LONZA (DE17-602E)
Propidium Iodide	eBioscience
Rotiphorese®Gel 30	Carl Roth
Sodium chloride	AppliChem
Sodium dodecyl sulfate (SDS) pellets	Carl Roth
Sodium hydroxyde	Carl Roth
Tetramethylethylenediamine (TEMED)	Carl Roth
Thymidine	Sigma
Tris	AppliChem
Triton-X-100	AppliChem
Trypsin/EDTA 10x	Biochrom
Tween 20	AppliChem

Table 3.8: Chemicals

3.1.7 Kits

Kit	Company
BCA Protein Assay Kit	Pierce
PureLink®HiPure Plasmid Filter DNA Purification Maxi kit	Invitrogen

Table 3.9: Kits

3.1.8 Devices

Device	Company
10cm dish	greiner bio-one
145mm dish	greiner bio-one
35mm dish nunclon surface	nunc™
6-well dish Nunclon ™Delta Surface	Thermo Scientific

Device	Company
96-well dish costar 3595	Corning Incorporated
Analysis balance LP 1200 S	Sartorius
Analysis balance Quintix 224-S	Sartorius
Bacteriological incubator Modell 500	memmert
Biosphere®Filter Tips	SARSTEDT
Blockthermostat BT200	Kleinfeld Labortechnik
Cell Scraper 25cm 2-position-blade	SARSTEDT
Centrifuge 5424R	eppendorf
Centrifuge Allegra X-12	Beckman Coulter
Centrifuge Avanti J-25	Beckman Coulter
Counting Chamber, Neubauer	Assistent®
Epoch	BioTek
EVOS digital inverted microscope	PeqLab
FACS Calibur	Becton Dickinson
Flow Cytometry Tubes Ref 55.1579	SARSTEDT
GV 0.22μm Filter unit	Millex®
HERA Cell 240i CO_2 cll incubator	Thermo Scientific
Injekt 2mL	Braun
innova 4230 Refrigerated Incubator Shaker	New Brunswick Scientific
LabTek 8 chambers	ibidi
Leica DM IL Microscope	Leica
LSM 780	Carl Zeiss Microscopy
LSM 800	Carl Zeiss Microscopy
Microlane 3 18G	BD
Mini gel system?	Biometra
Nanodrop ND-1000 UV/Vis Spectrophotometer	PeqLab
Nitrocellulose Membrane 0.45μm	Amersham^{TM}GE Healthcare Life Sciences
Odyssey Infrared Imaging System	LI-COR Biosciences
pH meter 766 Calimatic	Knick
Pipetboy accu	Integra Biosciences
Pipets	Gilson
Power Pack P25	Biometra
RCTbasic	IKA LABORTECHNIK
Rocking Platform	Biometra
Sprout®Mini Centrifuge 12V	Heathrow Scientific
Sterile work bench HERASafe HS12	Heraeus Instruments

Device	Company
TC20 Automated Cell counter	BIO-RAD
Thermomixer 5436	eppendorf
Tubes for transfection (5mL)	SARSTEDT
μ-Slide 4 well	ibidi
Vortex-Genie 2	Scientific Industries
Water bath	GFL

Table 3.10: Devices

3.1.9 Software

Software	Company
Cell Q Pro	Becton Dickinson
Excel 365	Microsoft
Fiji (Fiji is just ImageJ) 1.51n	Freeware
Image Studio	LI-COR
INKSCAPE 0.92	Freeware
Lightwave 3D 2015.3	NewTek
MikTex 2.9.6300	Freeware
R 3.4.1	Freeware
TexMaker 5.0.1	Freeware
ZEN black 2.3 SP1	ZEISS

Table 3.11: Software

3.2 Methods

3.2.1 Molecular biological methods

3.2.1.1 Cultivation of Escherichia coli

E.coli DH5α was cultivated in sterile lysogeny broth (LB) liquid medium or on LB agar plates (see Table 3.12), both at 37 °C.
After transformation, the transformed E.coli clones were selected by adding the respective antibiotic to the LB medium. In this thesis a stock solution of 25 mg/mL of Kanamycin was added to the LB medium at the ratio of 1:500. Only the clones that contained the plasmid with the necessary resistance to the antibiotic could grow.

LB liquid medium
1 % (w/v) Tryptone
0,5 % (w/v) Yeast extract
1 % NaCl

(a)

LB-Agar plates
1 % (w/v) Tryptone
0,5 % (w/v) Yeast extract
1 % NaCl
1.5 % Bacto-Agar

(b)

Table 3.12: LB mediums (a) LB liquid medium and (b) LB-Agar plates

3.2.1.2 Transformation of chemically competent E.coli

100 μL frozen chemically competent E.coli DH5α was thawed slowly on ice.
Then 1 μL of the purified plasmid DNA was added and the mixture was again incubated on ice for 30 min.
Next the mixture was transfered to a bacterial incubator at 37 °C for 1 min, followed by a quick incubation on ice for 10 min. 500 μL of LB medium was added and the bacteria were incubated for 30 min at 37 °C and 250 rpm in a shaker incubator.
Transformed clones were selected by spreading the vial's content on LB agar plates supplemented with the respective antibiotic.

3.2.1.3 Purification of plasmid DNA

To purify plasmids in large scale the PureLink ®HiPure Plasmid Filter DNA Purification Maxi kit (Invitrogen) was used.
One colony of the transformed E.coli was incubated in 400 mL LB medium with the respective antibiotic overnight. The bacteria were then harvested by centrifugation at 4.000 g for 10 min.
In the meantime, the PureLink®HiPure Maxi Column along with the Filtration Cartridge was equilibrated with 30 mL of Equilibration Buffer (EQ1).

The generated bacterial pellet was resuspended in $20\,mL$ of Resuspension Buffer (R3) with RNAse A by gentle shaking. Then the bacteria were lysed by adding $20\,mL$ of Lysis Buffer (L7) by gently inverting the bottle until the mixure was homogenous. For $5\,min$ the lysate was next incubated at room temperature. The addition of $20\,mL$ of Precipitation Buffer (N3) results in the precipitation of bacterial proteins and other debris. Again the bottle was directly inverted 3 times gently until the mixture was homogenous.

Then the equilibrated column was filled with the precipitated lysate obtained from the previous steps, which was allowed to pass the filtration cartridge by gravity flow. Next the column was washed with $50\,mL$ of Wash Buffer (W8).

Finally the plasmid DNA was eluted with $15\,mL$ of Elution Buffer (E4) into a sterile $50\,mL$ centrifugation tube. The addition of $10,5\,mL$ ice cold isopropanol resulted in the precipitation of the eluted DNA, which was harvested by centrifugation at $12.000\,g$ for $30\,min$ at 4 °C. The supernatant was discarded. Then the pellet was washed with $5\,mL$ of 70 % ice cold ethanol and centrifuged for $5\,min$ at 4 °C. For $10\,min$ the final pellet was air dried and resuspended in $200 - 500\,\mu L$ of RNAse and DNAse free water.

3.2.1.4 Quantification of DNA

The Nanodrop spectrophotometer makes it possible to check both the concentration and the purity of a DNA suspension.

At $260\,nm$ an absorption value of 1 coincides with a dsDNA concentration of $50\,\mu g/mL$. The optical densities ratio between $260\,nm$ and $280\,nm$ ($OD_{260} : OD_{280}$) is a readout for the purity. A value of about $1,8$ is considered to be “pure”.

3.2.2 Cell biological methods

3.2.2.1 Eukaryotic cell culture

The human cervical carcinoma cell line (HeLa) was cultivated in a DMEM (Dulbecco’s Modified Eagle Medium) solution with 10 % FCS (Fetal Calf Serum), 1 % L-Glutamine and 1 % Penicillin/Streptomycin at 37 °C and 7 % CO_2 atmosphere.

To passage the cells, the medium was aspirated and the cells were washed once with $10\,mL$ of PBS without Ca^{++} and Mg^{++} ($PBS^{-/-}$). After having aspirated the $PBS^{-/-}$, $1\,mL$ of a Trypsin/EDTA solution was added and the cells were incubated for $5 - 7\,min$ at 37 °C.

Afterwards the cells detached by a gentle tapping of the dish. $9\,mL$ of fresh medium was added to stop the trypsinization. The resulting suspension was then centrifuged at 200 g for 4 min. The supernatant was discarded and the cell pellet resuspended in 10 mL of fresh medium. Finally either $1mL$ of the resuspension was poured on a dish with 9 mL of fresh medium for reseeding, or 500 μL of the resuspension was poured on a dish with 9,5 mL of fresh medium, depending on the cell confluency at the beginning of the passaging steps. The reseeded cells were then used for continuous culture.

3.2.2.2 Cryopreservation of eukaryotic cells

Cryopreservation makes it possible to keep sufficient stocks of cell lines. Therefore they are preserved at −195 °C in liquid nitrogen.

Once cells had reached confluency, the medium was aspirated and the cells were washed once with 10 mL of PBS$^{-/-}$. After having aspirated the PBS$^{-/-}$, 1 mL of a Trypsin/EDTA solution was added and the cells were incubated for $5-7\,min$ at 37 °C.
Afterwards, the cells detached after a gentle tapping of the dish. 9 mL of fresh medium was added. The resulting suspension was then centrifuged at 200 g for 4 min.
The supernatant was discarded and the cell pellet was resuspended in FCS containing 10 % (v/v) DMSO. DMSO is a cryopreservative, protecting cells from ice crystal formation upon freezing. Labeled cryovials were each filled with 1 mL of the cell suspension and stored for 1 day at −80 °C in a cryocontainer that facilitates gradual freezing.
Finally the cryovials were transferred into liquid nitrogen tanks for extended storage periods.

When new cells were needed, a vial was taken out of the liquid nitrogen tank, transferred rapidly to a water bath adjusted at 37 °C and, when the last frozen material had thawed, the cell suspension was seeded into a 10 cm dish containing 9 mL of prewarmed medium. Finally the dish was transferred into a cell incubator for continued long-term culture.

3.2.2.3 Cell counting

3.2.2.3.1 General cell counting

Some experiments need a fixed confluency for the cells. Therefore the cells have to be counted before seeding.
The enumeration was performed using a hemocytometer (Neubauer cell chamber) when relatively exact values were needed. 10 μL of the cell suspension to analyze

was loaded into a Neubauer cell chamber. The cells were counted in 4 squares, each containing 16 “sub-squares” and the average of the squres was used to determine the concentration, according to the following formula:

$$\text{Total cells/mL} = \text{Average cell count} * \text{Dilution factor} * 10.000\, cells/mL \qquad (2)$$

Alternatively to the hemocytometer, the TC20 Automated Cell counter was used.

3.2.2.3.2 Shake off counting method

The proper rounding up of the cells in prometaphase implies a functional cell cortex stiffening. By transiently downregulating ERM proteins using Lipofectamine (see Chapter 3.2.2.4.1 below), early defects in mitosis, in particular proper rounding-up, can be studied.

Early defects would also lead to preselection of certain cellular phenotypes in the FACS method later described (see Chapter 3.2.5 below).

The following protocol was used:

On the first day the HeLa wildtype cells were seeded at a confluency of about 40 % in a 6-well dish.

The next day the cells were transfected with Lipofectamine in the morning. 7 wells were used: $n\,°1$: untransfected, $n\,°2$: a mock transfection using only Lipofectamine, $n\,°3$: Control siRNA, $n\,°4$: siEzrin, $n\,°5$: siRadixin, $n\,°6$: siMoesin and $n\,°7$: combined siEzrin, siRadixin and siMoesin. In the evening the cells were washed three times and the medium was changed to growing medium containing nocodazole (see Chapter 3.2.4.1 below).

On day 3 the majority of the cells was blocked in prometaphase. The rounded up cells were forced to enter into suspension by pipetting the growing medium of the wells several times in and out. Next, this suspension was introduced into a Falcon tube. For each well, one tube was used. The remaining cells in the wells were analysed under the EVOS digital inverted microscope. As not all the rounded up cells came into suspension, the cells were gently rinsed with $2\,mL$ new growing medium. The resulting suspension was added to the corresponding Falcon tubes. If needed, the rinsing was performed a second time. Then, the remaining non-rounded up cells in the wells were trypsinized with $500\,\mu L$ of a Trypsin/EDTA solution and the cells were incubated for $5 - 7\,min$ at 37 °C. Afterwards the cells detached after a gentle tapping of the dish. $1,5\,mL$ of fresh medium was added to stop the trypsinization. The content of each well was transfered into new 7 Falcon tubes.

Finally the cell concentration of the rounded up fraction and of the non-rounded up fraction could be measured (see 3.2.2.3.1 above). Afterwards the quality of the downregulation could be determined with Western blot (see 3.2.3 below).

3.2.2.4 (Transient) Transfection of eukaryotic cells

2 types of transient transfection had been used: Lipofectamine-2000 and GeneJammer.

3.2.2.4.1 Lipofectamine-2000

For some experiments proteins were transiently down regulated by usage of siRNA. This transfection was performed using Lipofectamine-2000. The protocol for a 10 cm dish went as follows:
First the cells were seeded at a confluency of about 60 %.
After one day the transfection solution was mixed at room temperature and each addition was followed by gentle mixing.
$4,8\,\mu L$ of Lipofectamine-2000 was added to $1,463\,mL$ of prewarmed Opti-MEM® in one tube. In another tube 200 *picomoles* of siRNA were introduced into $1,463\,mL$ of prewarmed Opti-MEM®. After 5 min the contents of both tubes were combined. 20 min later the solution was put in the medium of a 10 cm dish. Finally at $t = 4{-}6\,h$ the cells were washed three times and put overnight in the incubator.
On day 3 the cells were ready for experiments.
When the cells had to undergo a nocodazole block, they were seeded at a confluency of about 30 % on day 1. On day 3 the nocodazole block was started in the evening and the cells were ready on day 4.

3.2.2.4.2 GeneJammer

The GeneJammer method was used for plasmid DNA transfection for live cell analysis in confocal microscopy. Here 4-well chambers with 800 μL medium per chamber were utilized. The protocol went as follows:
On the first day the cells were seeded at a confluency of about 50 %.
After one day the transfection solution was mixed at room temperature and each addition was followed by gentle mixing.
$4,8\mu L$ of GeneJammer was introduced into $112\,\mu L$ of prewarmed Opti-MEM® medium, followed by the addition of $1,6\,\mu g$ of plasmid DNA after 5 min. 20 min later 1/4 of the mixture was put into each well.
Finally the cells were incubated overnight.
On the next day the cells were washed three times with prewarmed medium before being stained with Hoechst 33342 (see Chapter 3.2.6.2 below). Then the cells were ready for microscopy.

3.2.3 Protein biochemical methods

3.2.3.1 Cell lysate preparation

In order to analyze the cellular expression levels of the proteins in question, cell lysates were prepared. Afterwards the lysates underwent SDS-PAGE and Western Blotting.

Depending on the transfection type, the lysis time point was different. Experiments using Lipofectamine transfection needed 48 h incubation, whereas GeneJammer transfection only needed 16 h incubation. For lysis cells were washed once with PBS$^{-/-}$ before being resuspended in 120 μL of lysis buffer (Table 3.13).

Lysis Buffer Stock Solution	
Reagent	**Volume**
Imidazole ($pH = 7,4$)	20 mM
NaCl	100 mM
Triton-X-100	1 %
The final lysis buffer also contained Complete Protease Inhibitor Cocktail. 1 mL into 25 mL Stock Solution was used.	

Table 3.13: Lysis buffer

The lysates were incubated at 4 °C for 30min on an overhead rotator. Finally, they were centrifuged for 20min at 4 °C and 15.000 rpm. The supernatant was then moved to new tubes. After performing the bicinchoninic acid (BCA) test (see 3.2.3.2 below) and diluting the supernatants to adjust the same protein concentration in 45 μL, 15 μL of Loading Buffer (Table 3.14) were added and samples were boiled for 5 min at 95 °C.

Loading Buffer 4x (for $10\,mL$)	
Reagent	**Volume/Weight**
β-Mercaptoethanol	$800\,\mu L$
Bromphenol blue	$40\,mg$
Glycerin	$4,0\,mL$
SDS	$0,8\,g$
Tris $0,5\,M$ $(pH\,6,8)$	$5,0\,mL$
H_2O	Add to $10\,mL$

Table 3.14: Loading buffer

Now the samples were ready for SDS-PAGE (see 3.2.3.3 below).

3.2.3.2 Protein concentration determination using the BCA test

Loading the wells for SDS-PAGE (see 3.2.3.3 below) requires protein amount standardization to allow a more precise comparison between the wells.

Here the Pierce BCA Protein Assay Kit was used. The biuret reaction that utilizes the reduction from Cu^{+2} to Cu^{+1} by proteins is combined to the colorimetric detection of the chelation product of two bicinchoninic acid (BCA) molecules with one Cu^{+1} ion. The strong absorbance at $562\,nm$ of this complex is almost linear between $20 - 2.000\,\mu g/mL$.

The BCA working reagent was freshly mixed, by adding 50 parts of reagent A to 1 part of reagent B. $25\,\mu L$ of standard solutions and the unknown samples were pipeted into wells on a 96-well dish. Then $200\,\mu L$ of the working reagent was mixed with the different solutions and put for $20\,min$ in the incubator at $37\,°C$. Afterwards the dish was permitted to cool down before reading the absorbance with a spectrophotometer.

The standard solutions make it possible to trace the absorbance in function of the protein concentration and thereby deduce the concentration of the samples.

3.2.3.3 Sodium-Dodecyl-Sulfate Polyacrylamide Gel-Electrophoresis (SDS-PAGE)

Since its invention in 1970 by Laemmli [346], the SDS-PAGE has become a widely used method in labs to separate proteins according to their molecular mass indepently of charges. Later it was improved by Schägger [347] to enlarge the range of molecular masses that could be detected. An overview of more recent minor improvements can be found in Bass [348]

Depending on the molecular weight of the proteins separated, the percentage of acrylamide in the gel has to be chosen in advance for a good separation in the range of interest. For ERM proteins, gels with 12 % acrylamide had been used (Table 3.15).
The SDS inhibits non covalent bindings and that way linearizes the protein structure as anionic detergent. Subsequently a uniform negative charge around the proteins coats their inner charges. Thereby the resolution of the proteins in a polyacrylamide-gel is independent of charges and depends solely on the respective molecular mass.

SDS-polyacrylamide Gel 12 %		
Reagent	**Volume for Running Gel (for** $10\,mL$**)**	**Volume for Stack (for** $2\,mL$**)**
H_2O	$3,3\,mL$	$1,4\,mL$
30 % Acrylamide mix	$4,0\,mL$	$0,33\,mL$
$1,5\,M$ Tris	$2,5\,mL$ ($pH\,8,8$)	$0,25\,mL$ ($pH\,6,8$)
10 % SDS	$0,1\,mL$	$0,02\,mL$
10 % APS	$0,1\,mL$	$0,02\,mL$
TEMED	$0,004\,mL$	$0,002\,mL$

Table 3.15: SDS-polyacrylamide gel 12 %

The gel system itself consists of 2 combined media – an upper gel, called stack, and a lower gel, called running gel. As the pore size in the stack is larger than in the running gel, the proteins stack together at the migration zone between both gels. Another difference is the pH. While the stacking gel has its pH at 6, 8, making a trailing ion boundary, the running gel has $pH\,8,8$, making a leading ion boundary. The trailing border is built behind the migrating proteins and the leading border in front of the migrating proteins. Between these two boundaries the proteins are concentrated. This discontinuous system allows clear bands as final result.
The prepared lysates from 3.2.3.1 (see above) were introduced, after boiling, in wells of the stacking gel, after pouring SDS-Page Running Buffer into the system (Table 3.16). A current of $200\,V$ was used to start the system. It was stopped after $45\,min$ or when the dye front had migrated fully through the gel.

SDS-PAGE Running Buffer	
Reagent	**Quantity**
Glycine	$192\,mM$
SDS	$0,1\,\%$ (w/v)
Tris-HCl ($pH\,8,8$)	$25\,mM$

Table 3.16: SDS-PAGE running buffer

3.2.3.4 Western blotting

In 1979 Western Blot was invented independently by Renart et al. [349] and Burnette [350]. This blotting technique allows the transfer of resolved proteins from an SDS-polyacrylamide gel to a Nitrocellulose or a PVDF membrane. Again Bass [348] can be referred to for more recent improvements.

Under an electric current the proteins migrate here from an SDS-polyacrylamide gel to a nitrocellulose membrane without changing their structure. Thereafter antibodies are used to detect the proteins at the surface of the membrane.

For blotting, tank blot systems from Bio-Rad were used. To mount the systems, 4 Whatmann papers, 2 sponges and the nitrocellulose membrane were first soaked in cold Blotting Buffer (Table 3.17). Then the gel and the membrane were placed in between 2 sets of Whatmann papers. A falcon tube was gently rolled over the system to remove trapped air bubbles. Next, the system was placed between two sponges and then placed inside the blot carrier. The blot carrier was then put into the blot tank. Before filling the tank with cold blotting buffer, some ice was added in a recipient to keep the temperature low. Then the tank was placed in an ice bath. Finally a conductivity of $300\,mA$ was set, which started the transfer. After $1h$ the current was stopped.

Now the membrane was ready for blocking and antibody detection.

Blot Solution (for $1\,L$)	
Reagent	**Volume/Weight**
Glycine	$15\,g$
Methanol	$200\,mL$
Tris	$3,0285\,g$
H_2O	add to 1000 mL

Table 3.17: Blot solution

3.2.3.5 Antibody treatment and detection

For further treatment the nitrocellulose membrane was taken out of the blot tank and isolated from the papers and the gel. First the membrane had to be blocked in a blocking buffer consisting of a $PBS^{-/-}$ solution with $0,1\,\%$ Tween-20 and $5\,\%$ bovine serum albumin (BSA). This was placed for $1\,h$ on a shaker. Afterwards the regions where no proteins are located are blocked, reducing that way unspecific binding of antibodies.

The blocking buffer was removed and the membrane was then exposed to a solution of blocking buffer, with specific primary antibody at the respective dilution, as indicated by the manufacturer. The incubation time on a shaker was either $1\,h$ at room temperature or overnight at $4\,°C$. After the incubation, PBS-Tween was used to wash the blot three times for $5\,min$ on a shaker at room temperature.

As secondary antibodies, appropriate infrared labeled antibodies from Li-COR Biosciences were used in a solution of PBS-Tween with $5\,\%$ Non-fat dried milk powder at a dilution of 1:10.000. Again the blot was incubated for $1\,h$ at room temperature on a shaker before being washed three times with PBS-Tween for $5\,min$ as in the previous step.

Finally, the blot was ready for detection on the Li-COR Infrared detection system.

3.2.4 Cell synchronization methods

A cell population is formed of multiple cells, with groups at different points of the cell cycle. When an experiment is not just studying the cell cycle of one single cell, as in microscopy for example, the cell population has to be synchronized first. Therefore, chemical reagents can be used that interfere with key steps in the cell cycle, so that cells can't go beyond a certain point anymore. The result is an accumulation of cells at this stage of the cell cycle. Finally, the reagent has to be washed out and a synchronized cell population is ready to be analysed.

3.2.4.1 Nocodazole block

An antimitotic agent that can be used for synchronization is nocodazole. Spindle fibers are formed by microtubules. These microtubules are disrupted by nocodazole as it binds to β-tubulin and inhibits the formation of one of two interchain disulfide linkages. As result $> 90\,\%$ of the cells become arrested at the $G2/M$ checkpoint and a synchronized cell population can be studied. After washing the nocodazole out, the microtubules are again able to polymerize and the spindle fibers can attach to kinetochores, so that the cell division can occur.

Here we used a concentration of $50\,ng/mL$ in prewarmed growth medium. The cells were incubated overnight for $16\,h$ with the antimitotic agent and in the morning gentle tapping against the dish allowed the rounded-up cells (corresponding to the cells in $G2/M$) to detach and go into suspension. Then the cells were ready for examination.

3.2.5 Flow Cytometry

In contrast to the microscopic methods, the flow cytometer permits the analysis of whole cell populations in one single step. Developed by Dittrich and Göhde in 1968 [351] in Münster, the flow cytometry, based on fluorescence, makes it possible to analyze features such as cell size, granulation, DNA content or density, depending on the type of measurement.
In our case, the cells have to be fixed first before being analysed. Ethanol or paraformaldehyde (PFA) are two possibilities. As the cytometer takes its measurement through lasers at different wave length, appropriate stainings have to be applied next to the cells. The next four chapters explain the approach in detail.

3.2.5.1 Ethanol fixation

Cells that nocodazole was applied to and that were reseeded after washing out the antimitotic agent were gently tapped out of the dish into suspension or were forced into suspension with growth medium containing trypsin/EDTA.
They were centrifuged at $200\,g$ for $2\,min$ at room temperature. Then the pellet was washed once by resuspending the pellet in PBS$^{-/-}$ and centrifuging it again at $200\,g$ for $2\,min$ at room temperature. The resulting pellet was resuspended in $100\,\mu L$ of PBS$^{-/-}$ before adding $900\,\mu L$ of ice-cold $70\,\%$ ethanol. Next the suspension was mixed through gentle pipetting. Then the fixed cells were incubated for $> 2\,h$ on ice. Finally, the cells were ready for the staining procedure.

3.2.5.2 Propidium iodide staining

Propidium iodide is a fluorescent DNA intercalating agent that can be used for staining the cell nucleus.
The ethanol fixed cells were first centrifuged at $200\,g$ for $5\,min$ at room temperature. The supernatant was removed and the resulting pellet resuspended in $500\,\mu L$ of propidium iodide staining solution (Table 3.18). Before using the stained cells in flow cytometry, they were incubated for $30\,min$ at room temperature in the staining solution.

Propidium Iodide Staining Solution ($10\,mL$)	
Reagent	**Volume**
PBS$^{-/-}$	$8,8\,mL$
Propidium Iodide from a stock solution of $2\,g/L$	$100\,\mu L$
RNAse (DNAse free) from a stack of $10\,g/L$	$200\,\mu L$
Triton-X-100 from a stock solution of $10\,\%$ in PBS$^{-/-}$	$100\,\mu L$

Table 3.18: Propidium iodide staining solution

3.2.5.3 Analysis of Mitosis

The method of examining the cytokinesis of cells uses the cell cycle synchronization by nocodazole, fixing the synchronized cells in ethanol at different time points, after washing out the antimitotic agent and staining the cells with propidium iodide before subjecting them to flow cytometry. This technique was developed by Gasnereau [352] and already established in our lab by Dr.Rathangadhara Chakrapani Nammalwar.

The method was used to study the effect on cytokinesis of downregulating transiently either ezrin, radixin and moesin (ERM) in HeLa wildtype, or of downregulating transiently radixin and moesin together in HeLa ezr$^{-/-}$ KO cells. The protocol went as follows (see Figure 3.1):

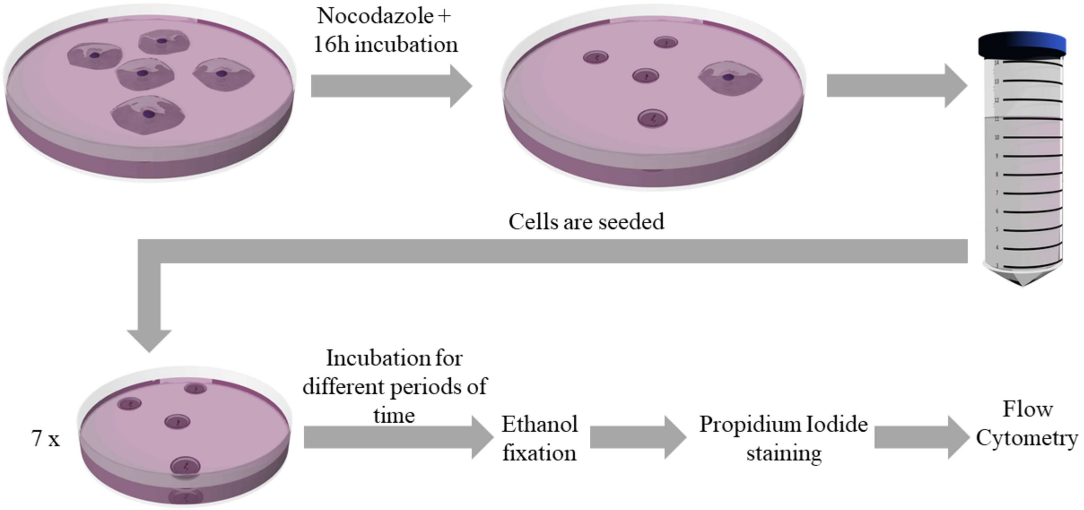

Figure 3.1: Preparation for flow cytometry

On the first day HeLa cells were seeded in a $10\,cm$ dish to a confluency of about $30\,\%$. Then after one day the growth medium was replaced by prewarmed growth medium containing $50\,ng/ml$ of nocodazole at 18:00. The cells were incubated overnight with this agent. On the third day the synchronized cells were selected first at 9:00 by gently tapping the 10 cm dish, so that the rounded-up cells went into suspension. This entry into suspension was checked under the microscope. Next, the suspension was centrifuged at 200 g for 4 min and the supernatant discarded. The cell pellet was resuspended in 10 mL of growth medium. This centrifugation and resuspending was done three times to wash the nocodazole out. The cell pellet was finally resuspended in 15 mL of growth medium. Then, 2 mL of the suspension was introduced in each of 7 35 mm dishes. The remaining 1 mL was used for lysis and Western blot analysis. The 7 dishes were incubated for different periods of time: 30 min, 60 min, 75 min, 90 min, 105 min, 120 min and 180 min.

During the incubation the cells could pursue their mitosis in absence of nocodazole. At the mentioned time points this mitosis progress was stopped and cells were fixed for further analysis. To do this, the respective 35 mm dish was taken out of the incubator. For the 30 min dish, the cells were not settled, so that gentle shaking moved the cells again into suspension. Then the suspension was transferred into a 15 mL centrifugation tube. For all the time points other than 30 min, the remaining cells on the dish were washed with 500 μL of PBS$^{-/-}$ and then trypsinized with 500 μL of prewarmed trypsin for 2 min. Next, the cells on the dish were resuspended in $1,5\,mL$ of warm growth medium and added to a 15 mL centrifugation tube. The tube was centrifuged at 200 g for 2 min at room temperature. The supernatant was discarded. Then the cells were washed by resuspending the pellet in 5 mL of PBS$^{-/-}$ and the tube was centrifuged again with the same parameters. Afterwards the cell pellet could be resuspended in 100 μL of PBS$^{-/-}$. Lastly 900 μL of 70 % ice-cold ethanol was added. The fixed cells were then placed on ice.

On the fourth day the cells were stained with propidium iodide (see 3.2.5.2 above) and the cells were prepared for flow cytometry.

FACS Calibur was used as flow cytometer, whose argon laser excited at 488 nm using FL2 as acquisition channel. In a scatter plot the fluorescence area (FL2-A) was plotted against the intensity of fluorescence (FL2-H). In addition the forward scatter (FSC-H) was plotted against the sideward scatter (SSC-H). Examples of plots are shown in Figure 3.2a and 3.2b. The numbers of the counting are described in Table 3.19.

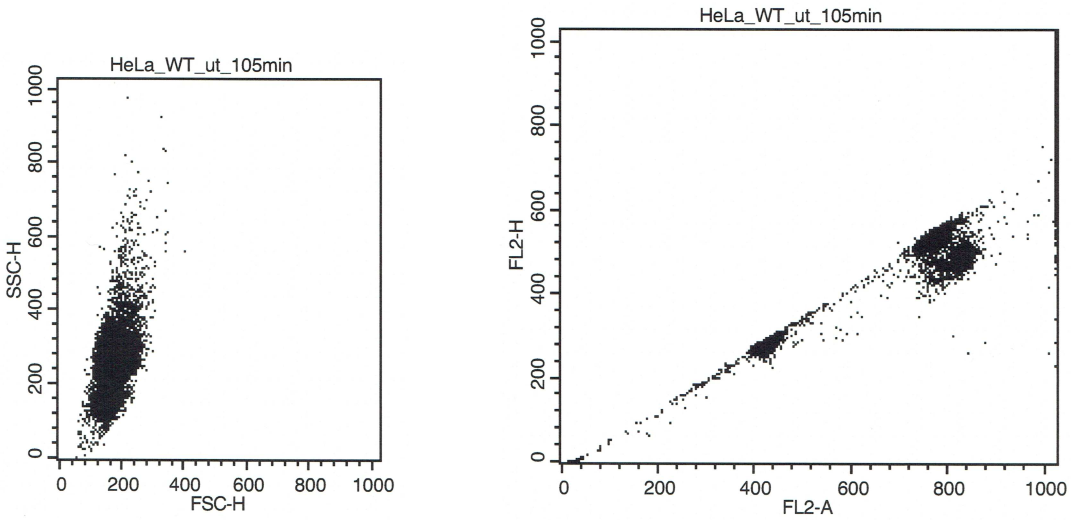

(a) forward scatter = f(sideward scatter) **(b)** FL2-A = f(FL2-H)

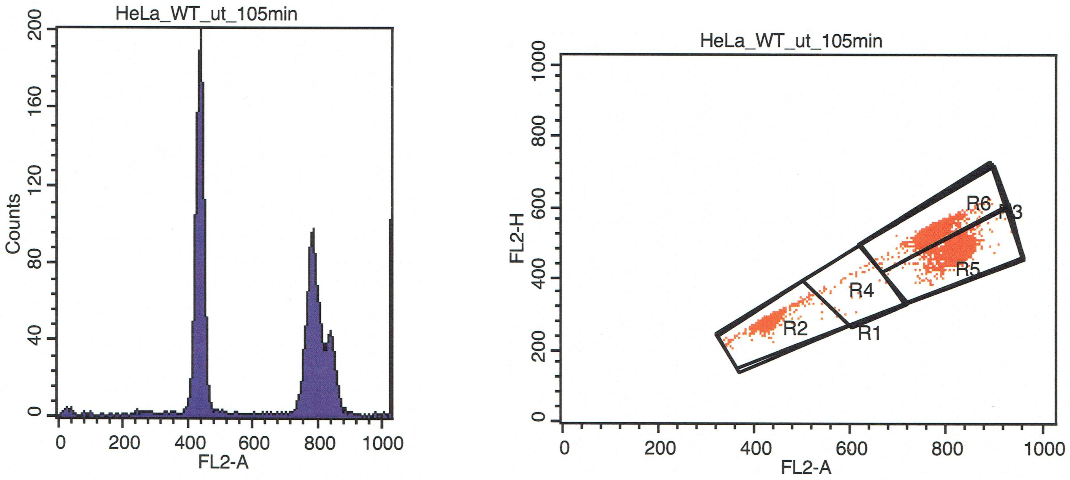

(c) FL2-A = f(Counts) **(d)** Gates

Figure 3.2: Mitosis assay in flow cytometry

Region	**Events**	**% Gated**	**% Total**
R1	9234	100,00	92,34
R2	4468	48,39	44,68
R3	4723	51,15	47,23
R4	45	0,49	0,45
R5	1643	17,79	16,43
R6	3106	33,64	31,06

Table 3.19: Counts in gates

Gates were applied to separate the different populations. The subpopulations were then quantified in their region as percentage of the total gated cell population. Such typical gated scatter plots are shown in figure 3.2d and in figure 3.3 over time. The latter figure shows at 30 *min* a homogenous cell population (**M**). The DNA content (FL2-A) and the DNA peak fluorescence (FL2-H) are very similar in population **M**. As 90 % of the cells are in prometaphase after 30 *min* these close values were expected. The cells have a DNA content of $2n/4c$ (1 chromosome pair/4 chromatids) and a similar peak DNA due to condensed chromosomes.

At 60 *min* two new cell populations appear. As cell division proceeds after having reseeded the cells, the cells undergo prophase and metaphase. Then the chromosomes start to segregate and the DNA peak intensity (FL2-H) reduces, leading to cell population **C**. As long as the cells are not separated into two daughter cells, the DNA content (FL2-A) stays at the same value. This population **C** intensifies over time until 90 *min* and **M** reduces constantly.

Another nascent population at 60 *min* is the **G1** cell population. It is situated at half the FL2-A value, corresponding to completed cell divisions. Its cells' DNA content is of $2n/2c$ (1 chromosome pair/2 chromatids). Also the DNA peak fluorescence is at half the value of the **M** population. The **G1** population grows over time.

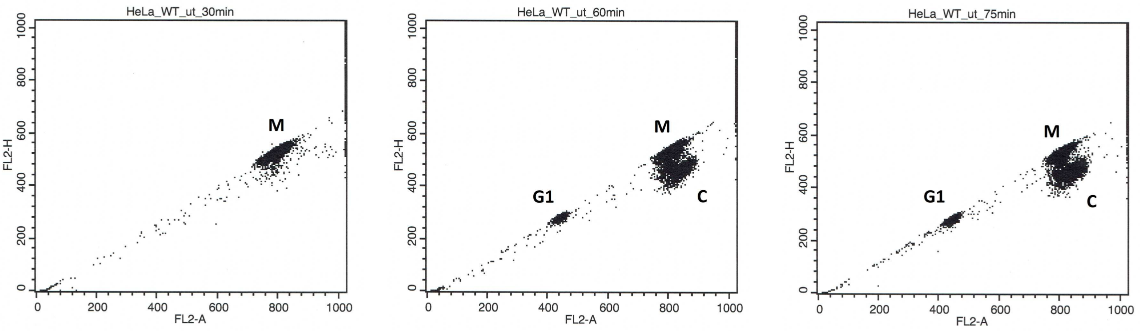

(a) HeLa WT 30 *min* **(b)** HeLa WT 60 *min* **(c)** HeLa WT 75 *min*

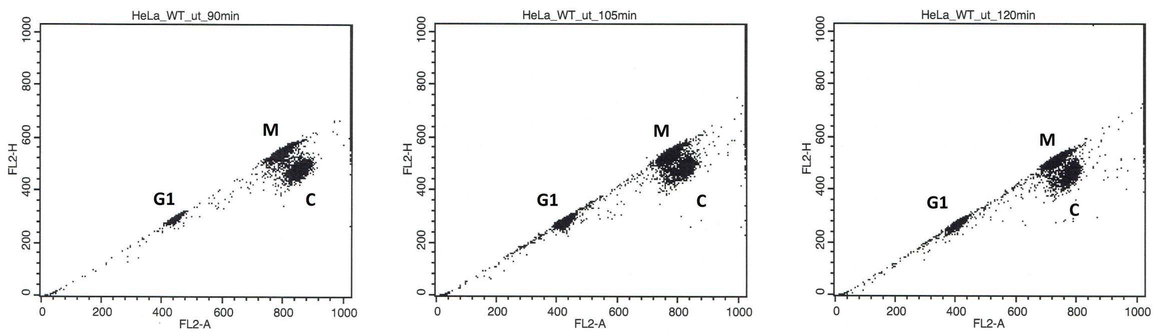

(d) HeLa WT 90 *min* **(e)** HeLa WT 105 *min* **(f)** HeLa WT 120 *min*

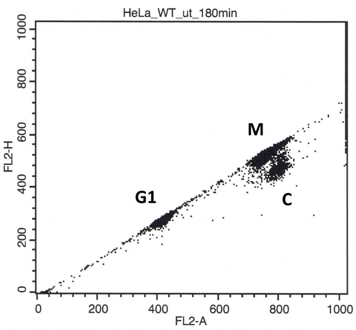

(g) HeLa WT 180 *min*

Figure 3.3: Cell population in flow cytometry.
3 cell populations can be observed: a mitotic (**M**), a cytokinetic (**C**) and a **G1** cell population.

The gated percentages were plotted as a grouped bar graph for each time point, allowing the analysis of the mitotic time scale in HeLa cells.
Disturbances of this time scale through downregulation of proteins can thereby be analysed in these bar graphs.

Mitosis failure can result in multinucleated cells. To test for the presence of multinucleation FACS Mitosis Assays can be used. One example is shown in 3.3 for HeLa ezr$^{-/-}$ KO. The measurements were performed as described above. Only the FL2-A on the x axis was expanded to also identify cells with $3n$ (R7) or $4n$ (R8) chromosomes (see Figure 3.4).

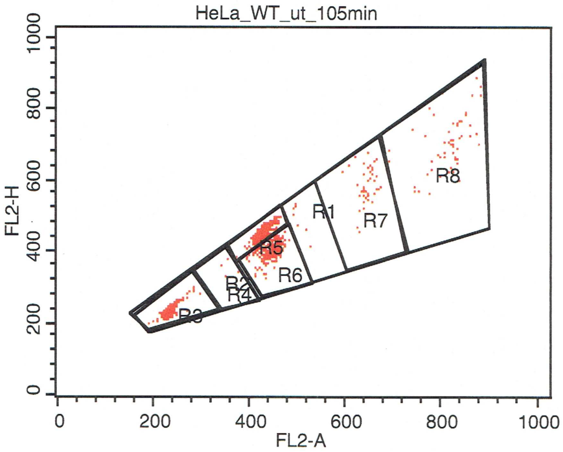

Figure 3.4: Multinucleation

3.2.5.4 Statistical Methods

In many of the time-consuming experiments of this thesis, replicas of 3 were performed and some shown as individual graphs.
In this work, statistical examination mainly refers to the FACS assays and employed the method developed by Gasnereau [352]. Mean values were analysed with their

standard deviation over time by using the ANOVA test, followed by the Tukey post-hoc test fits. ANOVA requires several assumptions: independence of observations, a normal distribution and homogeneity of variances (homoscedasticity). A given assumption is the independence of observations. The kind of distribution can't be inspected, but there exist tests for the assumption of normality. However $n > 3$ is needed. Changing to other statistical tests, like the Kruskal-Wallis, would influence the level of significance and the power in a way that $n \gg 3$ would even be needed. Furthermore, the ANOVA test is not very sensitive to moderate violations of the normality assumption when a large sample number is considered [353–355]. In the literature the Gasnereau method was used in three papers [356–358] for analysis of mitosis, but none gave reasons why a normal distribution can be assumed, or performed a statistical analysis at all. Finally, the ANOVA test is used in this thesis in view of its alleged robustness, but further studies will have to prove the normal distribution of cells undergoing mitosis.

Concerning systematic errors, they can't be completely excluded in the progress of an experiment, but as other lab members independantly got similar results, the probability is very small.

3.2.6 Imaging

A lot of experimental methods such as flow cytometry or colorimetric reactions analyse whole populations. A strong point of microscopy is the detailed analysis of both, the localization of proteins and a quantification of them (either enrichment or downregulation).

2 different microscopic methods had been used.

3.2.6.1 Cell fixation and immunofluorescence staining

Immunofluorescence of fixed cells is analyzing dead cells under the microscope. The cellular structure is preserved by the fixation and makes it possible to store the resulting microscopic slide for a longer period of time. Permeabilization then permits the passage of the antibodies through the cell membrane and thereby the labeling of their specific protein targets. After being incubated with the primary antibodies, fluorescently labelled secondary antibodies are used.

Here the microscopes LSM 780 and the LSM 800 were utilized.

8 welled labtek chambers were chosen to grow the cells. The fixation started with washing the cells twice gently with $250\,\mu L$ of PBS containing Ca^{++} and Mg^{++} (PBS$^{+/+}$) at 37 °C. Next, the cells were fixed with $150\,\mu L$ of 4 % paraformaldehyde (PFA). After the addition of PFA the cells were incubated for $5 - 7\,min$ at 37 °C. Then the cells were washed twice with $250\,\mu L$ of PBS$^{+/+}$ at 37 °C. The permeabi-

lization was done by adding 150 μL of 0,5 % Triton-X-100 in PBS$^{+/+}$ for 15 min. Resulting free aldehyde groups were modified by incubating the cells three times for 10 min at room temperature with 150 μL of glycine buffer (Table 3.20). These aldehyde groups could show some autofluorescence.

Glycine Buffer	
Reagent	**Volume/Weight**
$NaCl$ $(5\,M)$	$1,3\,mL$
Na_2HPO_4 $(0,2\,M)$	$1,75\,mL$
NaH_2PO_4 $(0,2\,M)$	$0,875\,mL$
Glycine	$0,3735\,g$
dH_2O	$46,075\,mL$

Table 3.20: Glycine buffer

Then the cells were washed twice with PBS$^{+/+}$ at room temperature. An incubation of 1 h in blocking buffer (Table 3.21) at room temperature followed. Finally on day 1, the cells were incubated with 200 μL of primary antibody overnight at 4 °C. For this, the Labtek chambers were placed in a humid chamber, to which gentle shaking was applied. On the second day, the cells were washed three times with 200 μL of PBS$^{+/+}$ for $4-5$ min at room temperature. The secondary antibodies were introduced in the appropriate dilution in blocking buffer. 200 μL of this solution was then poured into each chamber. After an incubation of 1 h at room temperature the cells were washed three times as in the previous step. Finally the cells were mounted in a drop of mowiol and permitted to dry overnight at room temperature. Microscopy could start on the following day.

Blocking Buffer	
Reagent	**Volume/Weight**
$NaCl$ ($5\,M$)	$1,3\,mL$
Na_2HPO_4 ($0,2\,M$)	$1,75\,mL$
NaH_2PO_4 ($0,2\,M$)	$0,875\,mL$
NaH_3 ($0,3\,M$)	$1,28\,mL$
Bovine Serum Albumine (BSA) (1 %)	$1\,mL$
Triton-X-100 (10 %)	$1\,mL$
Tween (10 %)	$0,25\,mL$
FCS	$5\,mL$
dH_2O	$37,545\,mL$

Table 3.21: Blocking buffer

3.2.6.2 Live cell time lapse imaging

For live cell imaging the LSM 780 was used. The microscopic method of live cell imaging was chosen to analyze the expression of GFP labelled ezrin and GFP labelled N-ERMAD in time and space during mitosis.

On the first day, the cells were seeded on 4 well μ slides from ibidi with a starting confluency of about 40 %. Then after one day the cells were transfected using GeneJammer (see 3.2.2.4.2 above). Finally, on day 3, the cells were ready for microscopy. First the LSM 780 was switched on with the incubator set at 37 °C and 7 % CO_2. Thereby a stable temperature could be guaranteed over the image capture time. Next, the medium of the cells was changed to warm growth medium containing Hoechst 33342 at $125\,ng/mL$. Hoechst 33342 is a DNA intercalating fluorophore that is capable of passing the cell membrane. The cells were incubated for $20\,min$ at 37 °C. Finally the cells were washed three times gently with $500\,\mu L$ of prewarmed growth medium and were then ready for microscopy.

4 Results

4.1 Localization of ERM proteins in HeLa cells

In order to analyze the role of ERM proteins in cell divsion, the localization of these proteins has first to be studied in the different cell division phases.
Figure 4.1 shows the distribution of activated ERM proteins (pERM), in representative selected HeLa wildtype cells, in all five phases of mitosis. In prophase the ERMs are ubiquitously spread in the cytosol and at the membrane. After the breakdown of the nuclear envelope in prometaphase the distribution of ERMs remains similar. In metaphase ERMs accumulate at the cell membrane. This membranous concentration persists until the end of cytokinesis. In anaphase and telophase a slightly brighter signal can also be observed at the cleavage furrow.

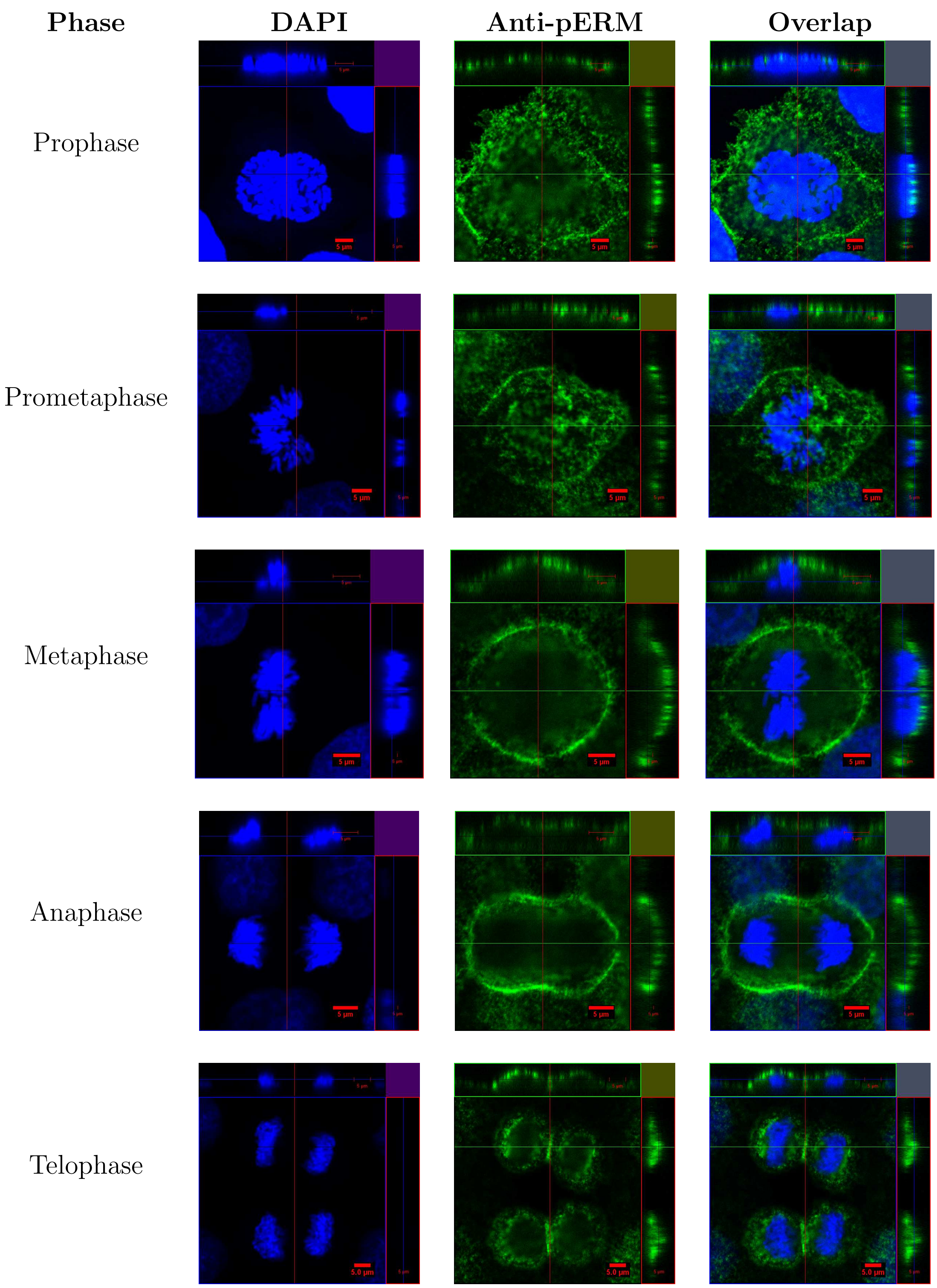

Figure 4.1: Distribution of phosphorylated ERM proteins in HeLa Wildtype cells undergoing mitosis.
DAPI (dilution 1 : 1.000) was used to visualize chromosomes in blue and ERMs were detected in green with anti-pERM (dilution 1 : 100). pERM are phosphorylated/activated ERMs. Scale bar $= 5\,\mu m$. In each image, the upper left rectangle shows the frontal view, the lower left square a cut view through cells and the lower right rectangle the side view.

To look specifically at the contribution of ezrin, a knockout (KO) was performed and the distribution of the remaining ERM proteins, radixin and moesin, was analyzed.

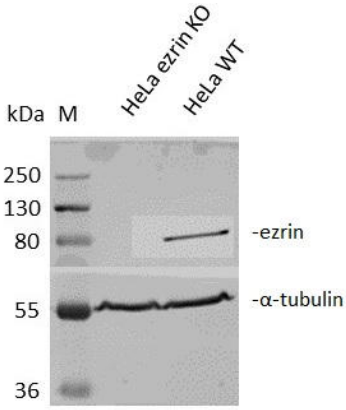

Figure 4.2: Quantification of ezrin level in HeLa WT and in HeLa ezrin$^{-/-}$ Knockout via a Western Blot.
The "M" lane shows the marker indicating different protein sizes.

Figure 4.2 shows a normalized quantity of HeLa ezrin KO cells in the middle lane, with α-tubulin at $\sim 55\,kDa$ and a normalized quantity of HeLa WT cells in the right lane, with an equal amount of α-tubulin at $\sim 55\,kDa$. Ezrin is only expressed at $\sim 80\,kDa$ in the right lane, allowing us to deduce, that the KO Cell line expresses no ezrin any more.

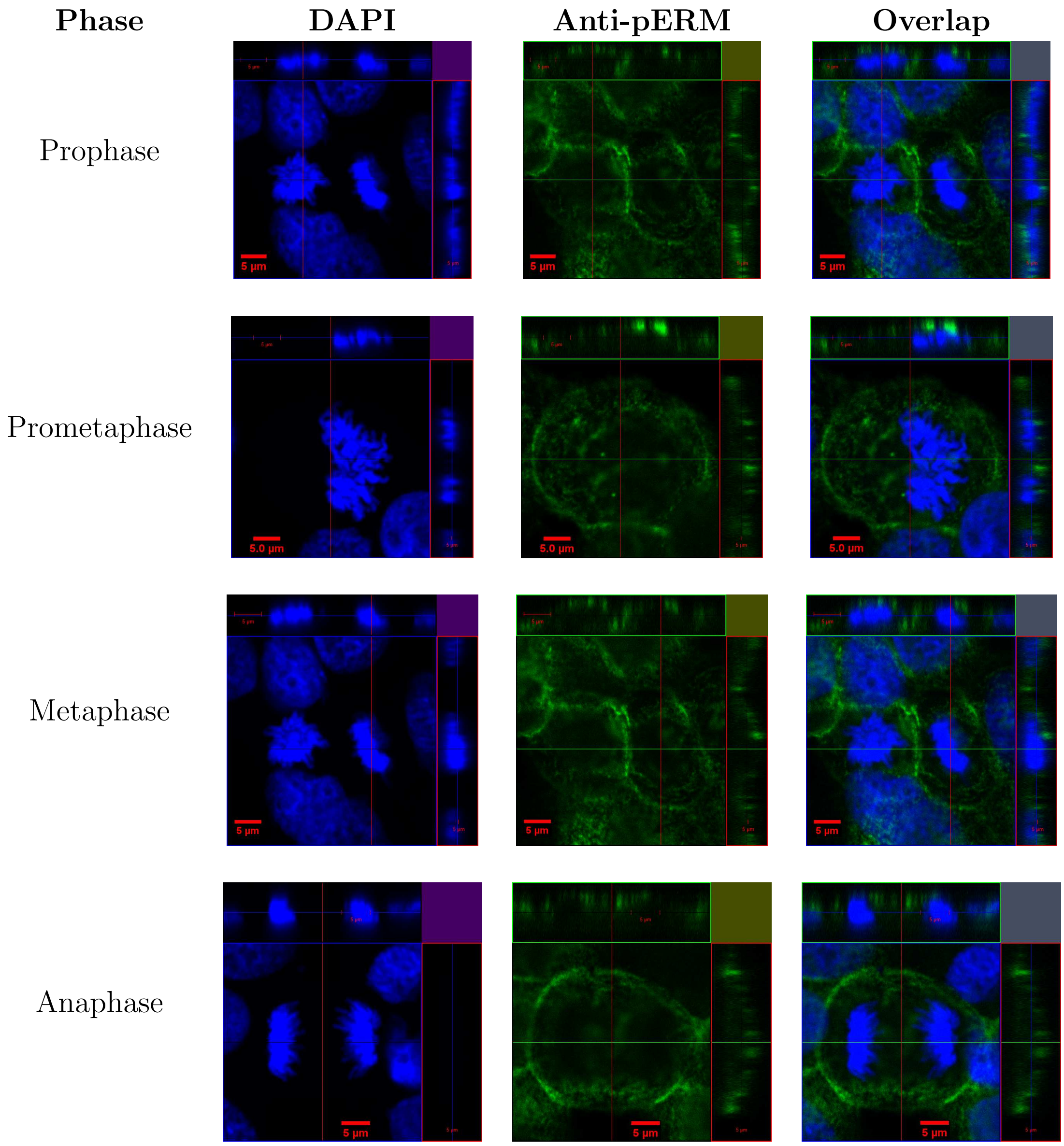

Figure 4.3: Distribution of phosphorylated RM proteins in HeLa Ezrin$^{-/-}$ Knockout cells undergoing mitosis.
DAPI (dilution 1 : 1.000) was used to visualize chromosomes in blue and RMs were detected in green with anti-pERM (dilution 1 : 100). Scale bar = 5 μm. Per image the upper left rectangle shows the frontal view, the lower left square a cut view through cells and the lower right rectangle the side view.

Figure 4.3 shows the distribution of activated RM proteins in representative selected HeLa ezrin$^{-/-}$ Knockout cells in four phases of mitosis. In prophase the RMs are ubiquitously spread in the cytosol and at the membrane (middle left cell). After the breakdown of the nuclear envelope in prometaphase, the distribution of RMs remains similar. In metaphase RMs accumulate at the cell membrane (middle right cell). This membranous concentration persists over anaphase. The unsynchronized population showed no cell in telophase, so that the ezrin localization at this phase was examined in the live cell microscopy section (see Chapter 4.3).

These results suggest no localization difference between pERM and pRM in HeLa cells.

Next, a cell model to study potential functional roles in mitosis was established. In following experiments siRNA was used to transiently knockdown all three ERMs in HeLa WT. The quality of these knockdowns was also checked in the beginning.

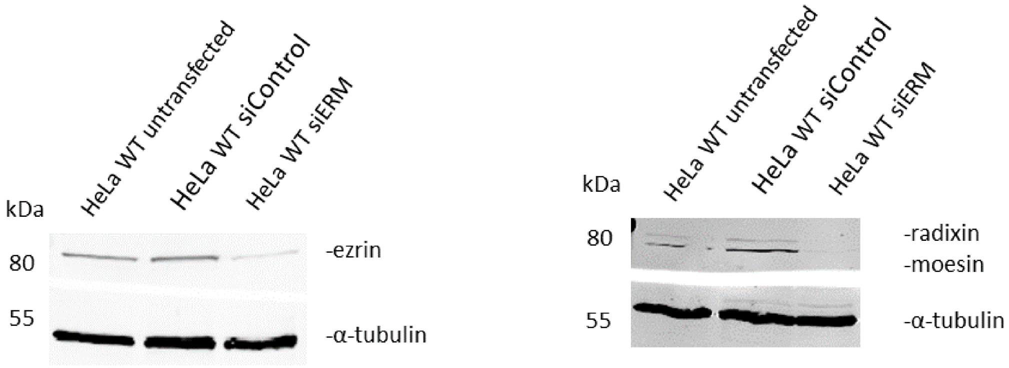

(a) (b)

Figure 4.4: Quantification of ERM levels via Western Blots in HeLa WT after siRNA treatment.
(a) Ezrin level in HeLa WT after siRNA treatment and **(b)** radixin and moesin level in HeLa WT after siRNA treatment.

Figure 4.4 shows on both western blots equal amounts of α-tubulin at $\sim 55\,kDa$, so equal amounts of cells were used for each lane. In Figure 4.4a the amount of ezrin expression persists at a similar level in HeLa WT after the transfection with siControl, whereas the transfection with siEzrin leads to a reduction of the ezrin level of $\sim$ 80 %. In Figure 4.4b the levels of radixin and moesin also stay stable in HeLa WT after the transfection with siControl, whereas the transfection with siRadixin and siMoesin leads to a reduction of the RM levels of $>$ 80 %.
This ERM expression shows the effectiveness of the performed knockdown. Knockdown effectiveness was then also analyzed by immunofluorescence microscopy.

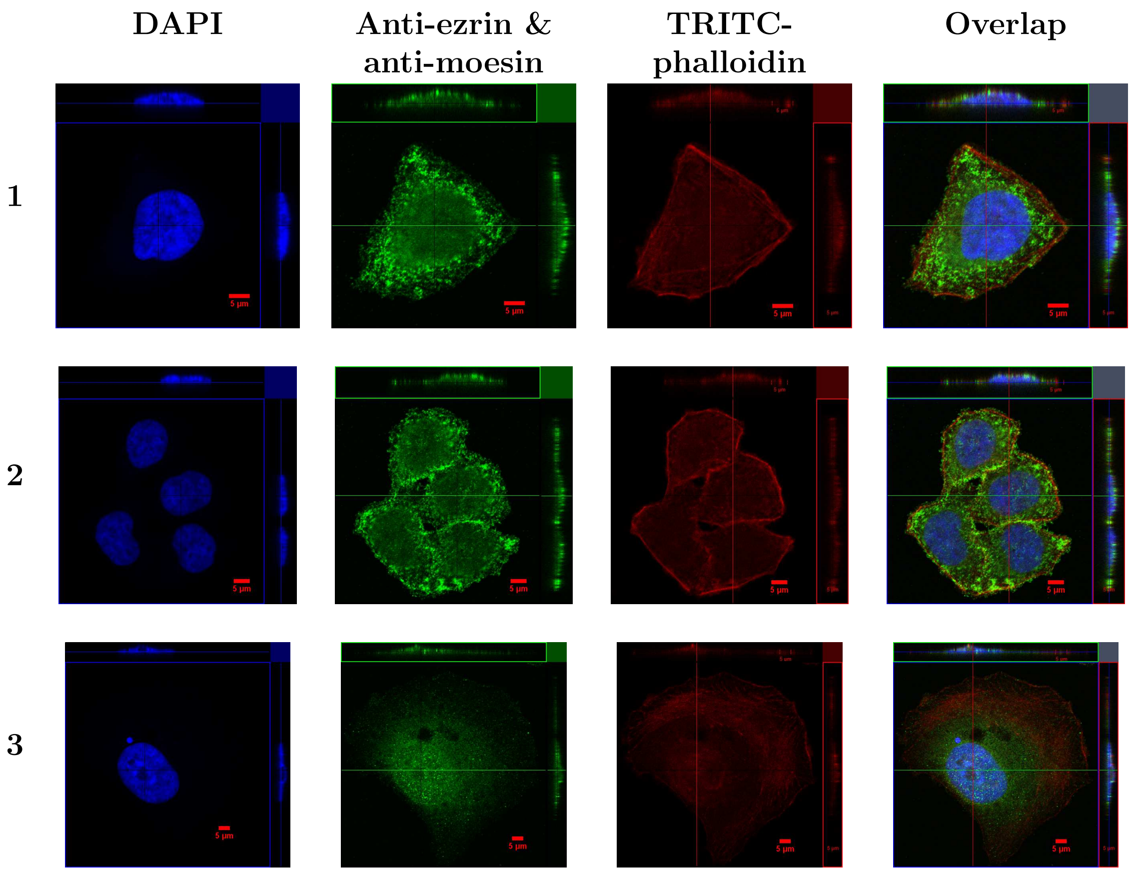

Figure 4.5: ERM levels in HeLa WT are not affected by control transfection. Each line shows representative selected HeLa WT cells. The nuclei are visualized with DAPI (dilution 1 : 1.000) in blue, ERMs are detected by using anti-ezrin (dilution 1 : 100) and anti-moesin (dilution 1 : 100), subsequently labeled by Alexa-Fluor-488 (dilution 1 : 1.000) in green. The moesin antibody is less specific and binds next to moesin also radixin. F-actin is stained with TRITC-phalloidin (dilution 1 : 1.000) in red. Scale bar = 5 μm.

Figure 4.5 shows that HeLa WT cells treated with siControl present a ubiquitous distribution of ERMs, comparable to Figure 4.1. All selected representative cells are in interphase and display an F-actin accumulation at the cell membrane.

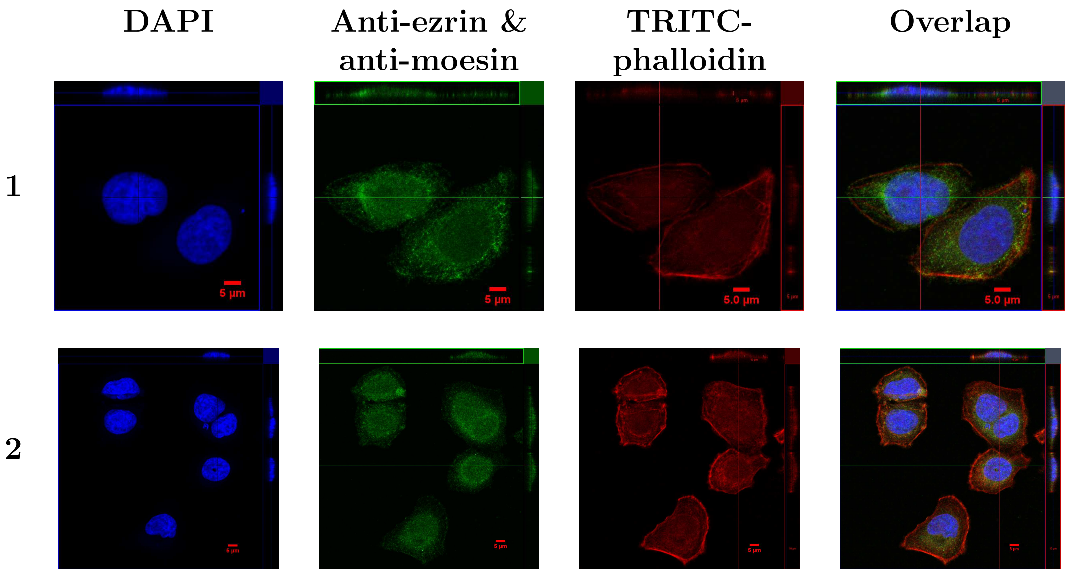

Figure 4.6: ERM levels in HeLa WT are affected by downregulation with siERM. Each line shows representative selected HeLa WT cells. The nuclei are visualized with DAPI (dilution 1 : 1.000) in blue, ERMs are detected by using anti-ezrin (dilution 1 : 100) and anti-moesin (dilution 1 : 100), subsequently labeled by Alexa-Fluor-488 (dilution 1 : 1.000) in green. The moesin antibody is less specific and binds next to moesin also radixin. F-actin is stained with TRITC-phalloidin (dilution 1 : 1.000) in red. Scale bar = 5 μm.

The selected representative HeLa WT cells transfected with siERM of Figure 4.6 show DAPI and TRITC-phalloidin signals at a level and localization similar to the cells transfected with siControl in Figure 4.5. However the signals of anti-ezrin and anti-moesin are reduced at the same excitation options for the microscope in the siERM case.

Another prominent observation is that the downregulation does not influence all cells at the same level, some more and some less. Nevertheless the microscopy images underline the effectiveness of the ERM knockdown documented above in the Western blots.

4.2 Role of ERMs in cell division: Mitotic entry

4.2.1 Cell adherence after induction of mitosis

The first cortical deformation that occurs in mitosis is the rounding-up. Therefore, interfering with cortical proteins such as ERMs could disturb this early phase in mitosis and lead to a change of cellular adhesive properties. Generally a minority of the cells undergoes mitosis at a given timepoint in an unsynchronized cell population. To test the quality of rounding-up in a large quantity of cells, ERM knockdown cells were blocked at the $G2/M$ checkpoint by nocodazole. $> 90\,\%$ of the cells are then rounded-up when studied.

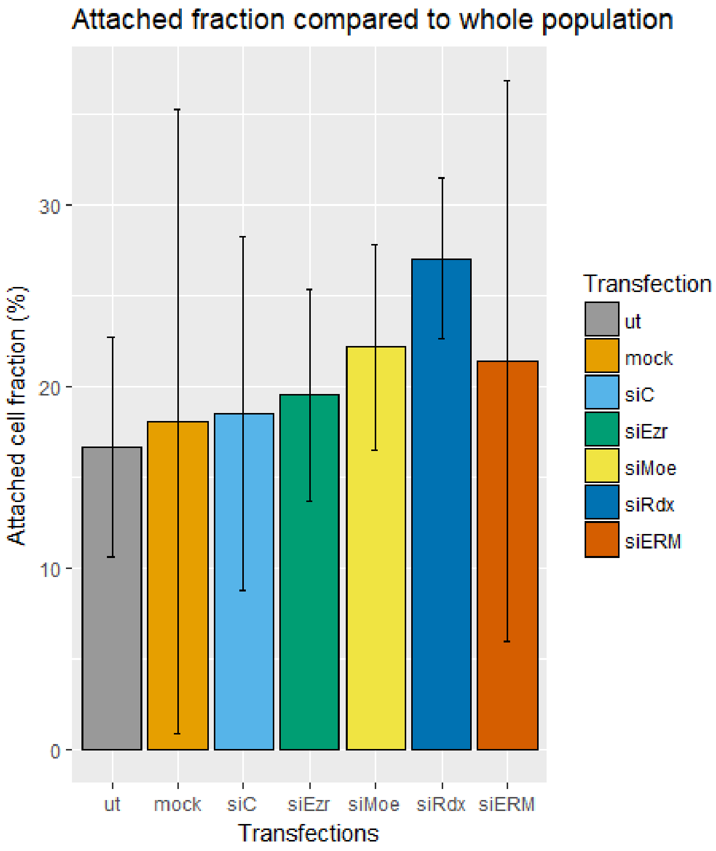

Figure 4.7: Effect of ERM depletion on cell attachment.
The mean attached fraction is displayed in comparison to the whole population. The untransfected population (ut) is represented in grey, the mock transfected population in light orange, the siControl transfected population (siC) in light blue, the siEzrin transfected population (siEzr) in green, the siMoesin transfected population (siMoe) in yellow, the siRadixin transfected population (siRdx) in dark blue and the combined SiEzrin, siRadixin and siMoesin transfected population (siERM) in dark orange. The error bars represent the standard deviation (n=3, except for mock n=2).

Those cells that round-up lose their major attachment forces and can be easily detached, so that cells can be divided into a non-rounded-up/attached fraction and a rounded-up fraction. In Figure 4.7 a slight increase of the attached fraction from $\sim 16,6\,\%$ up to $\sim 27,0\,\%$ is observed following ERM knockdown. However the standard deviations are of magnitudes that exceed each time 1/4 of each bar. Compared to the controls (ut, mock and siC), the measures for the populations siEzr, siMoe and siERM the ANOVA test defines a $p - value > 0,9$. The measurements of the siRdx population show a smaller standard deviation and a $p - value > 0,5$ compared to the controls in the ANOVA test. Thus, all changes have to be considered insignificant.

4.2.2 DNA content of cells in mitosis after ERM downregulation

After analysis of adhesion defects, potential defects in DNA segregation were examined. First, cells with non-physiological DNA content, where the chromosomes are not equally distributed to the nascent daughter cells, were assessed.
To study a synchronized cell population of HeLa cells, a nocodazole block was again performed. Next the cells were released and pursued mitosis simultaneously. Subsequently the flow cytometer separates cells in (pro)metaphase, cells with segregating chromosomes in ana- and telophase and cells after mitosis in G1. The dynamic of cell division populations, mentioned below in Chapter 4.2.3, shows when a sufficient amount of cells reaches the next detectable phase in cell division. Thus, it can be deduced that at 105 *min* after the release from nocodazole block, not all of the cells will have undergone mitosis completely. At this timepoint cell populations with DNA contents of $2n/4c$ and $2n/2c$ are observable (see [352] and Chapter 4.2.3).

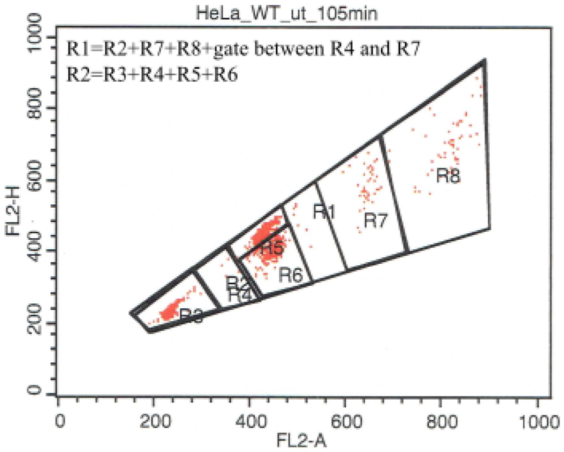

Gates		
Region	**Events**	**Gated**
R1	2411	100,00
R2	2306	95,64
R3	1099	45,58
R4	4	0,17
R5	773	32,06
R6	427	17,71
R7	42	1,74
R8	55	2,28

Figure 4.8: Different cell populations of untransfected HeLa WT separated by their DNA content, 105min after release from nocodazole block.
The column Gated is given in % and Events in total cell numbers. The gated percentage is calculated relative to the total population. R1 = all the gated cells; R2 = cells in (pro)meta-, ana- and telophase and in G1; R3 = cells in G1 with a DNA content of $2n/2c$; R4 = cells with a DNA content between G1 and (pro)meta-, ana- and telophase; R5 = cells in (pro)metaphase with a DNA content of $2n/4c$; R6 = cells undergoing cytokinesis with a DNA content of $2n/4c$; R7 = cells with $\sim$ 50 % more DNA content than R5/R6 and a multiple of $2n/4c$; R8 = cells with $\sim$ 100 % more DNA content than R5/R6 and a multiple of $2n/4c$. $n = 2500\,cells$.

The HeLa WT untransfected population (ut) (see Figure 4.8) contains at the timepoint 105 *min* 32, 06 % (R5) of the cells in metaphase, 17, 71 % (R6) in cytokinesis and 45, 58 % (R3) in $G1$. Only 4, 36 % (R1-R2) of the gated cells have non-physiological DNA amounts. 1, 74 % (R7) have 50 % more DNA than those in metaphase and 2, 28 % (R8) have 100 % more.
Thus, only few cells with an increased DNA content can be detected in the untrans-

fected case.

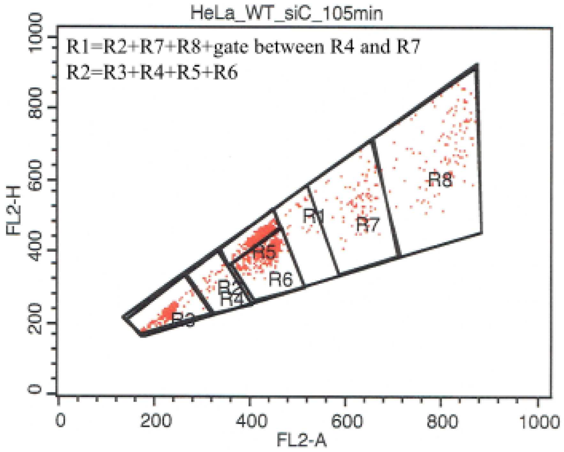

Gates		
Region	**Events**	**Gated**
R1	2208	100,00
R2	1962	88,86
R3	638	28,89
R4	33	1,49
R5	868	39,31
R6	411	18,61
R7	95	4,30
R8	128	5,80

Figure 4.9: Different cell populations of Control transfected HeLa WT separated by their DNA content, 105min after release from nocodazole block.
The column Gated is given in % and Events in total cell numbers. The gated percentage is calculated relative to the total population. R1 = all the gated cells; R2 = cells in (pro)meta-, ana- and telophase and in G1; R3 = cells in G1 with a DNA content of $2n/2c$; R4 = cells with a DNA content between G1 and (pro)meta-, ana- and telophase; R5 = cells in (pro)metaphase with a DNA content of $2n/4c$; R6 = cells undergoing cytokinesis with a DNA content of $2n/4c$; R7 = cells with $\sim$ 50 % more DNA content than R5/R6 and a multiple of $2n/4c$; R8 = cells with $\sim$ 100 % more DNA content than R5/R6 and a multiple of $2n/4c$. $n = 2500\,cells$.

The HeLa WT siControl transfected population (siC) (see Figure 4.9) contains at the timepoint $105\,min$ $39,31\,\%$ (R5) of the cells in metaphase, $18,61\,\%$ (R6) in cytokinesis and $28,89\,\%$ (R3) in $G1$. Now $11,14\,\%$ (R1-R2) of the gated cells have non-physiological DNA amounts. $4,30\,\%$ (R7) have $50\,\%$ more DNA than those in metaphase and $5,80\,\%$ (R8) have $100\,\%$ more.
Therefore, more than twice as many cells with an increased DNA amount are detectable after siC transfection than in the untransfected case, even if the total amount remains small.

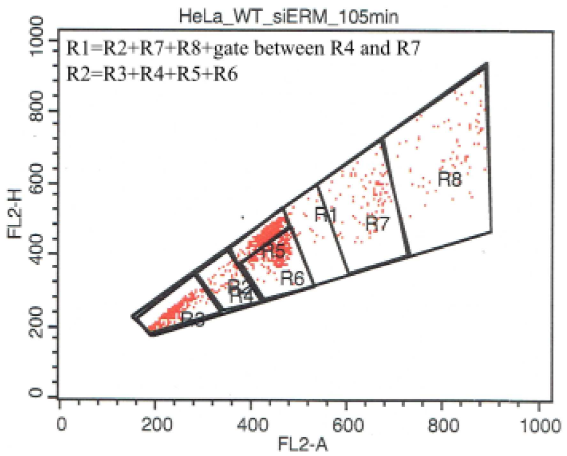

Gates		
Region	**Events**	**Gated**
R1	2098	100,00
R2	1890	90,09
R3	825	39,32
R4	46	2,19
R5	677	32,27
R6	322	15,35
R7	99	4,72
R8	86	4,10

Figure 4.10: Different cell populations of siERM transfected HeLa WT separated by their DNA content, 105min after release from nocodazole block.
The column Gated is given in % and Events in total cell numbers. The gated percentage is calculated relative to the total population. R1 = all the gated cells; R2 = cells in (pro)meta-, ana- and telophase and in G1; R3 = cells in G1 with a DNA content of $2n/2c$; R4 = cells with a DNA content between G1 and (pro)meta-, ana- and telophase; R5 = cells in (pro)metaphase with a DNA content of $2n/4c$; R6 = cells undergoing cytokinesis with a DNA content of $2n/4c$; R7 = cells with $\sim 50\,\%$ more DNA content than R5/R6 and a multiple of $2n/4c$; R8 = cells with $\sim 100\,\%$ more DNA content than R5/R6 and a multiple of $2n/4c$. $n = 2500\,cells$.

The HeLa WT siERM transfected population (siERM) (see Figure 4.10) contains at the timepoint $105\,min$ $32,27\,\%$ (R5) of the cells in metaphase, $15,35\,\%$ (R6) in cytokinesis and $39,32\,\%$ (R3) in $G1$. Now $9,91\,\%$ (R1-R2) of the gated cells have non-physiological DNA amounts. $4,72\,\%$ (R7) have $50\,\%$ more DNA than those in metaphase and $4,10\,\%$ (R8) have $100\,\%$ more.

Thus the cell number with an increased DNA amount in the siERM transfected population is also twice as high as the number in the case of untransfected cells, but is equal to the siControl case.

The comparisons are summarized in Table 4.1.

Phase	HeLa WT ut	HeLa WT siC	HeLa WT siERM
Metaphase	32,06	39,31	32,27
Cytokinesis	17,71	18,61	15,35
G1	45,58	28,89	39,32
non-physiological	4,36	11,14	9,91

Table 4.1: Cell cycle stages of different cell populations $105\,min$ after release from nocodazole block.
Numbers are given in %. 2500 cells are gated.

4.2.3 Progression of mitosis in cells with ERM downregulation

After analyzing the effect of ERM depletion on mitotic entry and chromosome segregation, I next focused on possible effects on other mitotic events. Therefore, I synchronized HeLa cells after different siRNA transfections (ut, siC and siERM) with a nocodazole block. Next I quantified the mitotic cell population in (pro)metaphase, the cytokinetic cell population and the cell population in G1 by the use of flow cytometry at different timepoints after release from nocodazole block.

HeLa WT cells:

Mitotic staging was first performed with HeLa WT ut cells to define the different populations. 7 timepoints after release from nocodazole block were chosen and the relative amount of cells in different stages of the cell cycle was determined by the FACS assay described in the Methods section (see Chapter 3.2.5.3). Results are shown in Figure 4.11a.

While the mitotic cell population (**M**) decreases almost exponentially from $99,2\,\%$ of all the cells in prometaphase at $30\,min$ to $24,3\,\%$ at $180\,min$, the population of cells after mitosis, called **G1** phase, increases almost linearly from $0,3\,\%$ at $30\,min$ to $62,5\,\%$ at $180\,min$. The number of cells undergoing cytokinesis (**C**) increases from $0,1\,\%$ at $30\,min$ to a peak value of $31,4\,\%$ at $90\,min$ and then decreases to $10,0\,\%$ at $180\,min$.

After the transfection of HeLa WT cells with siControl (see Figure 4.11b), the **M** population decreases still approximately exponentially from $96,3\,\%$ at $30\,min$ to $26,7\,\%$ at $180\,min$. The **G1** population also still increases almost linearly from $1,8\,\%$ at $30\,min$ to $65,2\,\%$ at $180\,min$ and the **C** population increases from $1,0\,\%$ at $30\,min$ to its peak value $28,1\,\%$, this time at $75\,min$. Nevertheless the value at $90\,min$ is very close to this peak value. Next the cytokinetic population shrinks again down to $7,0\,\%$ at $180\,min$.

Having established the controls and checked for the quality of the transient knockdowns (see Figure 4.4), the transient knockdown of ERMs is now accessible for evaluation (see Figure 4.11c). In the ERM knockdown cells the nearly exponential decrease of the **M** population persists; this time from $88,8\,\%$ at $30\,min$ to $29,7\,\%$ at $180\,min$. Also the close linearity of the **G1** population over time remains. It rises from $6,6\,\%$ at $30\,min$ to $60,0\,\%$ at $180\,min$. Finally the **C** population has a reduced increase, but still shows a peak. It increases from $2,2\,\%$ at $30\,min$ until $26,6\,\%$ at $90\,min$ and then decreases to $8,3\,\%$ at $180\,min$.

Clear differences in the mitotic indices of the different cell populations are not evident. Therefore Figure 4.12 and Table 4.2 summarize only the cytokinetic populations of all three conditions (ut, siC and siERM), as the cytokinesis with all its dynamics should be the most vulnerable of the phases to ERM depletion.

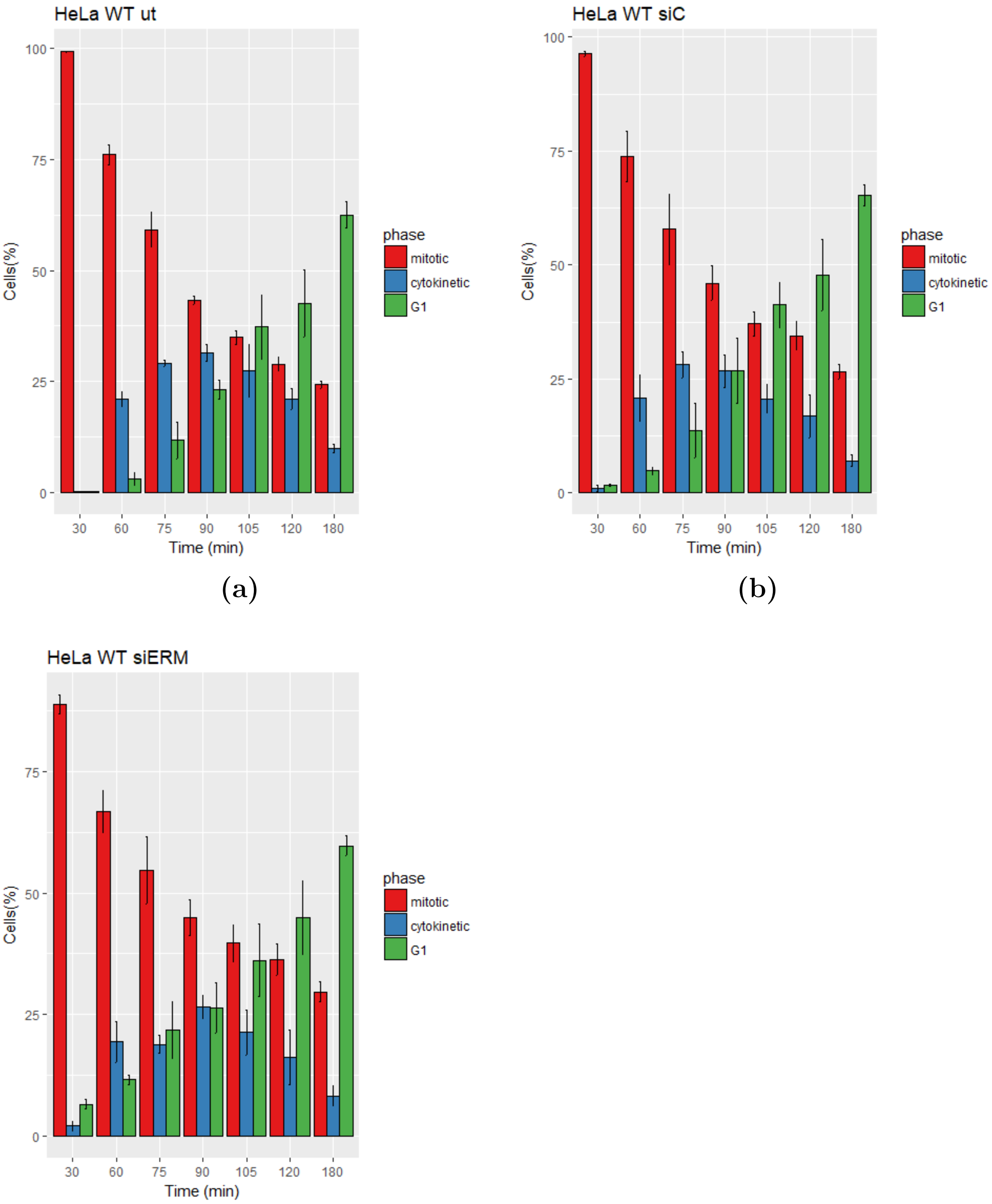

(a)

(b)

(c)

Figure 4.11: Mitosis progression of different HeLa WT populations.
(a) shows HeLa untransfected, (b) HeLa transfected with siC and (c) HeLa transfected with siERM. For each timepoint the percentage (%) of cells in the three given phases is examined. Time corresponds to time after release from nocodazole block. The mean values of the cells in metaphase are shown in the red bars, those of the cells in cytokinesis in the blue bars and those of the cells in G1 in green. The error bars correspond to the standard error. (n=3, except for ut at 30 *min* n=2).

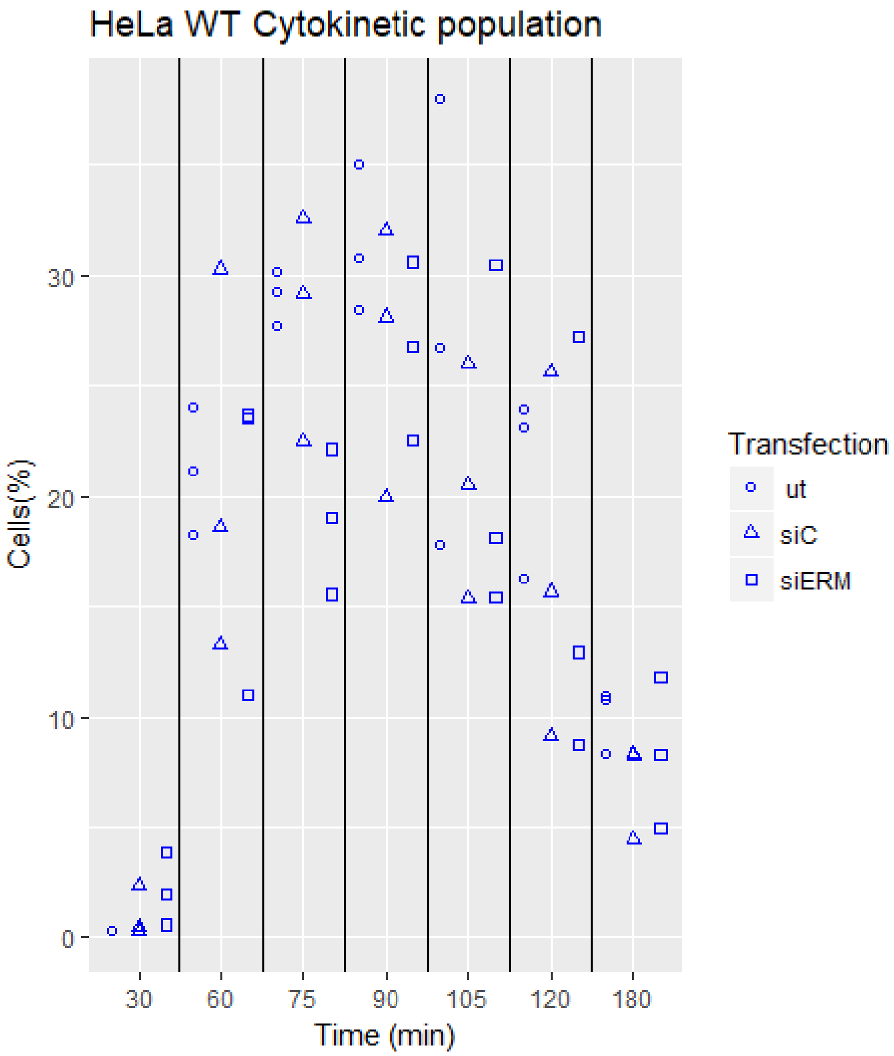

Figure 4.12: Effect of ERM depletion on the relative amount of cells in cytokinesis. The cytokinesis cell populations of Figure 4.11 are combined in this figure. Not the mean values, but each value is included. Untransfected cell populations are represented by circles, siControl transfected cell populations by triangles and siERM transfected cell populations by squares. The resolution is ∼ 0, 1%. Time corresponds to time after release from nocodazole block.

Statistics: p-Values				
Timepoint	**All 3 groups***	**siERM-siC****	**ut-siC****	**ut-siERM****
30 *min*	0,328	-	-	-
60 *min*	0,947	-	-	-
75 *min*	0,025	0,046	0,941	0,031
90 *min*	0,413	-	-	-
105 *min*	0,552	-	-	-
120 *min*	0,719	-	-	-
180 *min*	0,394	-	-	-

Table 4.2: Statistics of Figure 4.12.
Rounded to the third decimal place. *) p-Values gained with ANOVA; **) p-Values gained with Tukey.

As Figure 4.12 shows no mean values, but all of the individual values obtained,

their spreading is directly observable. In fact the values for the different cell populations are widely scattered, except for the first timepoint. The only visible difference between ut, siC and siERM can be seen at 75 *min*, when all the values of ut and siC are above those of siERM.
The assumption of normal distribution makes it possible to test the values of the three goups against each other for a significant difference. Table 4.2 indicates that at 75 *min* there is indeed a significant difference between ut and siC compared to siERM ($p < 0,05$). The post-hoc Tukey test specifies that a slighter significant difference can be calculated for siERM (siERM vs siC $p < 0,05$ and siERM vs ut $p < 0,05$).

HeLa ezr$^{-/-}$ KO cells:
The second cell line used in this thesis, generated by using the CRISPR/Cas system, possesses no ezrin and allows the analysis of possible mitotic defects of ezrin itself and RM depletion in an ezrin null background. Radixin and moesin downregulation in HeLa ezr$^{-/-}$ KO cells is shown in Figure 4.13.

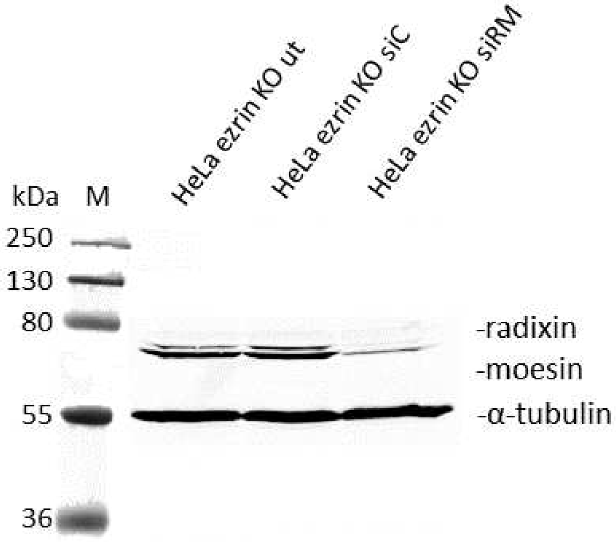

Figure 4.13: Quantification of radixin and moesin levels via a western blot in HeLa ezr$^{-/-}$ KO in mitosis assays.
The "M" column shows the marker indicating different protein sizes.

The same 7 timepoints after release from nocodazole block were chosen, where the relative amount of HeLa ezr$^{-/-}$ KO cells in different stages of the cell cycle was determined by the FACS assay. Figures 4.14a-c present the results.
All three conditions (ut, siC, siRM) of HeLa ezr$^{-/-}$ KO cells show an approximately exponential decrease for the mitotic population from 30 *min* to 180 *min*, this from respectively 97,9 % to 25,2 % (ut), 96,8 % to 30,1 % (siC) and 92,7 % to 34,6 (siRM).
The **G1** population shows in all three conditions a nearly linear increase from 30 *min*

to 180 min. The respective values are $0,7\,\%$ to $64,6\,\%$ (ut), $1,9\,\%$ to $62,6\,\%$ (siC) and $4,8\,\%$ to $56,8\,\%$ (siRM). Finally all three cytokinetic populations possess a peak value at 75 min. In the untransfected condition the population increases from $0,6\,\%$ to $33,8\,\%$ and then decreases to $9,5\,\%$. The siC population increases from $0,8\,\%$ to $33,1\,\%$ and then decreases to $6,5\,\%$. Furthermore the siRM population increases from $1,4\,\%$ to $25,4\,\%$ and then decreases to $7,2\,\%$.
Differences of the cytokinesis population are summarized in Figure 4.15 and Table 4.3.

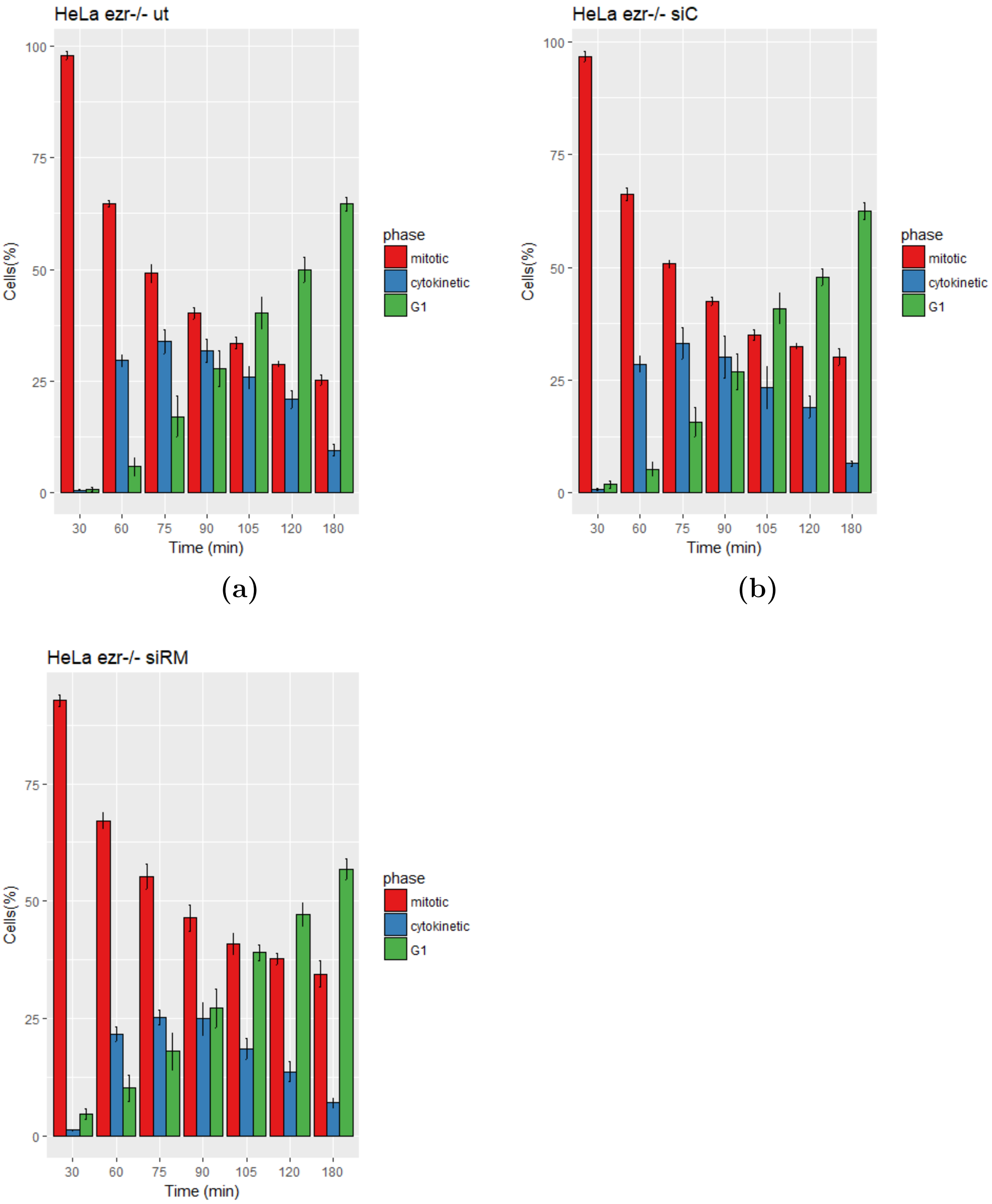

(a)

(b)

(c)

Figure 4.14: Mitosis progression of different HeLa ezr$^{-/-}$ KO cell populations. (a) shows HeLa untransfected, (b) HeLa transfected with siC and (c) HeLa transfected with siRM. For each timepoint the percentage (%) of cells in the three given phases is examined. Time corresponds to time after release from nocodazole block. The mean values of the cells in metaphase are shown in the red bars, those of the cells in cytokinesis in the blue bars and those of the cells in G1 in green. The error bars correspond to the standard error. (n=3).

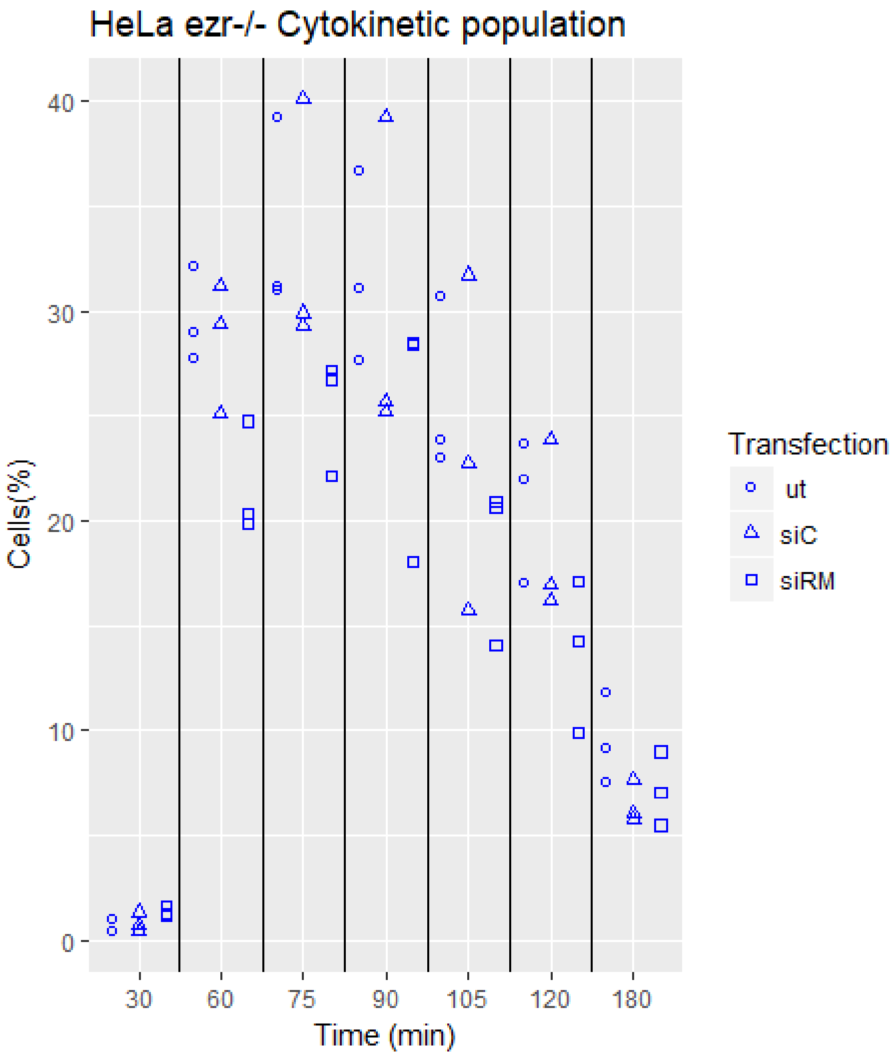

Figure 4.15: Effect of RM depletion in an ezrin null background on the relative amount of cells in cytokinesis.
The cytokinesis cell populations of Figure 4.14 are combined in this figure. Not the mean values, but each value is included. Untransfected cell populations are represented by circles, siControl transfected cell populations by triangles and siRM transfected cell populations by squares. The resolution is ~ 0,1%. Time corresponds to time after release from nocodazole block.

Statistics: p-Values				
Timepoint	**All 3 groups***	**siRM-siC****	**ut-siC****	**ut-siRM****
30 *min*	0,103	-	-	-
60 *min*	0,022	0,046	0,874	0,026
75 *min*	0,127	-	-	-
90 *min*	0,439	-	-	-
105 *min*	0,342	-	-	-
120 *min*	0,135	-	-	-
180 *min*	0,156	-	-	-

Table 4.3: Statistics of Figure 4.15.
Rounded to the third decimal place. *) p-Values gained with ANOVA; **) p-Values gained with Tukey.

Compared to the HeLa WT mitosis examination, HeLa ezr$^{-/-}$ KO cells show much closer values for each condition at each timepoint in Figure 4.15. Not only at $75\,min$, but at each timepoint apart from the first and the last, the untransfected values are very close to the values of siC, but they differ from those of siRM.
A normal distribution was again assumed and the ANOVA test could be used. Even if the p-values are much smaller than those for HeLa WT cells in Table 4.2, only at $60\,min$ $p < 0,05$. The Tukey post-hoc test shows at this timepoint, that siRM is the origin of the difference (siRM vs siC $p < 0,05$ and siRM vs ut $p < 0,05$).

4.3 Role of ERMs in cell division: Cytokinesis

All the methods that have been described above measure the quality and quantity of mitosis only indirectly. Live cell microscopy permits a direct inspection of cell divisions. However this view is restricted to quality, leaving the quantitative analysis to the sections above.
Before microscopic analysis, transfected cells were stained with Hoechst 33342. By this means the chromosomes became visible under the microscope and allowed analysis of mitosis.

4.3.1 Localization of full-length ezrin during cell division

To begin with, the localization of full-length ezrin in HeLa ezr$^{-/-}$ KO cells after expressing the GFP-ezrin DNA construct was assessed. Figure 4.16 displays a selected representative mitosis.

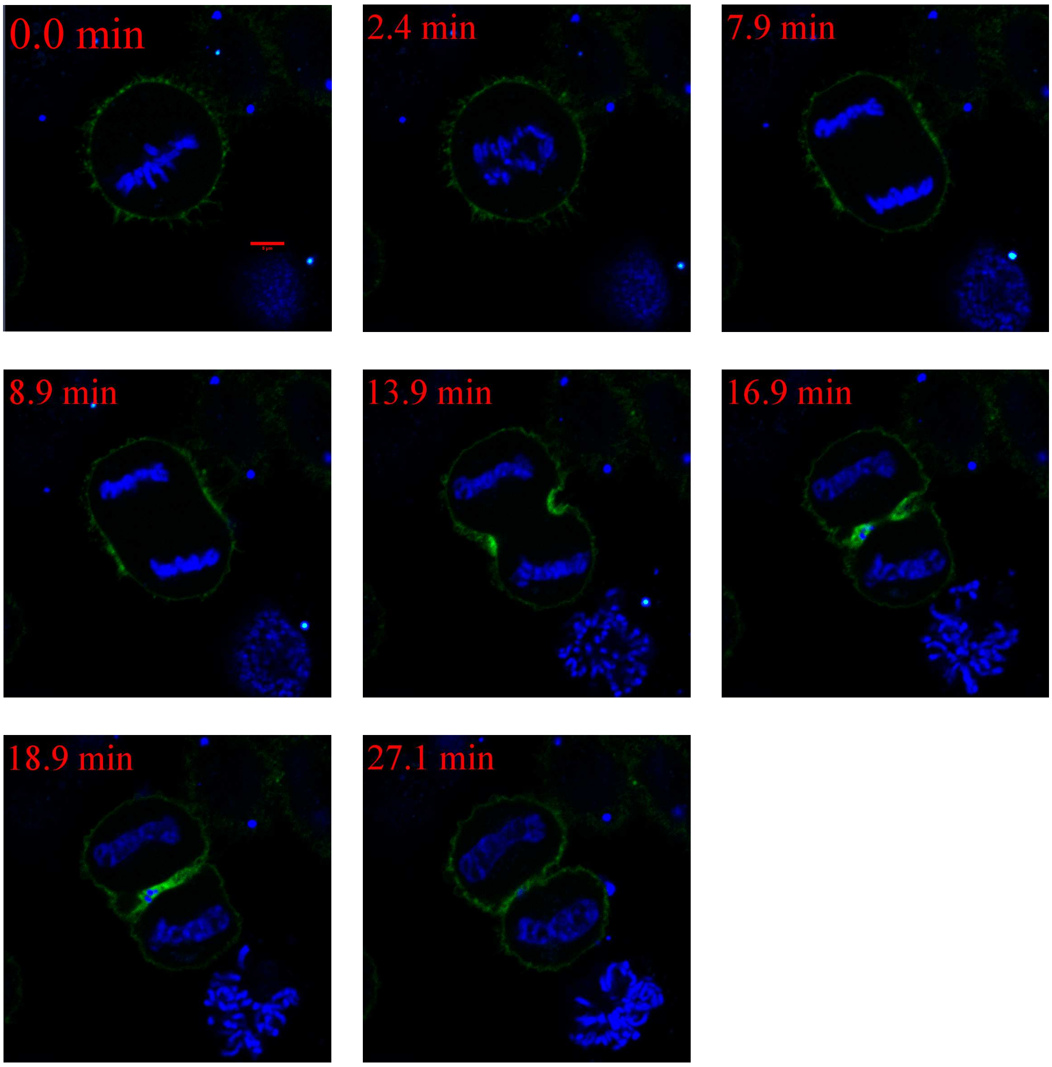

Figure 4.16:
Mitosis of HeLa ezrin$^{-/-}$ KO cells expressing GFP-ezrin.
Unsynchronized cells were analyzed. 8 representative timepoints are shown. Chromosomes are stained with Hoechst 33342 ($125\,ng/mL$) in blue. The starting point is set as $t = 0\,min$ and the total recorded time is $43,1\,min$. Scale bar = $5\,\mu m$.

The HeLa ezr$^{-/-}$ KO cell transfected with the GFP-ezrin DNA construct is at $t = 0.0\,min$ at metaphase. The chromosomes are aligned at the center and the GFP signal comes from the plasma membrane, where ezrin would also be located in HeLa WT (see Figure 4.1). Then at $t = 2,4\,min$, anaphase starts with the segregation of the chromosomes and lasts until $t \sim 7,9\,min$, when the equatorial cortex begins to form. An enrichment of GFP-ezrin at the cleavage furrow can be seen from the beginning at $t = 8,9\,min$, through $t = 13,9\,min$ and $t = 16,9\,min$, when the intracellular bridge can be imagined. Finally cytokinesis ends with the abscission at $t = 18,9\,min$. The cells flatten again ($t = 27,1\,min$) and there is no local difference in the membranous enrichment of GFP-ezrin anymore.

Thus, GFP-ezrin localizes in HeLa ezr$^{-/-}$ KO cells like endogenous ERMs in fixed

HeLa WT cells in Figure 4.1 and cell division shows no alterations in cells expressing GFP-ezrin. In HeLa ezr$^{-/-}$ KO cells only an amplified enrichment of GFP-ezrin at the cleavage furrow can be noticed.

4.3.2 Effect of an ezrin PI(4,5)P$_2$-binding mutant

The GFP-ezrin-PI(4,5)P$_2$-binding mutant constitutes an ezrin protein without the capability of binding PI(4,5)P$_2$ and thereby of binding to the plasma membrane. Figure 4.17 shows a selected representative HeLa WT cell in division after transfection with this DNA construct.

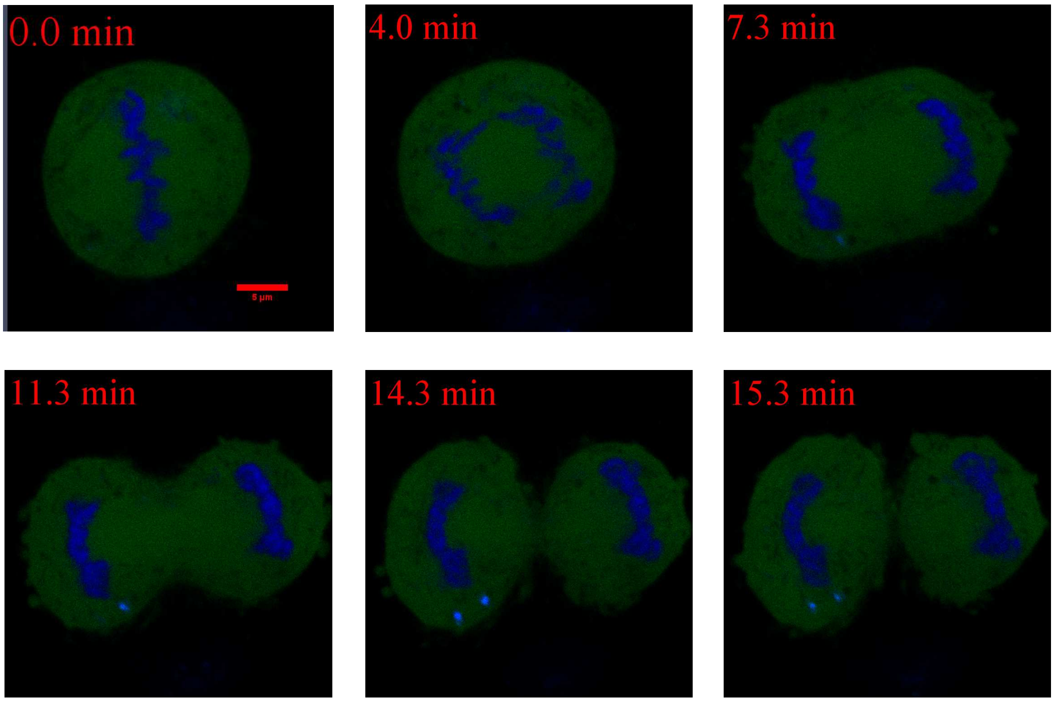

Figure 4.17:
Mitosis of HeLa WT after transfection with the GFP-ezrin-PI(4,5)P$_2$-mutant. Unsynchronized cells were analyzed. 6 representative timepoints of cytokinesis are shown. Chromosomes are stained with Hoechst 33342 ($125\,ng/mL$) in blue. The starting point is set as $t = 0\,min$ and the total recorded time is $19,8\,min$. Scale bar = $5\,\mu m$.

During the whole mitosis the GFP-ezrin-PI(4,5)P$_2$-mutant is expressed in the cytosol and the green signal of the mutant is evenly distributed.
At $t = 0$ the chromosomes are aligned at the cellular equator, so the cell is in metaphase. Then at $t = 4,0\,min$ the chromosomes start segregation, marking that way the beginning of anaphase. When the chromosomes are separated the cortex/cleavage furrow has to cut the mother cell into two nascent daughter cells. The cleavage furrow formation progresses through $t = 11,3\,min$ and $t = 14,3\,min$, when the intracellular bridge can be imagined. In ana- and telophase, from $t = 7,3\,min$ to $t = 14,3\,min$, small blebs appear. Then at $t = 15,3\,min$ the cytokinesis has

finished and two daughter cells have been formed.
Thus, cell division shows no major alterations in cells expressing the PI(4,5)P_2-binding mutant.

4.3.3 Effect of N-ERMAD overexpression

The N-ERMAD domain alone is capable of binding to the plasma membrane, but interactions with F-actin are impossible. Upon overexpression of this DNA construct, dominant-negative effects could be expected because N-ERMAD could compete with endogenous ERM proteins for plasma membrane binding. The experiments were performed in HeLa ezr$^{-/-}$ KO cells to compete with the remaining radixin and moesin and the results can be seen in Figure 4.18.

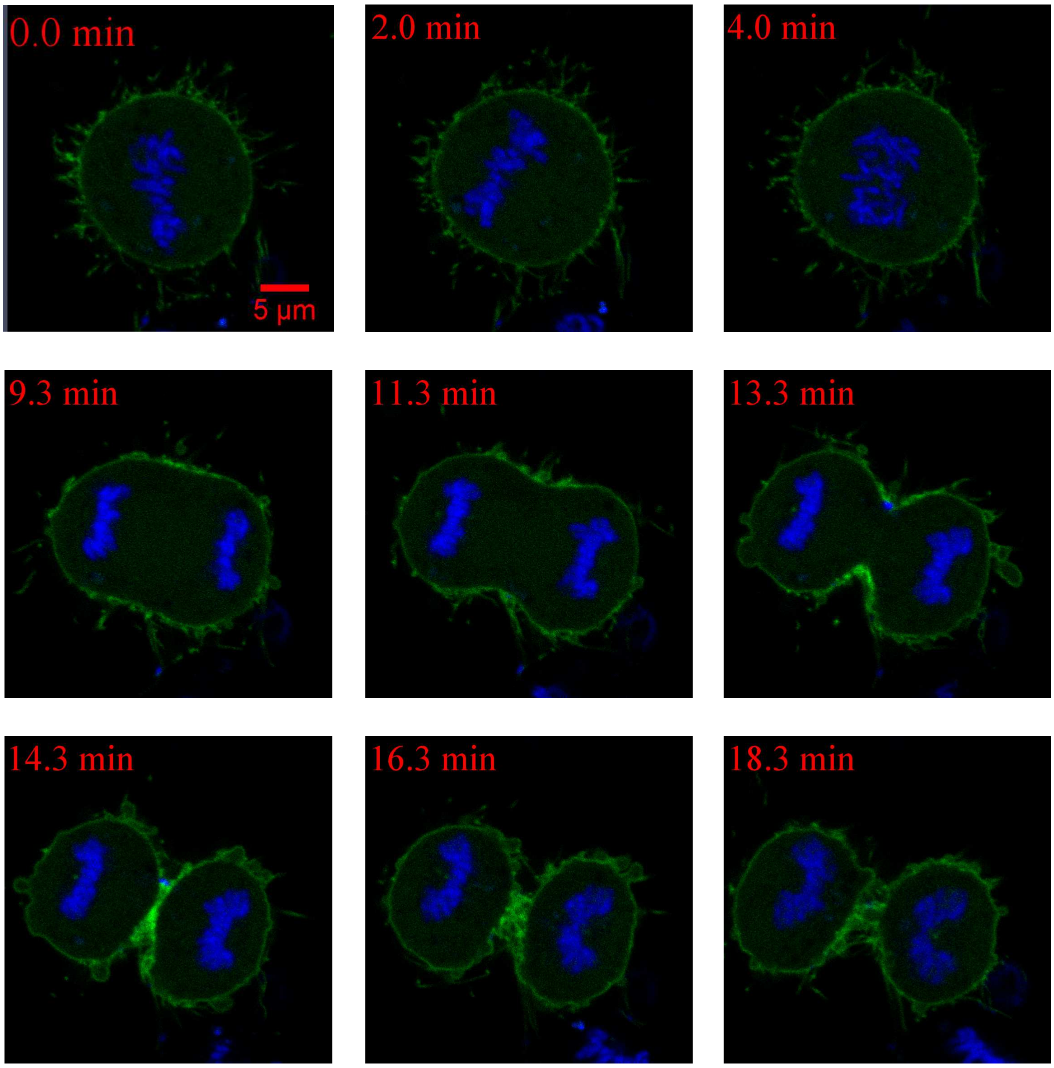

Figure 4.18:
Mitosis of HeLa ezr$^{-/-}$ KO cells after transfection with GFP-N-ERMAD.
Unsynchronized cells were analyzed. 9 representative timepoints are shown. Chromosomes are stained with Hoechst 33342 ($125\,ng/mL$) in blue. The starting point is set as $t = 0\,min$ and the total recorded time is $26,3\,min$. Scale bar $= 5\,\mu m$.

As expected, the GFP signal of GFP-N-ERMAD is enriched at the plasma membrane at all timepoints. Interestingly an increased number of protrusions and blebs of the plasma membrane are seen in N-ERMAD expressing cells at all phases of the cell cycle.
At $t = 0,0\,min$, the chromosomes are condensed, so prophase has started. $t = 2,0\,min$ later the chromosomes are still aligned at the equator. Then, shortly before $t = 4,0\,min$ the chromosomal segregation starts. At $t = 9,3\,min$ the equatorial cortex forms and the resulting cleavage furrow ingresses through $t = 11,3\,min$ and $t = 13,3\,min$ until the abscission takes place. Like the GFP-ezrin construct, an enrichment of the GFP N-ERMAD signal is apparent at the cleavage furrow. Furthermore, the plasma membrane extensions are accompanied by blebs of small and middle size, indicating cortex instability. After the abscission at $t = 16,3\,min$ and $t = 18,3\,min$, the number of blebs reduces slowly, leaving only the plasma membrane protrusions, and there is only the enrichment of GFP-N-ERMAD at the plasma membrane visible, but no local difference anymore.
The majority of HeLa ezr$^{-/-}$ KO transfected with GFP-N-ERMAD react like the selected representative cell in Figure 4.18 above, but a small minority reacts like in Figure 4.19 below:

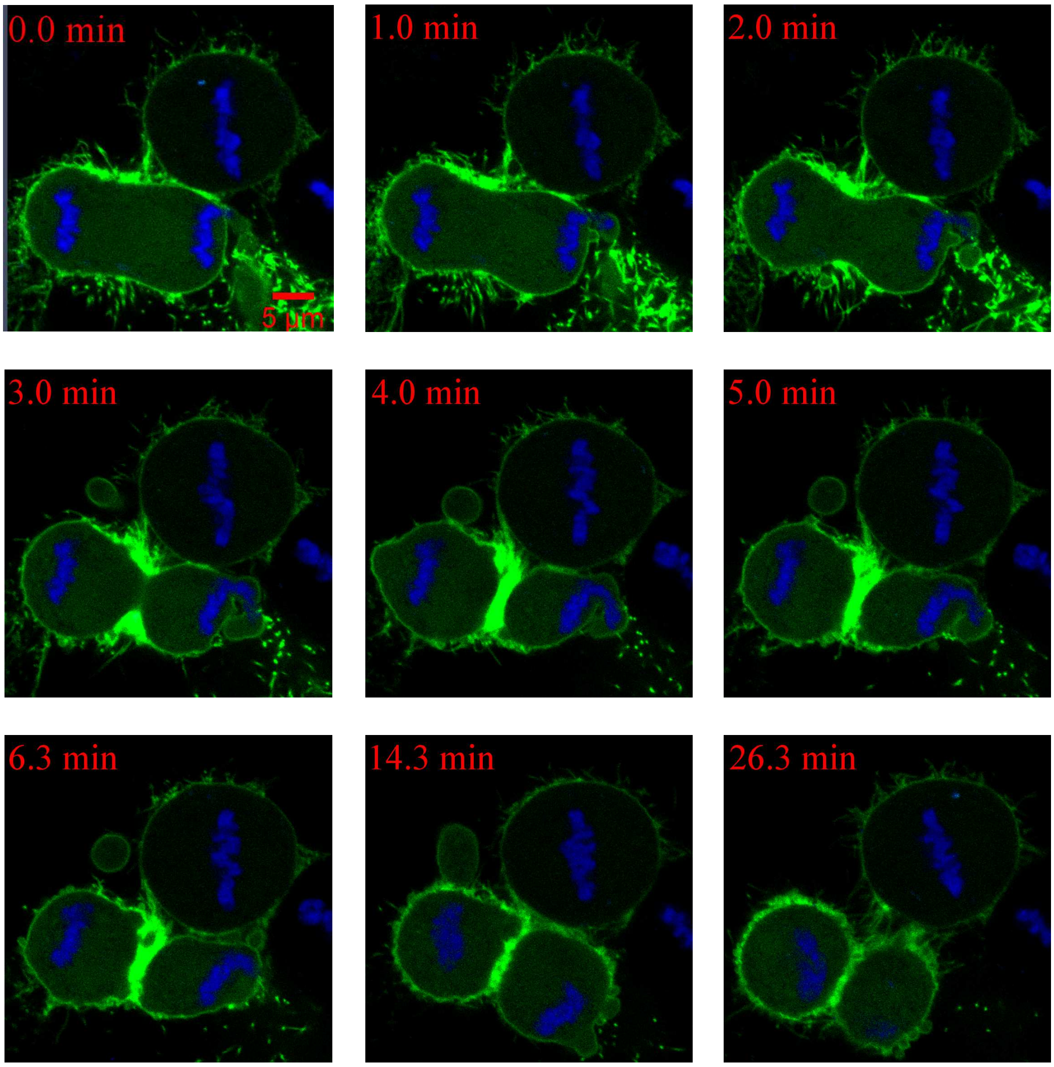

Figure 4.19:
Mitosis of HeLa ezr$^{-/-}$ KO cells after transfection with GFP-N-ERMAD.
Unsynchronized cells were analyzed. 9 representative timepoints are shown. Chromosomes are stained with Hoechst 33342 ($125\,ng/mL$) in blue. The starting point is set as $t = 0\,min$ and the total recorded time is $38,3\,min$. Scale bar = $5\,\mu m$.

Figure 4.19 shows another example of a cell division of HeLa ezr$^{-/-}$ KO cells after transfection with GFP N-ERMAD. The plasma membrane protrusions are larger and give a thicker signal from $t = 0\,min$ to $t = 2,0\,min$. From $t = 3,0\,min$ to $t = 14,3\,min$ a huge bleb can be seen at 12 o'clock from the left chromosomes. In addition a second major bleb is observable from $t = 3,0\,min$ to $t = 5,0\,min$ at 3 o'clock from the right chromosomes. 1/3 of HeLa ezr$^{-/-}$ KO cells expressing GFP N-ERMAD displays blebs of a similar, huge size, indicating an even greater cortical instability than the cell in Figure 4.18.

4.3.4 Analysis of chromosome segregation in dividing cells

Next I performed a more detailed analysis of the kinetics and morphological aspects of chromosome segregation in HeLa ezr$^{-/-}$ KO cells expressing GFP-ezrin or GFP N-ERMAD.

4.3.4.1 Kinetics of chromosome segregation

Two different periods were defined: observations start in metaphase, just before the cell enters anaphase and the chromosomes begin segregating. Therefore one period (a) lasts from the start of segregation until the mitosis finishes. The second period (b) lasts from just before the ingression of the cleavage furrow until the abscission. The latter period corresponds to the time needed for cytokinesis.

Time for ...	**a)Segregation & Ingression**	**b)Ingression**
HeLa ezr$^{-/-}$ KO	$16,11$	$9,71$
transfected with GFP-ezrin (n=21)		$60,3\,\%$ of (a)
	$SD = 3,76$	$SD = 2,69$
HeLa ezr$^{-/-}$ KO	$12,35$	$6,58$
transfected with GFP-N-ERMAD (n=30)		$53,3\,\%$ of (a)
	$SD = 2,81$	$SD = 2,15$

Table 4.4: Kinetics of chromosome segregation in HeLa ezr$^{-/-}$ KO cells expressing different DNA constructs.
Mean values of the time needed for chromosomal segregation and ingression in different transefection cases are determined (in min). n = cell number and SD = standard deviation.

In table 4.4, HeLa ezr$^{-/-}$ KO cells transfected with GFP-ezrin take a mean period of $16,11\,min$ (with the extreme values $8\,min$ and $20,37\,min$) for the segregation and the ingression, while they take $9,71\,min$ for cytokinesis (with the extreme values $4\,min$ and $13\,min$). In comparison HeLa ezr$^{-/-}$ KO cells expressing GFP N-ERMAD are analyzed for dominant-negative effects. These cells have almost the same duration for both periods, segregation and ingression needing $12,35\,min$ (with the extreme values $9\,min$ and $15,36\,min$) and cytokinesis requiring $6,58\,min$ (with the extreme values $4\,min$ and $11\,min$.

Furthermore, the part that period (b) takes of period (a) is higher for HeLa ezr$^{-/-}$ KO cells transefected with GFP-ezrin than for HeLa ezr$^{-/-}$ KO expressing GFP N-ERMAD ($60,3\,\%$ vs $53,3\,\%$).

Thus, the extreme range of the time measurements results in insignificant changes between the different conditions.

4.3.4.2 Morphological analysis of chromosome segregation

Morphological aspects of chromosome segregation were analyzed by measuring different lengths in mitosis that are specified in Figure 4.20.

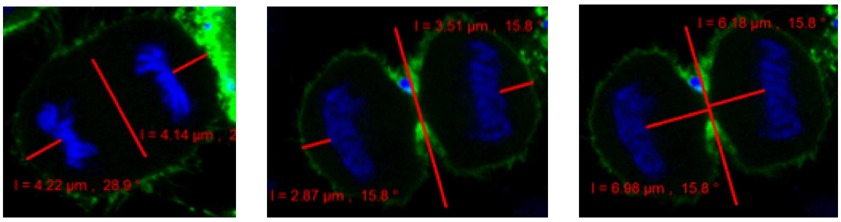

(a) (b) (c)

Figure 4.20: Measurement of specific distances
a) chromosomal distance to the cortex in anaphase; b) chromosomal distance to the cortex in telophase; c) chromosomal distance to the equator in telophase. Chromosomes stained with Hoechst 33342 ($125\,ng/mL$) in blue. In these specific images the membrane and the underlying cortex are stained in green after the transfection with GFP-ezrin.

In anaphase the distance between the chromosomes and the cortex was measured, while in telophase the distances from the chromosomes to both the cortex and the equator were measured.

First the chromosomes from one side are compared to the ones of the other side of the cell equator. Next the ratios obtained are averaged according to:

$$\frac{\sum_{i=1}^{n}\frac{left_i}{right_i}}{n} \tag{3}$$

with $left < right$ and $n = cell\,number$.

or

$$\frac{\sum_{i=1}^{n}\frac{right_i}{left_i}}{n} \tag{4}$$

with $right < left$ and $n = cell\,number$.

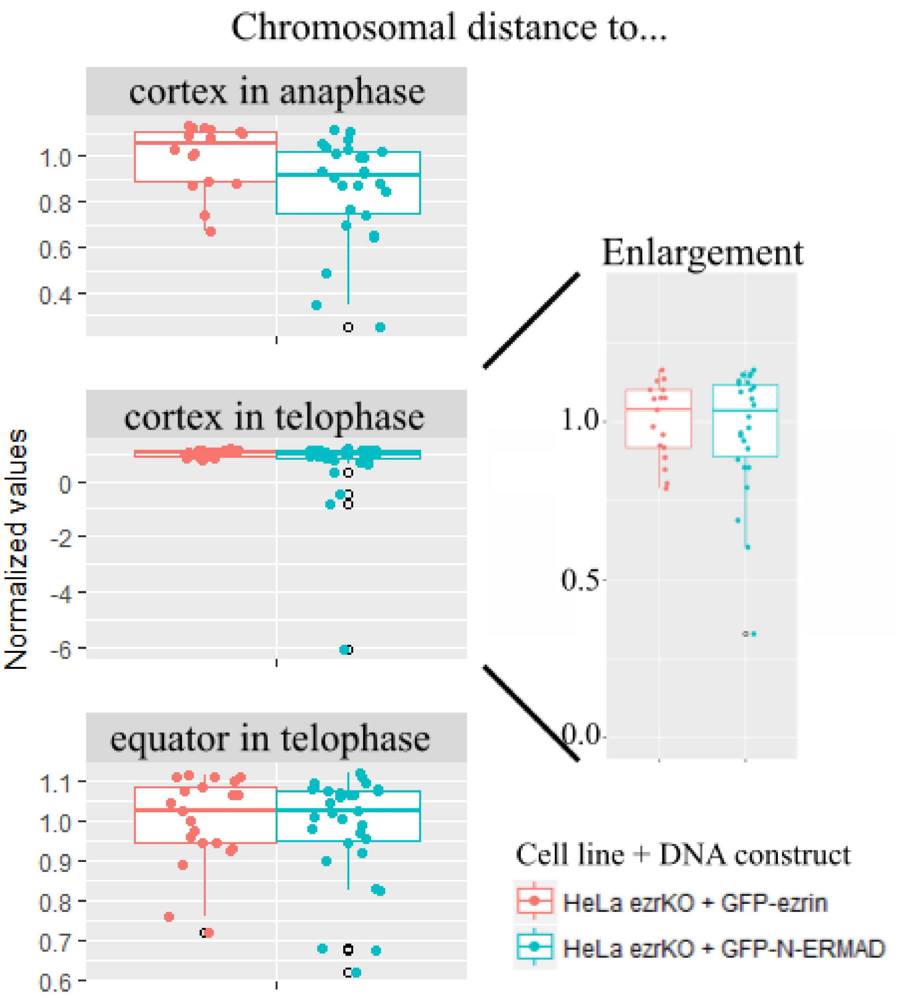

(a)

Chromosomal Distance to ...	HeLa ezr$^{-/-}$ KO transfected with GFP-ezrin (n=18)	HeLa ezr$^{-/-}$ KO transfected with GFP N-ERMAD (n=30)
Cortex in Anaphase	0,87	0,74
Cortex in Telophase	0,85	0,79
Equator in Telophase	0,87	0,85

(b)

Figure 4.21: Relative chromosomal positioning to each other in HeLa ezr$^{-/-}$ KO cells expressing GFP-ezrin or GFP N-ERMAD.
The positioning of the segregating chromosomes is analyzed by the ratios between the left and the right chromosomes according to formulas (3) and (4). **(a)** The top boxplot displays the chromosomal distance to the cortex in anaphase, the middle boxplot represents the chromosomal distance to the cortex in anaphase and the bottom boxplot shows the chromosomal distance to the equator in telophase. Each boxplot has a median line in the middle, notches according to $median + / - 1,58 * inter - quantile\,range\,(IQR)/sqrt(n)$ and hinges coinciding with the 25 %, respectively the 75 % quantile. Extreme values are displayed as circles with a black margin. Values are normalized to the mean value of HeLa ezr$^{-/-}$ KO cells transfected with GFP-ezrin for each distance condition. **(b)** The table shows the absolute mean values for each condition and indicates the number of cells observed. $n = cell\,number$.

Figure 4.21 shows that the values differ over a large range in each condition. First I assessed the chromosomal positioning relative to the chromosomes of the other side of the cell equator in HeLa ezr$^{-/-}$ KO cells expressing GFP-ezrin or GFP N-ERMAD. Thereby the chromosome segregation is analyzed for its morphological symmetry over time to the equator. In anaphase a reduction of this symmetry of $0,15$ in the mean and median values can be noticed by replacing the GFP-ezrin construct by GFP N-ERMAD.

However in telophase the median values of both conditions are similar and the mean value only reduces by $0,06\,\%$ after expressing GFP N-ERMAD. The cortical instability induced by N-ERMAD, which has been discussed above (see Chapter 4.3.3), can lead to bleb formation around chromosomes and subsequently to negative values, as I determined the bleb neck as limit of the plasma membrane.

The distances to the equator between the right and the left chromosomes result in telophase in very similar ratios between both transfection cases. The mean and median values are almost equal for the GFP-ezrin transfection and the GFP N-ERMAD transfection.

A second view could be given by considering the left and right segregating chromosomal parts as independant, doubling that way the distances measured (see Figure 4.22).

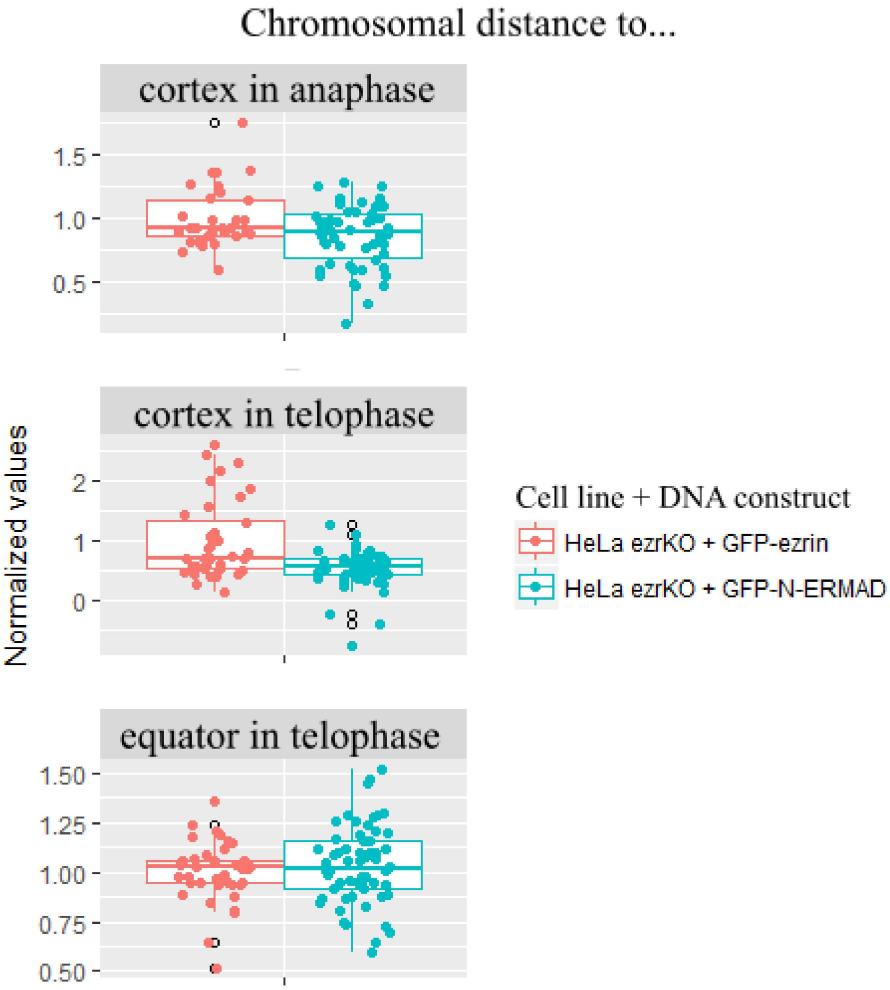

(a)

Chromosomal Distance to ...	HeLa ezr$^{-/-}$ KO transfected with GFP-ezrin (n=18)	HeLa ezr$^{-/-}$ KO transfected with GFP N-ERMAD (n=30)
Cortex in Anaphase	1, 00	0, 86
Cortex in Telophase	1, 00	0, 85
Equator in Telophase	1, 00	1, 03

(b)

Figure 4.22: Absolute chromosomal positioning in HeLa ezr$^{-/-}$ KO cells expressing GFP-ezrin or GFP N-ERMAD.
The positioning of the segregating chromosomes is analyzed by the absolute values measured without comparing right to left. **(a)** The top boxplot displays the chromosomal distance to the cortex in anaphase, the middle boxplot represents the chromosomal distance to the cortex in anaphase and the bottom boxplot shows the chromosomal distance to the equator in telophase. Each boxplot has a median line in the middle, notches according to $median +/- 1,58 * inter - quantile\, range\, (IQR)/sqrt(n)$ and hinges coinciding with the 25 %, respectively the 75 % quantile. Extreme values are displayed as circles with a black margin. Values are normalized to the mean value of HeLa ezr$^{-/-}$ KO cells transfected with GFP-ezrin for each distance condition. **(b)** The table shows the normalized mean values for each condition and indicates the number of cells observed. Values are again normalized to the mean value of HeLa ezr$^{-/-}$ KO cells transfected with GFP-ezrin. $n = cell\, number$.

This second analysis in Figure 4.22 shows that the total cortical distances measured per condition have smaller mean values for HeLa ezr$^{-/-}$ KO cells with the GFP N-ERMAD DNA construct than HeLa ezr$^{-/-}$ KO cells expressing GFP-ezrin have. However the median values are marginally smaller for the GFP N-ERMAD transfection. The elongation of the distance between the chromosomes and the cortex in ana- and telophase by $\sim 15\,\%$ after the expression of GFP N-ERMAD, compared to the GFP-ezrin construct, is not accompanied by an extension of the measurements from the chromosomes to the equator.

Finally the depletion of functional ERMs by N-ERMAD expression does not disturb the symmetry of the chromosomal segregation. However, a loss in functional ERMs seems to reduce the distance symmetrically between the chromosomes and the cellular cortex.

5 Discussion

Cellular changes on a morphological level require an adaptable cortex. Therefore the cytoskeleton is built of self-organizing components [97–99]. That way lamellipodial [160], blebbing [173–175, 188] and lobopodial [156, 196] movements are enabled next to microvilli formation [207, 208], rounding-up in pro- and metaphase [228] and cytokinesis [255]. To allow all these deformations, the plasma membrane has to be anchored to the cortex by well known proteins such as anillin and ERMs. In our laboratory group the enrichment of ezrin at the cleavage furrow was noticed, an observation corresponding to the early findings of Sato for radixin [63]. As the interaction of anillin in binding the contractile ring to the plasma membrane is crucial for cytokinesis [299], we hypothesized that the enrichment of ERMs at the cleavage furrow indicates a yet unknown role of ERMs in influencing the furrow ingression. Furthermore, the analysis of cytokinesis allows the inspection of further roles of the ERMs in mitosis before and after cytokinesis.

5.1 Cell adherence after induction of mitosis could involve all 3 ERMs

At mitotic entry the sterile 20-like kinase (SLK) activates ERMs [244], so that the crosslinking proteins can ensure the uniform distribution of the cortical tension in the rounding-up [224].

Therefore the transient knockdown of ezrin, radixin and moesin could lead to a decrease in cortical tension and subsequently a lack of rounding-up. We transfected HeLa WT separately and combined with siRNA targeting ERMs to not only check the overall role of these proteins in the process, but also to evaluate the supposed redundant roles between the family members [12]. In fact the individual knockdowns of ezrin, radixin and moesin show a slightly different reaction in the cells, with siRdx inducing the fewest rounding-up. However as our results differ widely for the untransfected cells and the mock and control transfected cells, no conclusion can be drawn on the question raised.

Remaining questions that further studies have to answer are 1) if the knockdown of ERMs impedes rounding-up at mitotic entry, 2) if siRNA itself influences the deformation and not the knockdown of proteins and 3) if ERMs and siRNA both interfere with morphogenesis at this timepoint.

5.2 Effect of ERM downregulation in chromosome segregation

In Drosophila melanogaster, the knockdown of its only ERM protein, dmoesin [66], leads to ectopic poles [250]. One explanation is that ERMs promote the polarized association of the LGN and the NUMA proteins, which are essential for spindle orientation [244]. In addition, the controlled softening of the cortex in mid anaphase is based on only locally polar dephosphorylation of ERMs [341].

Independantly of the already mentioned roles of ERMs in mitosis, the analysis of the cells after cell division should reveal any other defects, possibly related to chromosome mis-segregation in mitosis.

The Figures 4.8, 4.9 and 4.10 show the DNA content of HeLa WT cells $105\,min$ after nocodazole block release. Table 4.1 gives a summary. As the cell populations in metaphase and cytokinesis have not finished mitosis, post-mitotic differences are only detectable in the G1 cell population. While there are $45,58\,\%$ of the cells in G1 in the untransfected condition, the control transfection leads to a reduction to $28,89\,\%$ and the siERM transfection to a small decrease to $39,32\,\%$. Physiologically the cells have a ploidy of $2n/2c$ or $2n/4c$. Here HeLa WT ut shows $4,36\,\%$ of the cells with more chromosomal content. This is increased in HeLa WT siC and HeLa WT siERM cells to $\sim 10\,\%$. So even if the number of multinucleated cells more than doubles after the transient knockdown of ERMs, the transfection with siC does so too. Therefore an increase in DNA content is the result of the transfection process and not of the decrease in ERM expression.

Even if erroneous spindle building and ectopic poles have been observed in the absence of ERM proteins [250], these defects don't seem to end up in aneuploidy or other DNA content modification. These results are supported by early tests in the 1990s [359], where cells with more than two nuclei were also hardly seen after the addition of antisense oligonucleotides complementary to ERM sequences.

5.3 Effect of ERMs on kinetic and morphological aspects of mitosis

For the analysis of mitosis, and more accurately the cytokinesis, we chose two effective methods: 1) The flow cytometry method established by Gasnereau [352] gives a quantitative view on cytokinesis, while 2) live cell microscopy explores on a qualitative level.

5.3.1 ERMs accelerate the progression of cytokinesis

The mitosis assays shown in Figure 4.12 reveal a clear visible reduction of cells in the cytokinesis population for $t = 75\,min$ for the triple knockdown compared to the controls. The ANOVA test reveals a p-Value of $0,025$. All other timepoints have $p > 0,3$.
Also for HeLa ezr$^{-/-}$ KO only one timepoint, $t = 60\,min$, is statistically significant with a p-value of $0,022$. However visible differences at $t = 60\,min$, $t = 75\,min$, $t = 105\,min$ and $t = 120\,min$ are seen for individual values in Figure 4.15, albeit not being statistically significant with the low number of experiments.
After the detection of the decrease in cytokinetic population, two possibilities have to be examined; either the cytokinesis is speeded up, so that fewer cells are in this process per timepoint and the G1 population increases rapidly, or there is a slow-down marked by a high amount of cells in metaphase **M** that need longer to commit themselves to anaphase and the following chromosomal segregation. Actually Figures 4.11a-c are again less conclusive than Figures 4.14a-c, but the latter show a clear increase in the **M** population from the controls to the double knockdown in HeLa ezr$^{-/-}$ KO, combined with a correspondent decrease in **G1**. However Hiruma et al. described no 'gross influence' of ERMs on the progression of furrow ingression [342]. This difference might be due to the methods used. While they used only live cell imaging to gain an overview on the progression of cytokinesis, this thesis uses flow cytometry in addition to live cell microscopy (Chapter 5.3.2). Thereby not only ~ 100 cells are observed, but 10.000 cells are measured for each condition. Even if no 'significant contribution to the progression of furrow ingression during cytokinesis in HeLa cells' [342] is described in literature, we could show hereby, that ERMs do have an impact on the progression.
But why is there a difference between HeLa WT cells suffering a triple knockdown and HeLa ezr$^{-/-}$ KO cells experiencing a double knockdown? An explanation could be the expression levels of ezrin, radixin and moesin. A transient knockdown performed with siRNA (almost) never eradicates completely the target proteins. Thus, in our experiments, HeLa WT siERM cells still possess $\sim 20\,\%$ of the wildtype levels of ezrin, radixin and moesin. In contrast, HeLa ezr$^{-/-}$ KO cells show no ezrin expression ($0\,\%$) and radixin and moesin remain again $\sim 20\,\%$ of the wildtype expression levels. Thus, HeLa ezr$^{-/-}$ KO siRM cells express in total less ERMs than HeLa WT siERM cells.
However it has to be noted that I only analyzed one clone of the CRISPR/Cas gen-

erated HeLa ezr$^{-/-}$ KO cell line. Thus, the possibility persists that the presented results are due to a cellular alteration originating from the CRISPR/Cas method.

5.3.2 Individual analysis of cells revealed morphological alterations upon active ERM downregulation

Among the multitude of observations described in literature for cytokinesis after the manipulation of cortex to membrane anchoring proteins, D'Avino et al. presented unusual F-actin formations and an abnormal accumulation of anillin in cytokinesis, associated with blebbing and multinucleation, after the downregulation of the sole CIT-K homologue in drosophila [295]. Upon moesin depletion, F-actin and Myosin II are distributed irregularly and not restricted to the division equator in a way that the cortical integrity and rigidity are impaired. Moreover, the indirect switch-off by SLIK inactivation provokes transient cytoplasmatic blebs [43]. Furthermore, a poor association of ERMs with the contractile ring was proven. The authors also found that anillin and supervillin limit the access of ezrin to the cleavage furrow and the localization of ERMs at the cleavage furrow is regulated separately from Rho mediated pathways [342].
Thus, the blebs observed in Chapters 4.3.2 & 4.3.3 in HeLa ezr$^{-/-}$ KO cells transfected with N-ERMAD correspond to such reports. In comparison the reexpression of ezrin in HeLa ezr$^{-/-}$ KO cells displays no morphological alterations in mitosis in live cell microscopy. N-ERMAD most likely acts in a dominant negative manner, interfering with the remaining ERMs, radixin and moesin. Therefore, N-ERMAD, unable to bind F-actin alone, should strongly mimick the eradication of ERMs. Thus, the inactivation of SLIK, which operates above dmoesin, shows a similar blebbing to HeLa ezr$^{-/-}$ KO with N-ERMAD. Furthermore, the blebs of small sizes concerning the PIP$_2$ DNA construct also show the importance of functioning ERMs. The plasma membrane protrusions and extensions described earlier (Chapter 4.3.3) go along with a misdistribution of F-actin and Myosin II after dmoesin depletion. This is further supported by the discovery that active ERMs lead to MYOGEF (myosin II-interacting guanine nucleotide exchange factor) localization at the plasma membrane [193].

Kinetic inspections of cell divisions under the microscope revealed in Drosophila melanogaster that in the absence of dmoesin or SLIK anaphase onset is delayed [43]. However, no 'gross' contribution to the progression of furrow ingression during cytokinesis upon siERM treatment in HeLa WT has recently been described [342]. In this thesis I tried to minimize the energy put into the cell by the laser of the microscope, by choosing a rate of 1 image every $2-4\,min$. Therefore a high uncertainty remains on the quality of the starting point. Even if some uncertainties exist with respect to the start of mitosis, this work got no significant effect by analyzing individual cells.

I also analyzed whether the expression of GFP N-ERMAD in an ezrin null background affects the positioning of the chromosomes. In literature spindle length alerations and subsequent altered chromosome positioning upon dmoesin depletion are mentioned [43]. In Figure 4.21 the symmetry of the chromosomal segregation is analyzed while Figure 4.22 shows the overall positioning of the chromosomes. Overall the distances are in each condition heterogeneously spread.
HeLa ezr$^{-/-}$ KO cells transfected with GFP-ezrin present a certain asymmetry between their right and their left segregating chromosomes. Compared to this, HeLa ezr$^{-/-}$ KO transfected with GFP-N-ERMAD shows only marginal differences. Even if the latter condition possesses a chromosomal distance to the cortex in anaphase with a 13 % higher asymmetry, in telophase the median values are very similar and the heterogenous distribution prevents any significance. Furthermore, HeLa ezr$^{-/-}$ KO cells expressing GFP- ezrin and those expressing GFP N-ERMAD show no perfect symmetry. This could be physiological in the HeLa ezr$^{-/-}$ KO cell line. Another possibility could be an uneven distribution of the DNA construct in HeLa ezr$^{-/-}$ KO cells and subsequently a polarization favoring asymmetrical division as was shown for moesin [277].
In terms of the chromosomal positioning, HeLa ezr$^{-/-}$ KO cells transfected with GFP-N-ERMAD present chromosomes closer to the cortex than HeLa ezr$^{-/-}$ KO cells transfected with GFP-ezrin, but no respectively larger distances to the equator for the N-ERMAD condition. Additionally, the extreme values of cortex-to-chromosomes distances solely appear after the transfection with GFP-N-ERMAD.
These results can be added to those of Carreno et al. [43]. In Drosophila in metaphase they found asymmetrical and shorter spindle lengths in dmoesin depleted cells and the spindles were off center in 90 % of the cells. Spindle length differences can lead to differences in the distance chromosomes-to-cortex and the distance chromosome-to-equator. As the starting point of metaphase is less clear, in this thesis the anaphase and telophase are analyzed and can be seen as a subsequent development of the metaphase knowledge. Thus the reducation of the chromosomal distance to the cortex in HeLa ezr$^{-/-}$ KO cells expressing GFP N-ERMAD could be explained by the findings about spindles by Carreno et al. [43]. However the observed chromosome segregations did not show an increased asymmetry compared to HeLa ezr$^{-/-}$ KO cells transfected with GFP-ezrin. Now different explanations are possible: 1) HeLa ezr$^{-/-}$ KO cells expressing GFP-ezrin possess all three ERMs while Drosophila only has dmoesin. So different roles concerning the cell lines could

be imaginable. 2) Carreno et al. used 25 cells for this specific analysis, while this thesis uses different numbers for each condition. Gaining the same amount of divisions per condition would enhance the validity of comparisons and would enable the ANOVA statistical test. Furthermore, the heterogenous distribution of the values implies a high number of values for any statistical test. 3) Only one clone of the CRISPR/Cas generated HeLa ezr$^{-/-}$ KO cell line could be used in this thesis. Therefore, any difference could be due to clonal selection.
Further investigations concluding the discovered dmoesin structure which preceeds spindle formation [250] would be interesting for morphological insights in mitosis.

5.4 Conclusion

The current study analyzes the distribution and possible role of ERM proteins in cell division. I could show that no cells with an increased DNA content result in ERM depletion. This confirms the observations of the literature [359]. Furthermore I was able to prove an accelerating role of ERMs in the progression of cytokinesis. This finding contradicts recent studies in HeLa cells [342], where only live cell microscopy was used, whereas this work is based on flow cytometry, a more suitable method. However in 2008 a delayed anaphase onset in Drosophila melanogaster upon SLIK or dmoesin depletion was described [43]. There they were satisfied with a one-time only examination of up to 172 fixed cells under the microscope. Thus, my work provides the first statistically significant proof of a delayed anaphase onset in HeLa cells, by assessing the kinetics of mitosis with flow cytometry. Additionally this work detected cortical instabilities in mitosis upon GFP N-ERMAD expression in HeLa ezr$^{-/-}$ KO cells such as blebs and morphological alterations were shown. Blebs have already been described upon ERM downregulation [43, 341]. Local softening of the cortex at the poles enables the cellular elongation in anaphase [341]. The dominant negative situation with N-ERMAD overexpression could that way globally soften the cortex. Furthermore, this thesis discovered a morphological shortening of the distance between the chromosomes and the cortex upon GFP N-ERMAD expression. Distances have not been discussed before. However the positioning of chromosomes was assessed by analyzing spindles in mitosis [43]. Spindles were shown to be affected upon dmoesin depletion. Furthermore, a structure of non-phosphorylated dmoesin was shown to locally preceed spindle formation [250]. Thus, this thesis provides additional arguments to further assess the positioning of non-phosphorylatable mutants of ERMs in mammalian cells, and if a structure such as for dmoesin appears, analyzing its kinetics in live cell microscopy.
That way two promising paths remain as a perspective:
1) If the progression in cytokinesis includes a mechanism implicating ERMs and this

mechanism is based on cortical interactions, the role of Eps8 combined with ERMs should be targeted. Eps8 localizes to the cleavage furrow [247] and an interaction with ezrin for the reestablishment of the cortex in retracting blebs has been reported [188]. Thus it is possible that the enlargment of the equatorial cortex also dilutes the Rnd3 concentration and is thereby perceived by a cell as a bleb. This would also explain the stronger effect of ERMs in furrow ingression after anillin and supervillin depletion [342]. As first steps further studies should check for a colocalization of Eps8 and ezrin, and then analyze possible interactions.

2) If the progression in cytokinesis includes a mechanism implicating ERMs and this mechanism is based on spindle organization and positioning, this study verifies morphological alterations upon ERM depletion. Therefore further studies should deal with the dmoesin structure discovered by Vilmos et al. [250] by assessing the positioning of non-phosphorylatable mutants of ERMs in mammalian cells. Furthermore, the proposed interaction between ERMs and MYOGEF by Jiao [193], could be interesting, as MYOGEF was shown to concentrate at the spindle pole and the central spindle during mitosis, where it contributes to the spatiotemporal regulation of cytokinesis [360].

6 References

1. Sato, N, Funayama, N, Nagafuchi, A, Yonemura, S, and Tsukita, S. A gene family consisting of ezrin, radixin and moesin. Its specific localization at actin filament/plasma membrane association sites. Journal of Cell Science 1992;103:131–143.
2. Algrain, M, Turunen, O, Vaheri, A, Louvard, D, and Arpin, M. Ezrin contains cytoskeleton and membrane binding domains accounting for its proposed role as a membrane-cytoskeletal linker. Journal of Cell Biology 1993;1:129–139.
3. Rouleau, G, Merel, P, Lutchman, M, et al. Alteration in a new gene encoding a putative membrane-organizing protein causes neuro-fibromatosis type 2. Nature 1993;363:515–521.
4. Trofatter, J, MacCollin, M, Rutter, J, et al. A novel moesin-, ezrin-, radixin-like gene is a candidate for the neurofibromatosis 2 tumor suppressor. Cell 1993;72:791–800.
5. Gould, K, Bretscher, A, Esch, F, and Hunter, T. cDNA cloning and sequencing of the protein-tyrosine kinase substrate, ezrin, reveals homology to band 4.1. EMBO Journal 1989;8:4133–4142.
6. Lankes, F and Furthmayr, H. Moesin: a member of the protein 4.1-talin-ezrin family of proteins. Proceedings of the National Academy of Sciences of the United States of America 1991;19:8297–8301.
7. Funayama, N, Nagafuchi, A, Sato, N, Tsukita, S, and Tsukita, S. Radixin is a novel member of the band 4.1 family. Journal of Cell Biology 1991;4:1039–1048.
8. Bretscher, A. Purification of an 80,000-dalton protein that is a component of the isolated microvillus cytoskeleton. Journal of Cell Biology 1983;97:425–432.
9. Tsukita, S, Hieda, Y, and Tsukita, S. A new 82-kD barbed end-capping protein (radixin) localized in the cell-to-cell adherens junction: purification and characterization. Journal of Cell Biology 1989;108:2369–2382.
10. Turunen, O, Wahlstroem, T, and Vaheri, A. Ezrin has a COOH-terminal actin-binding site that is conserved in the ezrin protein family. Journal of Cell Biology 1994;6:1445–1453.
11. Li, Q, Nance, M, Kulikauskas, R, et al. Self-masking in an intact ERM-merlin protein: an active role for the central α-helical domain. Journal of Molecular Biology 2007;5:1446–1459.

12. Bretscher, A, Edwards, K, and Fehon, RG. ERM proteins and merlin: integrators at the cell cortex. Nature Reviews Molecular Cell Biology 2002;3:586–599.

13. Pearson, MA, Reczek, D, Bretscher, A, and Karplus, PA. Structure of the ERM protein moesin reveals the FERM domain fold masked by an extended actin binding tail domain. Cell 2000;101:259–270.

14. Smith, WJ, Nassar, N, Bretscher, A, Cerione, RA, and Karplus, PA. Structure of the active N-terminal domain of ezrin. Conformational and mobility changes identify keystone interactions. Journal of Biological Chemistry 2003:4949–4956.

15. Vijay-Kumar, S, Bugg, CE, and Cook, WJ. Structure of ubiquitin refined at 1.8Å resolution. Journal of Molecular Biology 1987;194:531–544.

16. Kragelund, BB, Andersen, KV, Madsen, JC, Knudsen, J, and Poulsen, FM. Three-dimensional structure of the complex between acyl-coenzyme A binding protein and palmitoyl-coenzyme A. Journal of Molecular Biology 1993;230:1260–1277.

17. Forman-Kaya, JD and Pawson, T. Diversity in protein recognition by PTB domains. Current Opinion in Structural Biology 1999;9:690–695.

18. Niggli, V, Andréoli, C, Roy, C, and Mangeat, P. Identification of a phosphatidyl inositol-4,5-bisphosphate-binding domain in the N-terminal region of ezrin. FEBS Letters 1995;376:172–176.

19. Gary, R and Bretscher, A. Ezrin self-association involves binding of an N-terminal domain to a normally masked C-terminal domain that includes the F-actin binding site. Molecular Biology of the Cell 1995;6:1061–1075.

20. Nakamura, F, Amieva, MR, and Furthmayr, H. Phosphorylation of Threonine 558 in the carboxyl-terminal actin-binding domain of moesin by thrombin activation of human platelets. Journal of Biological Chemistry 1995;270:31377–31385.

21. Matsui, T, Maeda, M, Doi, Y, et al. Rho-kinase phosphorylates COOH-terminal Threonines of ezrin/radixin/moesin (ERM) proteins and regulates their head-to-tail association. Journal of Cell Biology 1998;140:647–657.

22. Gary, R and Bretscher, A. Heterotypic and homotypic associations between ezrin and moesin, two putative membrane-cytoskeletal linking proteins. Proceedings of the National Academy of Sciences of the United States of America 1993;90:10846–10850.

23. Andreoli, C, Martin, M, Le Borgne, R, Reggio, H, and Mangeat, P. Ezrin has properties to self-associate at the plasma membrane. Journal of Cell Science 1994;107:2509–2521.

24. Jayaraman, B and Nicholson, LK. Thermodynamic dissection of the ezrin FERM/CERMAD interface. Biochemistry 2007;46:12174–12189.

25. Kawaguchi, K, Yoshida, S, Hatano, R, and Asano, S. Pathophysiological roles of ezrin/radixin/moesin proteins. Biological and Pharmaceutical Bulletin 2017;40:381–390.

26. Yonemura, S, Matsui, T, Tsukita, S, and Tsukita, S. Rho-dependent and -independent activation mechanisms of ezrin/radixin/moesin proteins: an essential role for polyphosphoinositides in vivo. Journal of Cell Science 2002;115:2569–2580.

27. Fievet, B, Gautreau, A, Roy, C, et al. Phosphoinositide binding and phosphorylation act sequentially in the activation mechanism of ezrin. Journal of Cell Biology 2004;164:653–659.

28. Hirao, M, Sato, N, Kondo, T, et al. Regulation mechanism of ERM (ezrin/ radixin/ moesin) protein/plasma membrane association: possible involvement of phosphatidylinositol turnover and Rho-dependent signaling pathway. Journal of Cell Biology 1996;135:37–51.

29. Solinet, S, Mahmud, K, Stewman, SF, et al. The actin-binding ERM protein moesin binds to and stabilizes microtubules at the cell cortex. Journal of Cell Biology 2013;202:251–260.

30. Fritzsche, M, Thorogate, R, and Charras, G. Quantitative analysis of ezrin turnover dynamics in the actin cortex. Biophysical Journal 2014;106:343–353.

31. Ng, T, Parsons, M, Hughes, WE, et al. Ezrin is a downstream effector of trafficking PKC–integrin complexes involved in the control of cell motility. EMBO Journal 2001;20:2723–2741.

32. Simons, PC, Pietromonaco, SF, Reczek, D, Bretscher, A, and Elias, L. C-terminal Threonine phosphorylation activates ERM proteins to link the cell's cortical lipid bilayer to the cytoskeleton. Biochemical and Biophysical Research Communications 1998;253:561–565.

33. Klooster, J ten, Jansen, M, Yuan, J, et al. Mst4 and ezrin induce brush borders downstream of the Lkb1/Strad/Mo25 polarization complex. Developmental Cell 2009;16:551–562.

34. Belkina, N, Liu, Y, Hao, JJ, Karasuyama, H, and Shaw, S. LOK is a major ERM kinase in resting lymphocytes and regulates cytoskeletal rearrangement through ERM phosphorylation. Proceedings of the National Academy of Sciences of the United States of America 2009;106:4707–4712.

35. Ivetic, A and Ridley, A. Ezrin/radixin/moesin proteins and Rho GTPase signalling in leucocytes. Immunology 2004;112:425–432.

36. Hori, Y, Kikuchi, A, Isomura, M, et al. Post-translational modifications of the C-terminal region of the rho protein are important for its interaction with membranes and the stimulatory and inhibitory GDP/GTP exchange proteins. Oncogene 1991;6:515–522.

37. Takahashi, K, Sasaki, T, Mammoto, A, et al. Direct interaction of the Rho GDP dissociation inhibitor with ezrin/radixin/moesin initiates the activation of the Rho small G protein. Journal of Biological Chemistry 1997;272:23371–23375.

38. Takahashi, K, Sasaki, T, Mammoto, A, et al. Interaction of radixin with Rho small G protein GDP/GTP exchange protein Dbl. Oncogene 1998;16:3279–3284.

39. Dransfield, DT, Bradford, AJ, Smith, J, et al. Ezrin is a cyclic AMP-dependent protein kinase anchoring protein. EMBO Journal 1997;16:35–43.

40. Yang, HS and Hinds, PW. Increased ezrin expression and activation by CDK5 coincident with acquisition of the senescent phenotype. Molecular Cell 2003;11:1163–1176.

41. Krieg, J and Hunter, T. Identification of the two major epidermal growth factor-induced tyrosine phosphorylation sites in the microvillar core protein ezrin. Journal of Biological Chemistry 1992;267:19258–19265.

42. Parameswaran, N, Enyindah-Asonye, G, Bagheri, N, Shah, NB, and Gupta, N. Spatial coupling of JNK activation to the B cell antigen receptor by Tyrosine-phosphorylated ezrin. Journal of Immunology 2013;190:2017–2026.

43. Carreno, S, Kouranti, I, Glusman, ES, Fuller, MT, Echard, A, and Payre, F. Moesin and its activating kinase Slik are required for cortical stability and microtubule organization in mitotic cells. Journal of Cell Biology 2008;180:739–746.

44. Kunda, P, Pelling, AE, Liu, T, and Baum, B. Moesin controls cortical rigidity, cell rounding, and spindle morphogenesis during mitosis. Current Biology 2008;18:91–101.

45. Hipfner, DR, Keller, N, and Cohen, SM. Slik Sterile-20 kinase regulates Moesin activity to promote epithelial integrity during tissue growth. Genes & Development 2004;18:2243–2248.

46. Hughes, S and Fehon, R. Phosphorylation and activity of the tumor suppressor Merlin and the ERM protein Moesin are coordinately regulated by the Slik kinase. Journal of Cell Biology 2006;175:305–313.

47. Speck, O, Hughes, SC, Noren, NK, Kulikauskas, RM, and Fehon, RG. Moesin functions antagonistically to the Rho pathway to maintain epithelial integrity. Nature 2003;421:83–87.

48. Chambers, DN and Bretscher, A. Ezrin mutants affecting dimerization and activation. Biochemistry 2005;44:3926–3932.

49. Fehon, R, McClatchey, A, and A.Bretscher. Organizing the cell cortex: the role of ERM proteins. Nature reviews Molecular cell biology 2010;11:267–287.

50. Yonemura, S, Hirao, M, Doi, Y, et al. Ezrin/radixin/moesin (ERM) proteins bind to a positively charged amino acid cluster in the juxta-membrane cytoplasmic domain of CD44, CD43, and ICAM-2. Journal of Cell Biology 1998;140:885–895.

51. Denker, SP, Huang, DC, Orlowski, J, Furthmayr, H, and Barber, DL. Direct binding of the Na–H exchanger NHE1 to ERM proteins regulates the cortical cytoskeleton and cell shape independently of H^+ translocation. Molecular Cell 2000;6:1425–1436.

52. Reczek, D, Berryman, M, and Bretscher, A. Identification of EBP50: a PDZ-containing phosphoprotein that associates with members of the ezrin-radixin-moesin family. Journal of Cell Biology 1997;139:169–179.

53. Weinman, E, Steplock, D, Wang, Y, and Shenolikar, S. Characterization of a protein cofactor that mediates protein kinase A regulation of the renal brush border membrane Na^+-H^+ exchanger. Journal of Clinical Investigation 1995;95:2143–2149.

54. Reczek, D and Bretscher, A. The carboxyl-terminal region of EBP50 binds to a site in the amino-terminal domain of ezrin that is masked in the dormant molecule. Journal of Biological Chemistry 1998;273:18452–18458.

55. Murthy, A, Gonzalez-Agosti, C, Cordero, E, et al. NHE-RF, a regulatory cofactor for Na^+-H^+exchange, is a common interactor for merlin and ERM (MERM) proteins. Journal of Biological Chemistry 1998;273:1273–1276.

56. Takeda, T. Podocyte cytoskeleton is connected to the integral membrane protein podocalyxin through Na^+/H^+-exchanger regulatory factor 2 and ezrin. Journal of Clinical and Experimental Nephrology 2003;7:260–269.

57. Hall, RA, Ostedgaard, LS, Premont, RT, et al. A C-terminal motif found in the β2-adrenergic receptor, P2Y1 receptor and cystic fibrosis transmembrane conductance regulator determines binding to the Na^+/H^+ exchanger regulatory factor family of PDZ proteins. Proceedings of the National Academy of Sciences 1998;95:8496–8501.

58. Short, DB, Trotter, KW, Reczek, D, et al. An apical PDZ protein anchors the cystic fibrosis transmembrane conductance regulator to the cytoskeleton. Journal of Biological Chemistry 1998;273:19797–19801.

59. Cheng, H, Li, J, Fazlieva, R, Dai, Z, Bu, Z, and Roder, H. Autoinhibitory interactions between the PDZ2 and C-terminal domains in the scaffolding protein NHERF1. Structure 2009;17:660–669.

60. Morales, FC, Takahashi, Y, Momin, S, Adams, H, Chen, X, and Georgescu, MM. NHERF1/EBP50 head-to-tail intramolecular interaction masks association with PDZ domain ligands. Molecular and Cellular Biology 2007;27:2527–2537.

61. Berryman, M, Franck, Z, and Bretscher, A. Ezrin is concentrated in the apical microvilli of a wide variety of epithelial cells whereas moesin is found primarily in endothelial cells. Journal of Cell Science 1993;105:1025–1043.

62. Amieva, MR and Furthmayr, H. Subcellular localization of moesin in dynamic filopodia, retraction fibers, and other structures involved in substrate exploration, attachment, and cell-cell contacts. Experimental Cell Research 1995;219:180–196.

63. Sato, N, Yonemura, S, Obinata, T, Tsukita, S, and Tsukita, S. Radixin, a barbed end-capping actin-modulating protein, is concentrated at the cleavage furrow during cytokinesis. Journal of Cell Biology 1991;113:321–330.

64. Millard, TH and Martin, P. Dynamic analysis of filopodial interactions during the zippering phase of Drosophila dorsal closure. Development 2008;135:621–626.

65. McClatchey, AI and Fehon, RG. Merlin and the ERM proteins – regulators of receptor distribution and signaling at the cell cortex. Trends in Cell Biology 2009;19:198–206.

66. McCartney, BM and Fehon, RG. Distinct cellular and subcellular patterns of expression imply distinct functions for the Drosophila homologues of moesin and the neurofibromatosis 2 tumor suppressor, merlin. Journal of Cell Biology 1996;133:843–852.

67. Ingraffea, J, Reczek, D, and Bretscher, A. Distinct cell type-specific expression of scaffolding proteins EBP50 and E3KARP: EBP50 is generally expressed with ezrin in specific epithelia, whereas E3KARP is not. European Journal of Cell Biology 2002;81:61–68.

68. Bonilha, VL, Rayborn, ME, Saotome, I, McClatchey, AI, and Hollyfield, JG. Microvilli defects in retinas of ezrin knockout mice. Experimental Eye Research 2006;82:720–729.

69. Tamura, A, Kikuchi, S, Hata, M, et al. Achlorhydria by ezrin knockdown. Journal of Cell Biology 2005;169:21–28.

70. Hatano, R, Fujii, E, Segawa, H, et al. Ezrin, a membrane cytoskeletal cross-linker, is essential for the regulation of phosphate and calcium homeostasis. Kidney International 2013;83:41–49.

71. Hatano, R, Akiyama, K, Tamura, A, et al. Knockdown of ezrin causes intrahepatic cholestasis by the dysregulation of bile fluidity in the bile duct epithelium in mice. Hepatology 2015;61:1660–1671.

72. Hanzel, DK, Urushidani, T, Usinger, WR, Smolka, A, and Forte, JG. Immunological localization of an 80-kDa phosphoprotein to the apical membrane of gastric parietal cells. American Journal of Physiology-Gastrointestinal and Liver Physiology 1989;256:G1082–G1089.

73. Ding, X, Deng, H, Wang, D, et al. Phospho-regulated ACAP4-ezrin interaction is essential for Histamine-stimulated parietal cell secretion. Journal of Biological Chemistry 2010;285:18769–18780.

74. Brown, MJ, Nijhara, R, Hallam, JA, et al. Chemokine stimulation of human peripheral blood T lymphocytes induces rapid dephosphorylation of ERM proteins, which facilitates loss of microvilli and polarization. Blood 2003;102:3890–3899.

75. Hirata, T, Nomachi, A, Tohya, K, et al. Moesin-deficient mice reveal a non-redundant role for moesin in lymphocyte homeostasis. International Immunology 2012;24:705–717.

76. Liu, X, Yang, T, Suzuki, K, et al. Moesin and myosin phosphatase confine neutrophil orientation in a chemotactic gradient. Journal of Experimental Medicine 2015;212:267–280.

77. Amieva, MR, Wilgenbus, KK, and Furthmayr, H. Radixin is a component of hepatocyte microvilli in situ. Experimental Cell Research 1994;210:140–144.

78. Okayama, T, Kikuchi, S, Ochiai, T, et al. Attenuated response to liver injury in moesin-deficient mice: impaired stellate cell migration and decreased fibrosis. Biochimica et Biophysica Acta (BBA) - Molecular Basis of Disease 2008;1782:542–548.

79. Kitajiri, Si, Fukumoto, K, Hata, M, et al. Radixin deficiency causes deafness associated with progressive degeneration of cochlear stereocilia. Journal of Cell Biology 2004;166:559–570.

80. Loebrich, S, Bähring, R, Katsuno, T, Tsukita, S, and Kneussel, M. Activated radixin is essential for GABA$_A$ receptor $\alpha5$ subunit anchoring at the actin cytoskeleton. EMBO Journal 2006;25:987–999.

81. Hausrat, TJ, Muhia, M, Gerrow, K, et al. Radixin regulates synaptic GABA$_A$ receptor density and is essential for reversal learning and short-term memory. Nature Communications 2015.

82. Hirate, Y and Sasaki, H. The role of angiomotin phosphorylation in the Hippo pathway during preimplantation mouse development. Tissue Barriers 2014;2:e28127.

83. Hirate, Y, Hirahara, S, Inoue, Ki, et al. Polarity-dependent distribution of Angiomotin localizes Hippo signaling in preimplantation embryos. Current Biology 2013;23:1181–1194.

84. Campanale, JP, Sun, TY, and Montell, DJ. Development and dynamics of cell polarity at a glance. Journal of Cell Science 2017;130:1201–1207.

85. Mast, SO. Structure, movement, locomotion, and stimulation in amoeba. Journal of Morphology 1926;41:347–425.

86. Apgar, JR, Herrmann, SH, Robinson, JM, and Mescher, MF. Triton X-100 extraction of P815 tumor cells: evidence for a plasma membrane skeleton structure. Journal of Cell Biology 1985;100:1369–1378.

87. Pollard, T and Ito, S. Cytoplasmic filaments of amoeba proteus: the role of filaments in consistency changes and movement. Journal of Cell Biology 1970;46:267–289.

88. Comly, LT. Microfilaments in chaos carolinensis. Membrane association, distribution and heavy meromyosin binding in the glycerinated cell. Journal of Cell Biology 1970;58:230–237.

89. Morone, N, Fujiwara, T, Murase, K, et al. Three-dimensional reconstruction of the membrane skeleton at the plasma membrane interface by electron tomography. Journal of Cell Biology 2006;174:851–862.

90. Charras, G, Hu, CK, Coughlin, M, and Mitchison, T. Reassembly of contractile actin cortex in cell blebs. Journal of Cell Biology 2006;175:477–490.

91. Small, J, Auinger, S, Nemethova, M, et al. Unravelling the structure of the lamellipodium. Journal of Microscopy 2008;231:479–485.

92. Bovellan, M, Romeo, Y, Biro, M, et al. Cellular control of cortical actin nucleation. Current Biology 2014;24:1628–1635.

93. Fritzsche, M, Erlenkämper, C, Moeendarbary, E, Charras, G, and Kruse, K. Actin kinetics shapes cortical network structure and mechanics. Science Advances 2016;2:e1501337–e1501337.

94. Fritzsche, M, Li, D, Colin-York, H, et al. Self-organizing actin patterns shape membrane architecture but not cell mechanics. Nature Communications 2017;8:14347.

95. Kushner, DJ. Self-assembly of biological structures. Bacteriological Reviews 1969;33:302–345.

96. Nicolis, G and Prigogine, I. Self-organization in nonequilibrium Systems. From dissipative structures to order through fluctuations. Berichte der Bunsengesellschaft für physikalische Chemie 1978;82:672–672.

97. Misteli, T. The concept of self-organization in cellular architecture. Journal of Cell Biology 2001;155:181–186.

98. Hannezo, E, Dong, B, Recho, P, Joanny, JF, and Hayashi, S. Cortical instability drives periodic supracellular actin pattern formation in epithelial tubes. Proceedings of the National Academy of Sciences 2015;112:8620–8625.

99. Tan, TH, Garbi, MM, Abu-Shah, E, et al. Self-organization of stress patterns drives state transitions in actin cortices. Science Advances 2018;4:eaar2847.

100. Kruse, K, Joanny, JF, Jülicher, F, Prost, J, and Sekimoto, K. Asters, vortices, and rotating spirals in active gels of polar filaments. Physical Review Letters 2004;92:078101.

101. Murthy, K and Wadsworth, P. Myosin-II-dependent localization and dynamics of F-actin during cytokinesis. Current Biology 2005;15:724–731.

102. Wilson, CA, Tsuchida, MA, Allen, GM, et al. Myosin II contributes to cell-scale actin network treadmilling through network disassembly. Nature 2010;465:373–377.

103. Mukhina, S, Wang, Yl, and Murata-Hori, M. α-actinin is required for tightly regulated remodeling of the actin cortical network during cytokinesis. Developmental Cell 2007;13:554–565.

104. Tinevez, JY, Schulze, U, Salbreux, G, Roensch, J, Joanny, JF, and Paluch, E. Role of cortical tension in bleb growth. Proceedings of the National Academy of Sciences 2009;106:18581–18586.

105. Uehara, R, Goshima, G, Mabuchi, I, Vale, RD, Spudich, JA, and Griffis, ER. Determinants of myosin II cortical localization during cytokinesis. Current Biology 2010;20:1080–1085.

106. Wottawah, F, Schinkinger, S, Lincoln, B, et al. Optical rheology of biological cells. Physical Review Letters 2005;94:098103.

107. Fritzsche, M, Lewalle, A, Duke, T, Kruse, K, and Charras, G. Analysis of turnover dynamics of the submembranous actin cortex. Molecular Biology of the Cell 2013;24:757–767.

108. Bray, D and White, J. Cortical flow in animal cells. Science 1988;239:883–888.

109. Salbreux, G, Charras, G, and Paluch, E. Actin cortex mechanics and cellular morphogenesis. Trends in Cell Biology 2012;22:536–545.

110. Stewart, MP, Helenius, J, Subramanian P. Ramanathan, YT and, Muller, DJ, and Hyman, AA. Hydrostatic pressure and the actomyosin cortex drive mitotic cell rounding. Nature 2011;469:226–230.

111. Pollard, T and Cooper, J. Actin and actin-binding proteins. A critical evaluation of mechanisms and functions. Annual Review of Biochemistry 1986;55:987–1035.

112. Hartwig, JH, Chambers, KA, and Stossel, TP. Association of gelsolin with actin filaments and cell membranes of macrophages and platelets. Journal of Cell Biology 1989;108:467–479.

113. Wuestehube, LJ and Luna, EJ. F-actin binds to the cytoplasmic surface of ponticulin, a 17-kD integral glycoprotein from Dictyostelium discoideum plasma membranes. Journal of Cell Biology 1987;105:1741–1751.

114. Verkhovsky, AB and Borisy, GG. Non-sarcomeric mode of myosin II organization in the fibroblast lamellum. Journal of Cell Biology 1993;123:637–652.

115. Svitkina, TM, Verkhovsky, AB, McQuade, KM, and Borisy, GG. Analysis of the actin–myosin II system in fish epidermal keratocytes: mechanism of cell body translocation. Journal of Cell Biology 1997;139:397–415.

116. Bridgman, PC. Growth cones contain myosin II bipolar filament arrays. Cell Motility and the Cytoskeleton 2002;52:91–96.

117. Stendahl, OI and Stossel, TP. Actin-binding protein amplifies actomyosin contraction, and gelsolin confers calcium control on the direction of contraction. Biochemical and Biophysical Research Communications 1980;92:675–681.

118. Janson, LW, Kolega, J, and Taylor, DL. Modulation of contraction by gelation/solation in a reconstituted motile model. Journal of Cell Biology 1991;114:1005–1015.

119. Janson, LW and Taylor, DL. In vitro models of tail contraction and cytoplasmic streaming in amoeboid cells. Journal of Cell Biology 1993;123:345–356.

120. Kane, RE. Interconversion of structural and contractile actin gels by insertion of myosin during assembly. Journal of Cell Biology 1983;97:1745–1752.

121. Carlsson, AE. Contractile stress generation by actomyosin gels. Physical Review E 2006;74:051912.

122. Bendix, PM, Koenderink, GH, Cuvelier, D, et al. A quantitative analysis of contractility in active cytoskeletal protein networks. Biophysical Journal 2008;94:3126–3136.

123. Koenderink, GH, Dogic, Z, Nakamura, F, et al. An active biopolymer network controlled by molecular motors. Proceedings of the National Academy of Sciences 2009;106:15192–15197.

124. MacKintosh, FC and Schmidt, CF. Active cellular materials. Current Opinion in Cell Biology 2010;22:29–35.

125. Gardel, ML, Shin, JH, MacKintosh, FC, Mahadevan, L, Matsudaira, P, and Weitz, DA. Elastic behavior of cross-linked and bundled actin networks. Science 2004;304:1301–1305.

126. Gardel, ML, Nakamura, F, Hartwig, JH, Crocker, JC, Stossel, TP, and Weitz, DA. Prestressed F-actin networks cross-linked by hinged filamins replicate mechanical properties of cells. Proceedings of the National Academy of Sciences of the United States of America 2006;103:1762–1767.

127. Sato, M, Schwarz, WH, and Pollard, TD. Dependence of the mechanical properties of actin/α-actinin gels on deformation rate. Nature 1987;325:828–830.

128. Humphrey, D, Duggan, C, Saha, D, Smith, D, and Kas, J. Active fluidization of polymer networks through molecular motors. Nature 2002;416:413–416.

129. Lieleg, O, Claessens, MMAE, Luan, Y, and Bausch, AR. Transient binding and dissipation in cross-linked actin networks. Physical Review Letters 2008;101:108101–4.

130. Sellers, JR. Myosins: a diverse superfamily. Biochimica et Biophysica Acta (BBA) - Molecular Cell Research 2000;1496:3–22.

131. Whittaker, M, Wilson-Kubalek, EM, Smith, JE, Faust, L, Milligan, RA, and Sweeney, HL. A 35-A movement of smooth muscle myosin on ADP release. Nature 1995;378:748–751.

132. Houdusse, A and Sweeney, HL. How myosin generates force on actin filaments. Trends in Biochemical Sciences 2016;41:989–997.

133. Niederman, R and Pollard, TD. Human platelet myosin. II. In vitro assembly and structure of myosin filaments. Journal of Cell Biology 1975;67:72–92.

134. Mahajan, RK and Pardee, JD. Assembly mechanism of Dictyostelium myosin II: regulation by K^+, Mg^{2+} and actin filaments. Biochemistry 1996;35:15504–15514.

135. Moussavi, RS, Kelley, CA, and Adelstein, RS. Phosphorylation of vertebrate nonmuscle and smooth muscle myosin heavy chains and light chains. Molecular and Cellular Biochemistry 1993;127:219–227.

136. Matsumura, F. Regulation of myosin II during cytokinesis in higher eukaryotes. Trends in Cell Biology 2005;15:371–377.

137. Craig, R, Smith, R, and Kendrick-Jones, J. Light-chain phosphorylation controls the conformation of vertebrate non-muscle and smooth muscle myosin molecules. Nature 1983;302:436–439.

138. Jung, H, Komatsu, S, Ikebe, M, and Craig, R. Head–head and head–tail interaction: a general mechanism for switching off myosin II activity in cells. Molecular Biology of the Cell 2008;19:3234–3242.

139. Yumura, S, Ueda, M, Sako, Y, Kitanishi-Yumura, T, and Yanagida, T. Multiple mechanisms for accumulation of myosin II filaments at the equator during cytokinesis. Traffic 2008;9:2089–2099.

140. Murakami, N, Chauhan, VPS, and Elzinga, M. Two nonmuscle myosin II heavy chain isoforms expressed in rabbit brains: filament forming properties, the effects of phosphorylation by protein kinase C and casein kinase II, and location of the phosphorylation sites. Biochemistry 1998;37:1989–2003.

141. Murakami, N, Kotula, L, and Hwang, YW. Two distinct mechanisms for regulation of nonmuscle myosin assembly via the heavy chain: phosphorylation for MIIB and Mts 1 binding for MIIA. Biochemistry 2000;39:11441–11451.

142. Rosenberg, M and Ravid, S. Protein kinase C γ regulates myosin IIB phosphorylation, cellular localization, and filament assembly. Molecular Biology of the Cell 2006;17:1364–1374.

143. Abercrombie, M, Heaysman, JE, and Pegrum, SM. The locomotion of fibroblasts in culture I. Movements of the leading edge. Experimental Cell Research 1970;59:393–398.

144. Lauffenburger, DA and Horwitz, AF. Cell migration: a physically integrated molecular process. Cell 1996;84:359–369.

145. Naumanen, P, Lappalainen, P, and Hotulainen, P. Mechanisms of actin stress fibre assembly. Journal of Microscopy 2008;231:446–454.

146. Pellegrin, S and Mellor, H. Actin stress fibres. Journal of Cell Science 2007;120:3491–3499.

147. Cramer, LP, Siebert, M, and Mitchison, TJ. Identification of novel graded polarity actin filament bundles in locomoting heart fibroblasts: implications for the generation of motile force. Journal of Cell Biology 1997;136:1287–1305.

148. Lazarides, E and Burridge, K. α-Actinin: immunofluorescent localization of a muscle structural protein in nonmuscle cells. Cell 1975;6:289–298.

149. Weber, K and Groeschel-Stewart, U. Antibody to myosin: the specific visualization of myosin-containing filaments in nonmuscle cells. Proceedings of the National Academy of Sciences of the United States of America 1974;71:4561–4564.

150. Lazarides, E. Tropomyosin antibody: the specific localization of tropomyosin in nonmuscle cells. Journal of Cell Biology 1975;65:549–561.

151. Ridley, AJ and Hall, A. The small GTP-binding protein rho regulates the assembly of focal adhesions and actin stress fibers in response to growth factors. Cell 1992;70:389–399.

152. Leung, T, Chen, XQ, Manser, E, and Lim, L. The p160 RhoA-binding kinase ROK alpha is a member of a kinase family and is involved in the reorganization of the cytoskeleton. Molecular and Cellular Biology 1996;16:5313–5327.

153. Kumar, S, Maxwell, IZ, Heisterkamp, A, et al. Viscoelastic retraction of single living stress fibers and its impact on cell shape, cytoskeletal organization, and extracellular matrix mechanics. Biophysical Journal 2006;90:3762–3773.

154. Levayer, R and Lecuit, T. Biomechanical regulation of contractility: spatial control and dynamics. Trends in Cell Biology 2012;22:61–81.

155. Watanabe, N, Kato, T, Fujita, A, Ishizaki, T, and Narumiya, S. Cooperation between mDia1 and ROCK in Rho-induced actin reorganization. Nature Cell Biology 1999;1:136–143.

156. Sixt, M. Cell migration: fibroblasts find a new way to get ahead. Journal of Cell Biology 2012;197:347–349.

157. Heath, J. Behaviour and structure of the leading lamella in moving fibroblasts. I. Occurrence and centripetal movement of arc-shaped microfilament bundles beneath the dorsal cell surface. Journal of Cell Science 1983;60:331–354.

158. Small, J, Rottner, K, Kaverina, I, and Anderson, K. Assembling an actin cytoskeleton for cell attachment and movement. Biochimica et Biophysica Acta (BBA) - Molecular Cell Research 1998;1404:271–281.

159. Zaidel-Bar, R, Cohen, M, Addadi, L, and Geiger, B. Hierarchical assembly of cell–matrix adhesion complexes. Biochemical Society Transactions 2004;32:416–420.

160. Vicente-Manzanares, M, Choi, CK, and Horwitz, AR. Integrins in cell migration – the actin connection. Journal of Cell Science 2008;122:199–206.

161. Hynes, RO. Integrins: bidirectional, allosteric signaling machines. Cell 2002;110:673–687.

162. Hotulainen, P and Lappalainen, P. Stress fibers are generated by two distinct actin assembly mechanisms in motile cells. Journal of Cell Biology 2006;173:383–394.

163. Etienne-Manneville, S, Manneville, JB, Nicholls, S, Ferenczi, MA, and Hall, A. Cdc42 and Par6–PKCζ regulate the spatially localized association of Dlg1 and APC to control cell polarization. Journal of Cell Biology 2005;170:895–901.

164. Osmani, N, Vitale, N, Borg, JP, and Etienne-Manneville, S. Scrib controls Cdc42 localization and activity to promote cell polarization during astrocyte migration. Current Biology 2006;16:2395–2405.

165. Robertson, AMG, Bird, CC, Waddell, AW, and Currie, AR. Morphological aspects of glucocorticoid-induced cell death in human lymphoblastoid cells. Journal of Pathology 1978;126:181–187.

166. Blaser, H, Reichman-Fried, M, Castanon, I, et al. Migration of zebrafish primordial germ cells: a role for myosin contraction and cytoplasmic flow. Developmental Cell 2006;11:613–627.

167. Jaglarz, M and Howard, K. The active migration of Drosophila primordial germ cells. Development 1995;121:3495–3503.

168. Zatulovskiy, E, Tyson, R, Bretschneider, T, and Kay, RR. Bleb-driven chemotaxis of Dictyostelium cells. Journal of Cell Biology 2014;204:1027–1044.

169. Tyson, RA, Zatulovskiy, E, Kay, RR, and Bretschneider, T. How blebs and pseudopods cooperate during chemotaxis. Proceedings of the National Academy of Sciences 2014;111:11703–11708.

170. Paluch, EK and Raz, E. The role and regulation of blebs in cell migration. Current Opinion in Cell Biology 2013;25:582–590.

171. Charras, G and Paluch, E. Blebs lead the way: how to migrate without lamellipodia. Nature Reviews Molecular Cell Biology 2008;9:730–736.

172. Lämmermann, T and Sixt, M. Mechanical modes of 'amoeboid' cell migration. Current Opinion in Cell Biology 2009;21:636–644.

173. Cunningham, CC. Actin polymerization and intracellular solvent flow in cell surface blebbing. Journal of Cell Biology 1995;129:1589–1599.

174. Keller, H and Eggli, P. Protrusive activity, cytoplasmic compartmentalization, and restriction rings in locomoting blebbing Walker carcinosarcoma cells are related to detachment of cortical actin from the plasma membrane. Cell Motility and the Cytoskeleton 1998;41:181–193.

175. Paluch, E, Piel, M, Prost, J, Bornens, M, and Sykes, C. Cortical actomyosin breakage triggers shape oscillations in cells and cell fragments. Biophysical Journal 2005;89:724–733.

176. Sheetz, MP, Sable, JE, and Döbereiner, HG. Continuous membrane-cytoskeleton adhesion requires continuous accommodation to lipid and cytoskeleton dynamics. Annual Review of Biophysics and Biomolecular Structure 2006;35:417–434.

177. Merkel, R, Simson, R, Simson, DA, et al. A micromechanic study of cell polarity and plasma membrane cell body coupling in Dictyostelium. Biophysical Journal 2000;79:707–719.

178. Boulbitch, A, Simson, R, Simson, DA, et al. Shape instability of a biomembrane driven by a local softening of the underlying actin cortex. Physical Review E 2000;62:3974–3985.

179. Estecha, A, Sánchez-Martín, L, Puig-Kröger, A, et al. Moesin orchestrates cortical polarity of melanoma tumour cells to initiate 3D invasion. Journal of Cell Science 2009;122:3492–3501.

180. Goudarzi, M, Banisch, TU, Mobin, MB, et al. Identification and regulation of a molecular module for bleb-based cell motility. Developmental Cell 2012;23:210–218.

181. Terayama, K, Kataoka, K, Morichika, K, Orii, H, Watanabe, K, and Mochii, M. Developmental regulation of locomotive activity in Xenopus primordial germ cells. Development, Growth & Differentiation 2013;55:217–228.

182. Charras, GT, Yarrow, JC, Horton, MA, Mahadevan, L, and Mitchison, TJ. Non-equilibration of hydrostatic pressure in blebbing cells. Nature 2005;435:365–369.

183. Charras, G. A short history of blebbing. Journal of Microscopy 2008;231:466–478.

184. Zwaenepoel, I, Naba, A, Menezes Lyra Da Cunha, M, et al. Ezrin regulates microvillus morphogenesis by promoting distinct activities of Eps8 proteins. Molecular Biology of the Cell 2012;23:1080–1095.

185. Logue, JS, Cartagena-Rivera, AX, Baird, MA, Davidson, MW, Chadwick, RS, and Waterman, CM. Erk regulation of actin capping and bundling by Eps8 promotes cortex tension and leader bleb-based migration. eLife 2015;4:e08314.

186. Croce, A, Cassata, G, Disanza, A, et al. A novel actin barbed-end-capping activity in Eps-8 regulates apical morphogenesis in intestinal cells of Caenorhabditis elegans. Nature Cell Biology 2004;6:1173–1179.

187. Disanza, A, Carlier, MF, Stradal, TEB, et al. Eps8 controls actin-based motility by capping the barbed ends of actin filaments. Nature Cell Biology 2004;6:1180–1188.

188. Aoki, K, Maeda, F, Nagasako, T, Mochizuki, Y, Uchida, S, and Ikenouchi, J. A RhoA and Rnd3 cycle regulates actin reassembly during membrane blebbing. Proceedings of the National Academy of Sciences 2016;113:E1863–E1871.

189. Chardin, P. Function and regulation of Rnd proteins. Nature Reviews Molecular Cell Biology 2006;7:54–62.

190. Riou, P, Kjær, S, Garg, R, et al. 14-3-3 proteins interact with a hybrid prenyl-phosphorylation motif to inhibit G proteins. Cell 2013;153:640–653.

191. Wennerberg, K, Forget, MA, Ellerbroek, SM, et al. Rnd Proteins Function as RhoA Antagonists by Activating p190 RhoGAP. Current Biology 2003;13:1106–1115.

192. Ikenouchi, J and Aoki, K. Membrane bleb: a seesaw game of two small GTPases. Small GTPases 2017;8:85–89.

193. Jiao, M, Wu, D, Wei, Q, and Blanchoin, L. Myosin II–interacting guanine nucleotide exchange factor promotes bleb retraction via stimulating cortex reassembly at the bleb membrane. Molecular Biology of the Cell 2018;29:643–656.

194. Diz-Muñoz, A, Krieg, M, Bergert, M, et al. Control of directed cell migration in vivo by membrane-to-cortex attachment. PLOS Biology 2010;8:1–12.

195. Poincloux, R, Collin, O, Lizárraga, F, et al. Contractility of the cell rear drives invasion of breast tumor cells in 3D Matrigel. Proceedings of the National Academy of Sciences 2011;108:1943–1948.

196. Petrie, RJ, Gavara, N, Chadwick, RS, and Yamada, KM. Nonpolarized signaling reveals two distinct modes of 3D cell migration. Journal of Cell Biology 2012;197:439–455.

197. Harris, TJC and Tepass, U. Adherens junctions: from molecules to morphogenesis. Nature Reviews Molecular Cell Biology 2010;11:502–514.

198. Rodriguez-Boulan, E and Macara, IG. Organization and execution of the epithelial polarity programme. Nature Reviews Molecular Cell Biology 2014;15:225–242.

199. Harris, TJ and Peifer, M. The positioning and segregation of apical cues during epithelial polarity establishment in Drosophila. Journal of Cell Biology 2005;170:813–823.

200. Benton, R and Johnston, DS. Drosophila PAR-1 and 14-3-3 inhibit Bazooka/PAR-3 to establish complementary cortical domains in polarized cells. Cell 2003;115:691–704.

201. Jiang, T, David, DJV, and Harris, TJC. Cell polarity 1: biological role and basic mechanisms. Chapter Epithelial apicobasal polarity in the Drosophila embryo. In: ed. by Ebnet, K. Springer International Publishing Switzerland, 2015:167–187.

202. Stein, W von, Ramrath, A, Grimm, A, Müller-Borg, M, and Wodarz, A. Direct association of Bazooka/PAR-3 with the lipid phosphatase PTEN reveals a link between the PAR/aPKC complex and phosphoinositide signaling. Development 2005;132:1675–1686.

203. Martin-Belmonte, F, Gassama, A, Datta, A, et al. PTEN-mediated apical segregation of phosphoinositides controls epithelial morphogenesis through Cdc42. Cell 2007;128:383–397.

204. Bilder, D, Schober, M, and Perrimon, N. Integrated activity of PDZ protein complexes regulates epithelial polarity. Nature Cell Biology 2003;5:53–58.

205. Tanentzapf, G and Tepass, U. Interactions between the crumbs, lethal giant larvae and bazooka pathways in epithelial polarization. Nature Cell Biology 2002;5:46–52.

206. Sauvanet, C, Wayt, J, Pelaseyed, T, and Bretscher, A. Structure, regulation, and functional diversity of microvilli on the apical domain of epithelial cells. Annual Review of Cell and Developmental Biology 2015;31:593–621.

207. Bretscher, A. Molecular architecture of the microvillus cytoskeleton. 1983;95:164–179.

208. Bretscher, A. Rapid phosphorylation and reorganization of ezrin and spectrin accompany morphological changes induced in A-431 cells by epidermal growth factor. Journal of Cell Biology 1989;108:921–930.

209. Bretscher, A and Weber, K. Purification of microvilli and an analysis of the protein components of the microfilament core bundle. Experimental Cell Research 1978;116:397–407.

210. Bartles, JR, Zheng, L, Li, A, Wierda, A, and Chen, B. Small espin: a third actin-bundling protein and potential forked protein ortholog in brush border microvilli. Journal of Cell Biology 1998;143:107–119.

211. Bretscher, A and Weber, K. Villin: the major microfilament-associated protein of the intestinal microvillus. Proceedings of the National Academy of Sciences of the United States of America 1979;76:2321–2325.

212. Bretscher, A and Weber, K. Fimbrin, a new microfilament-associated protein present in microvilli and other cell surface structures. Journal of Cell Biology 1980;86:335–340.

213. Ahuja, R, Pinyol, R, Reichenbach, N, et al. Cordon-Bleu is an actin nucleation factor and controls neuronal morphology. Cell 2007;131:337–350.

214. Husson, C, Renault, L, Didry, D, Pantaloni, D, and Carlier, MF. Cordon-Bleu uses WH2 domains as multifunctional dynamizers of actin filament assembly. Molecular Cell 2011;43:464–477.

215. Chen, T, Hubbard, A, Murtazina, R, et al. Myosin VI mediates the movement of NHE3 down the microvillus in intestinal epithelial cells. Journal of Cell Science 2014;127:3535–3545.

216. Kravtsov, DV, Caputo, C, Collaco, A, et al. Myosin Ia is required for CFTR brush border membrane trafficking and ion transport in the mouse small intestine. Traffic 2012;13:1072–1082.

217. Viswanatha, R, Ohouo, PY, Smolka, MB, and Bretscher, A. Local phosphocycling mediated by LOK/SLK restricts ezrin function to the apical aspect of epithelial cells. Journal of Cell Biology 2012;199:969–984.

218. Rhind, N and Russell, P. Signaling pathways that regulate cell division. Cold Spring Harbor Perspectives in Biology 2012;4.

219. Wieser, S and Pines, J. The biochemistry of mitosis. Cold Spring Harbor Perspectives in Biology 2015;7.

220. Gavet, O and Pines, J. Activation of cyclin B1–Cdk1 synchronizes events in the nucleus and the cytoplasm at mitosis. Journal of Cell Biology 2010;189:247–259.

221. Santos, SD, Wollman, R, Meyer, T, and Ferrell, JE. Spatial positive feedback at the onset of mitosis. Cell 2012;149:1500–1513.

222. Gavet, O and Pines, J. Progressive activation of cyclinB1-Cdk1 coordinates entry to mitosis. Developmental Cell 2010;18:533–543.

223. Matthews, HK, Delabre, U, Rohn, JL, Guck, J, Kunda, P, and Baum, B. Changes in Ect2 localization couple actomyosin-dependent cell shape changes to mitotic progression. Developmental Cell 2012;23:371–383.

224. Champion, L, Linder, MI, and Kutay, U. Cellular reorganization during mitotic entry. Trends in Cell Biology 2017;27:26–41.

225. Ramanathan, SP, Helenius, J, Stewart, MP, Cattin, CJ, Hyman, AA, and Muller, DJ. Cdk1-dependent mitotic enrichment of cortical myosin II promotes cell rounding against confinement. Nature Cell Biology 2015;17:148–159.

226. Son, S, Kang, JH, Oh, S, Kirschner, MW, Mitchison, T, and Manalis, S. Resonant microchannel volume and mass measurements show that suspended cells swell during mitosis. Journal of Cell Biology 2015;211:757–763.

227. Zlotek-Zlotkiewicz, E, Monnier, S, Cappello, G, Le Berre, M, and Piel, M. Optical volume and mass measurements show that mammalian cells swell during mitosis. Journal of Cell Biology 2015;211:765–774.

228. Dao, VT, Dupuy, AG, Gavet, O, Caron, E, and Gunzburg, J de. Dynamic changes in Rap1 activity are required for cell retraction and spreading during mitosis. Journal of Cell Science 2009;122:2996–3004.

229. Lafuente, EM, Puijenbroek, AA van, Krause, M, et al. RIAM, an Ena/VASP and Profilin ligand, interacts with Rap1-GTP and mediates Rap1-induced adhesion. Developmental Cell 2004;7:585–595.

230. Lee, HS, Lim, CJ, Puzon-McLaughlin, W, Shattil, SJ, and Ginsberg, MH. RIAM activates integrins by linking talin to Ras GTPase membrane-targeting sequences. Journal of Biological Chemistry 2009;284:5119–5127.

231. Lancaster, OM, Berre, ML, Dimitracopoulos, A, et al. Mitotic rounding alters cell geometry to ensure efficient bipolar spindle formation. Developmental Cell 2013;25:270–283.

232. Lancaster, OM and Baum, B. Shaping up to divide: coordinating actin and microtubule cytoskeletal remodelling during mitosis. Seminars in Cell & Developmental Biology 2014;34:109–115.

233. Cadart, C, Zlotek-Zlotkiewicz, E, Berre, ML, Piel, M, and Matthews, HK. Exploring the function of cell shape and size during mitosis. Developmental Cell 2014;29:159–169.

234. Marchesi, S, Montani, F, Deflorian, G, et al. DEPDC1B coordinates deadhesion events and cell-cycle progression at mitosis. Developmental Cell 2014;31:420–433.

235. Nicassio, F, Bianchi, F, Capra, M, et al. A cancer-specific transcriptional signature in human neoplasia. Journal of Clinical Investigation 2005;115:3015–3025.

236. Cramer, LP and Mitchison, TJ. Investigation of the mechanism of retraction of the cell margin and rearward flow of nodules during mitotic cell rounding. Molecular Biology of the Cell 1997;8:109–119.

237. Maddox, AS and Burridge, K. RhoA is required for cortical retraction and rigidity during mitotic cell rounding. Journal of Cell Biology 2003;160:255–265.

238. Rosenblatt, J, Cramer, LP, Baum, B, and McGee, KM. Myosin II-dependent cortical movement is required for centrosome separation and positioning during mitotic spindle assembly. Cell 2004;117:361–372.

239. Cattin, CJ, Düggelin, M, Martinez-Martin, D, Gerber, C, Müller, DJ, and Stewart, MP. Mechanical control of mitotic progression in single animal cells. Proceedings of the National Academy of Sciences 2015;112:11258–11263.

240. Tatsumoto, T, Xie, X, Blumenthal, R, Okamoto, I, and Miki, T. Human Ect2 is an exchange factor for Rho Gtpases, phosphorylated in G2/M phases, and involved in cytokinesis. Journal of Cell Biology 1999;147:921–928.

241. Niiya, F, Tatsumoto, T, Lee, KS, and Miki, T. Phosphorylation of the cytokinesis regulator ECT2 at G2//M phase stimulates association of the mitotic kinase Plk1 and accumulation of GTP-bound RhoA. Oncogene 2005;25:827–837.

242. Oceguera-Yanez, F, Kimura, K, Yasuda, S, et al. Ect2 and MgcRacGAP regulate the activation and function of Cdc42 in mitosis. Journal of Cell Biology 2005;168:221–232.

243. Mitsushima, M, Toyoshima, F, and Nishida, E. Dual role of Cdc42 in spindle orientation control of adherent cells. Molecular and Cellular Biology 2009;29:2816–2827.

244. Machicoane, M, Frutos, CA de, Fink, J, et al. SLK-dependent activation of ERMs controls LGN–NuMA localization and spindle orientation. Journal of Cell Biology 2014;205:791–799.

245. Kunda, P and Baum, B. The actin cytoskeleton in spindle assembly and positioning. Trends in Cell Biology 2009;19:174–179.

246. Tuncay, H, Brinkmann, BF, Steinbacher, T, et al. JAM-A regulates cortical dynein localization through Cdc42 to control planar spindle orientation during mitosis. 2015;6:8128.

247. Werner, A, Disanza, A, Reifenberger, N, et al. SCF^{Fbxw5} mediates transient degradation of actin remodeler Eps8 to allow proper mitotic progression. Nature Cell Biology 2013;15:179–188.

248. Vilmos, P, Jankovics, F, Szathmári, M, Lukácsovich, T, Henn, L, and Erdélyi, M. Live imaging reveals that the Drosophila actin-binding ERM protein, moesin, co-localizes with the mitotic spindle. European Journal of Cell Biology 2009;88:609–619.

249. Thery, M, Racine, V, Pepin, A, et al. The extracellular matrix guides the orientation of the cell division axis. Nature Cell Biology 2005;7:947–953.

250. Vilmos, P, Kristó, I, Szikora, S, et al. The actin-binding ERM protein moesin directly regulates spindle assembly and function during mitosis. Cell Biology International 2016;40:696–707.

251. Polesello, C, Delon, I, Valenti, P, Ferrer, P, and Payre, F. Dmoesin controls actin-based cell shape and polarity during Drosophila melanogaster oogenesis. Nature Cell Biology 2002;4:782–789.

252. Alberts, B, Johnson, A, Lewis, J, Raff, M, Roberts, K, and Walter, P. Molecular Biology of the Cell, 4^{th} edition. New York: Garland Science, 2002:1072–1073, 1092.

253. Lacroix, B and Maddox, AS. Cytokinesis, ploidy and aneuploidy. Journal of Pathology 2012;226:338–351.

254. Rappaport, R. Experiments concerning the cleavage stimulus in sand dollar eggs. Journal of Experimental Zoology 1961;148:81–89.

255. Green, RA, Paluch, E, and Oegema, K. Cytokinesis in animal cells. Annual Review of Cell and Developmental Biology 2012;28:29–58.

256. Douglas, ME and Mishima, M. Still entangled: assembly of the central spindle by multiple microtubule modulators. Seminars in Cell & Developmental Biology 2010;21:899–908.

257. Kurasawa, Y, Earnshaw, WC, Mochizuki, Y, Dohmae, N, and Todokoro, K. Essential roles of KIF4 and its binding partner PRC1 in organized central spindle midzone formation. EMBO Journal 2004;23:3237–3248.

258. Zhu, C and Jiang, W. Cell cycle-dependent translocation of PRC1 on the spindle by Kif4 is essential for midzone formation and cytokinesis. Proceedings of the National Academy of Sciences of the United States of America 2005;102:343–348.

259. Zhu, C, Lau, E, Schwarzenbacher, R, Bossy-Wetzel, E, and Jiang, W. Spatiotemporal control of spindle midzone formation by PRC1 in human cells. Proceedings of the National Academy of Sciences 2006;103:6196–6201.

260. Nunes Bastos, R, Gandhi, SR, Baron, RD, Gruneberg, U, Nigg, EA, and Barr, FA. Aurora B suppresses microtubule dynamics and limits central spindle size by locally activating KIF4A. Journal of Cell Biology 2013;202:605–621.

261. Bieling, P, Telley, IA, and Surrey, T. A minimal midzone protein module controls formation and length of antiparallel microtubule overlaps. Cell 2010;142:420–432.

262. Subramanian, R, Wilson-Kubalek, EM, Arthur, CP, et al. Insights into antiparallel microtubule crosslinking by PRC1, a conserved nonmotor microtubule binding protein. Cell 2010;142:433–443.

263. Hu, CK, Coughlin, M, Field, CM, and Mitchison, TJ. KIF4 regulates midzone length during cytokinesis. Current Biology 2011;21:815–824.

264. Adams, RR, Tavares, AA, Salzberg, A, Bellen, HJ, and Glover, DM. pavarotti encodes a kinesin-like protein required to organize the central spindle and contractile ring for cytokinesis. Genes & Development 1998;12:1483–1494.

265. Mishima, M, Kaitna, S, and Glotzer, M. Central spindle assembly and cytokinesis require a kinesin-like protein/RhoGAP complex with microtubule bundling activity. Developmental Cell 2002;2:41–54.

266. D'Avino, PP, Savoian, MS, Capalbo, L, and Glover, DM. RacGAP50C is sufficient to signal cleavage furrow formation during cytokinesis. Journal of Cell Science 2006;119:4402–4408.

267. Douglas, ME, Davies, T, Joseph, N, and Mishima, M. Aurora B and 14-3-3 coordinately regulate clustering of centralspindlin during cytokinesis. Current Biology 2010;20:927–933.

268. Kaitna, S, Mendoza, M, Jantsch-Plunger, V, and Glotzer, M. Incenp and an Aurora-like kinase form a complex essential for chromosome segregation and efficient completion of cytokinesis. Current Biology 2000;10:1172–1181.

269. Mishima, M, Pavicic, V, Gruneberg, U, Nigg, EA, and Glotzer, M. Cell cycle regulation of central spindle assembly. Nature 2004;430:908–913.

270. Guse, A, Mishima, M, and Glotzer, M. Phosphorylation of ZEN-4/MKLP1 by Aurora B regulates completion of cytokinesis. Current Biology 2005;15:778–786.

271. Gruneberg, U, Neef, R, Honda, R, Nigg, EA, and Barr, FA. Relocation of Aurora B from centromeres to the central spindle at the metaphase to anaphase transition requires MKlp2. Journal of Cell Biology 2004;166:167–172.

272. Fuller, BG, Lampson, MA, Foley, EA, et al. Midzone activation of aurora B in anaphase produces an intracellular phosphorylation gradient. Nature 2008;453:1132–1136.

273. Glotzer, M. Cleavage furrow positioning. Journal of Cell Biology 2004;164:347–351.

274. D'Avino, PP, Savoian, MS, and Glover, DM. Cleavage furrow formation and ingression during animal cytokinesis: a microtubule legacy. Journal of Cell Science 2005;118:1549–1558.

275. Dassow, G von. Concurrent cues for cytokinetic furrow induction in animal cells. Trends in Cell Biology 2009;19:165–173.

276. Cabernard, C, Prehoda, KE, and Doe, CQ. A spindle-independent cleavage furrow positioning pathway. Nature 2010;467:91–94.

277. Abeysundara, N, Simmonds, AJ, Hughes, SC, and Fehon, R. Moesin is involved in polarity maintenance and cortical remodeling during asymmetric cell division. Molecular Biology of the Cell 2018;29:419–434.

278. Wang, Yl. The mechanism of cortical ingression during early cytokinesis: thinking beyond the contractile ring hypothesis. Trends in Cell Biology 2005;15:581–588.

279. Bement, WM, Benink, HA, and Dassow, G von. A microtubule-dependent zone of active RhoA during cleavage plane specification. Journal of Cell Biology 2005;170:91–101.

280. Piekny, A, Werner, M, and Glotzer, M. Cytokinesis: welcome to the Rho zone. Trends in Cell Biology 2005;15:651–658.

281. Jordan, SN and Canman, JC. Rho GTPases in animal cell cytokinesis: an occupation by the one percent. Cytoskeleton 2012;69:919–930.

282. Werner, M, Munro, E, and Glotzer, M. Astral signals spatially bias cortical myosin recruitment to break symmetry and promote cytokinesis. Current Biology 2007;17:1286–1297.

283. Murthy, K and Wadsworth, P. Dual role for microtubules in regulating cortical contractility during cytokinesis. Journal of Cell Science 2008;121:2350–2359.

284. Hutterer, A, Glotzer, M, and Mishima, M. Clustering of centralspindlin is essential for its accumulation to the central spindle and the midbody. Current Biology 2009;19:2043–2049.

285. Somers, WG and Saint, R. A RhoGEF and Rho family GTPase-activating protein complex links the contractile ring to cortical microtubules at the onset of cytokinesis. Developmental Cell 2003;4:29–39.

286. Yüce, Ö, Piekny, A, and Glotzer, M. An ECT2–centralspindlin complex regulates the localization and function of RhoA. Journal of Cell Biology 2005;170:571–582.

287. Lee, JS, Kamijo, K, Ohara, N, Kitamura, T, and Miki, T. MgcRacGAP regulates cortical activity through RhoA during cytokinesis. Experimental Cell Research 2004;293:275–282.

288. Zhao, Wm and Fang, G. MgcRacGAP controls the assembly of the contractile ring and the initiation of cytokinesis. Proceedings of the National Academy of Sciences of the United States of America 2005;102:13158–13163.

289. Kamijo, K, Ohara, N, Abe, M, et al. Dissecting the role of Rho-mediated signaling in contractile ring formation. Molecular Biology of the Cell 2006;17:43–55.

290. Su, KC, Takaki, T, and Petronczki, M. Targeting of the RhoGEF Ect2 to the equatorial membrane controls cleavage furrow formation during cytokinesis. Developmental Cell 2011;21:1104–1115.

291. Burkard, ME, Randall, CL, Larochelle, S, et al. Chemical genetics reveals the requirement for Polo-like kinase 1 activity in positioning RhoA and triggering cytokinesis in human cells. Proceedings of the National Academy of Sciences 2007;104:4383–4388.

292. Burkard, ME, Maciejowski, J, Rodriguez-Bravo, V, et al. Plk1 self-organization and priming phosphorylation of HsCYK-4 at the spindle midzone regulate the onset of division in human cells. PLOS Biology 2009;7:1–16.

293. Petronczki, M, Glotzer, M, Kraut, N, and Peters, JM. Polo-like kinase 1 triggers the initiation of cytokinesis in human cells by promoting recruitment of the RhoGEF Ect2 to the central spindle. Developmental Cell 2007;12:713–725.

294. Wolfe, BA, Takaki, T, Petronczki, M, and Glotzer, M. Polo-like kinase 1 directs assembly of the HsCyk-4 RhoGAP/Ect2 RhoGEF complex to initiate cleavage furrow formation. PLOS Biology 2009;7:1–15.

295. D'Avino, PP, Savoian, MS, and Glover, DM. Mutations in sticky lead to defective organization of the contractile ring during cytokinesis and are enhanced by Rho and suppressed by Rac. Journal of Cell Biology 2004;166:61–71.

296. Canman, JC, Lewellyn, L, Laband, K, et al. Inhibition of Rac by the GAP activity of centralspindlin is essential for cytokinesis. Science 2008;322:1543–1546.

297. D'Avino, PP, Giansanti, MG, and Petronczki, M. Cytokinesis in animal cells. Cold Spring Harbor Perspectives in Biology 2015;7.

298. Madaule, P, Furuyashiki, T, Reid, T, et al. A novel partner for the GTP-bound forms of rho and rac. FEBS Letters 1995;377:243–248.

299. Bassi, ZI, Verbrugghe, KJ, Capalbo, L, et al. Sticky/Citron kinase maintains proper RhoA localization at the cleavage site during cytokinesis. Journal of Cell Biology 2011;195:595–603.

300. Paolo D'Avino, P. How to scaffold the contractile ring for a safe cytokinesis – lessons from Anillin-related proteins. Journal of Cell Science 2009;122:1071–1079.

301. Gai, M, Camera, P, Dema, A, et al. Citron kinase controls abscission through RhoA and anillin. Molecular Biology of the Cell 2011;22:3768–3778.

302. Liu, J, Fairn, GD, Ceccarelli, DF, Sicheri, F, and Wilde, A. Cleavage furrow organization requires PIP_2-mediated recruitment of anillin. Current Biology 2012;22:64–69.

303. Field, CM, Coughlin, M, Doberstein, S, Marty, T, and Sullivan, W. Characterization of anillin mutants reveals essential roles in septin localization and plasma membrane integrity. Development 2005;132:2849–2860.

304. Oh, Y and Bi, E. Septin structure and function in yeast and beyond. Trends in Cell Biology 2011;21:141–148.

305. Joo, E, Surka, MC, and Trimble, WS. Mammalian SEPT2 is required for scaffolding nonmuscle myosin II and its kinases. Developmental Cell 2007;13:677–690.

306. Hickson, GR and O'Farrell, PH. Rho-dependent control of anillin behavior during cytokinesis. Journal of Cell Biology 2008;180:285–294.

307. Neto, H, Collins, L, and Gould, G. Vesicle trafficking and membrane remodelling in cytokinesis. Biochemical Journal 2011;437:13–24.

308. McKay, HF and Burgess, DR. 'Life is a highway': membrane trafficking during cytokinesis. Traffic 2011;12:247–251.

309. Gromley, A, Yeaman, C, Rosa, J, et al. Centriolin anchoring of exocyst and SNARE complexes at the midbody is required for secretory-vesicle-mediated abscission. Cell 2005;123:75–87.

310. Goss, JW and Toomre, DK. Both daughter cells traffic and exocytose membrane at the cleavage furrow during mammalian cytokinesis. Journal of Cell Biology 2008;181:1047–1054.

311. Albertson, R, Cao, J, Hsieh, Ts, and Sullivan, W. Vesicles and actin are targeted to the cleavage furrow via furrow microtubules and the central spindle. Journal of Cell Biology 2008;181:777–790.

312. Montagnac, G, Echard, A, and Chavrier, P. Endocytic traffic in animal cell cytokinesis. Current Opinion in Cell Biology 2008;20:454–461.

313. Schiel, JA and Prekeris, R. Membrane dynamics during cytokinesis. Current Opinion in Cell Biology 2013;25:92–98.

314. Szafer-Glusman, E, Giansanti, MG, Nishihama, R, et al. A role for very-long-chain fatty acids in furrow ingression during cytokinesis in Drosophila spermatocytes. Current Biology 2008;18:1426–1431.

315. Takeda, T, Robinson, IM, Savoian, MM, et al. Drosophila F-BAR protein Syndapin contributes to coupling the plasma membrane and contractile ring in cytokinesis. Open Biology 2013;3.

316. Mullins, J and Biesele, J. Terminal phase of cytokinesis in D-98S cells. Journal of Cell Biology 1977;73:672–684.

317. Hu, CK, Coughlin, M, and Mitchison, TJ. Midbody assembly and its regulation during cytokinesis. Molecular Biology of the Cell 2012;23:1024–1034.

318. Elia, N, Sougrat, R, Spurlin, TA, Hurley, JH, and Lippincott-Schwartz, J. Dynamics of endosomal sorting complex required for transport (ESCRT) machinery during cytokinesis and its role in abscission. Proceedings of the National Academy of Sciences 2011;108:4846–4851.

319. Kechad, A, Jananji, S, Ruella, Y, and Hickson, GR. Anillin acts as a bifunctional linker coordinating midbody ring biogenesis during cytokinesis. Current Biology 2012;22:197–203.

320. Madaule, P, Eda, M, Watanabe, N, et al. Role of citron kinase as a target of the small GTPase Rho in cytokinesis. Nature 1998;394:491–494.

321. Echard, A, Hickson, G, Foley, E, and O'Farrell, P. Terminal cytokinesis events uncovered after an RNAi screen. Current biology 2004;14:1685–1693.

322. Somma, MP, Fasulo, B, Cenci, G, Cundari, E, and Gatti, M. Molecular dissection of cytokinesis by RNA interference in Drosophila cultured cells. Molecular Biology of the Cell 2002;13:2448–2460.

323. Piekny, AJ and Maddox, AS. The myriad roles of Anillin during cytokinesis. Seminars in Cell & Developmental Biology 2010;21:881–891.

324. Caballe, A and Martin-Serrano, J. ESCRT machinery and cytokinesis: the road to daughter cell separation. Traffic 2011;12:1318–1326.

325. Henne, WM, Buchkovich, NJ, and Emr, SD. The ESCRT pathway. Developmental Cell 2011;21:77–91.

326. Hurley, JH and Hanson, PI. Membrane budding and scission by the ESCRT machinery: it's all in the neck. Nature Reviews Molecular Cell Biology 2010;11:556–566.

327. Morita, E. Differential requirements of mammalian ESCRTs in multivesicular body formation, virus budding and cell division. FEBS Journal 2012;279:1399–1406.

328. Lee, HH, Elia, N, Ghirlando, R, Lippincott-Schwartz, J, and Hurley, JH. Midbody targeting of the ESCRT machinery by a noncanonical coiled coil in CEP55. Science 2008;322:576–580.

329. Morita, E, Sandrin, V, Chung, HY, et al. Human ESCRT and ALIX proteins interact with proteins of the midbody and function in cytokinesis. EMBO Journal 2007;26:4215–4227.

330. Guizetti, J, Schermelleh, L, Mäntler, J, et al. Cortical constriction during abscission involves helices of ESCRT-III–dependent filaments. Science 2011;331:1616–1620.

331. Connell, JW, Lindon, C, Luzio, JP, and Reid, E. Spastin couples microtubule severing to membrane traffic in completion of cytokinesis and secretion. Traffic 2009;10:42–56.

332. Reid, E, Connell, J, Edwards, TL, Duley, S, Brown, SE, and Sanderson, CM. The hereditary spastic paraplegia protein spastin interacts with the ESCRT-III complex-associated endosomal protein CHMP1B. Human Molecular Genetics 2005;14:19–38.

333. Yang, D, Rismanchi, N, Renvoise, B, Lippincott-Schwartz, J, Blackstone, C, and Hurley, JH. Structural basis for midbody targeting of spastin by the ESCRT-III protein CHMP1B. Nature Structural & Molecular Biology 2008;15:1278–1286.

334. Bastos, RN and Barr, FA. Plk1 negatively regulates Cep55 recruitment to the midbody to ensure orderly abscission. Journal of Cell Biology 2010;191:751–760.

335. Fabbro, M, Zhou, BB, Takahashi, M, et al. Cdk1/Erk2- and Plk1-dependent phosphorylation of a centrosome protein, Cep55, is required for its recruitment to midbody and cytokinesis. Developmental Cell 2005;9:477–488.

336. Zhao, Wm, Seki, A, and Fang, G. Cep55, a microtubule-bundling protein, associates with centralspindlin to control the midbody integrity and cell abscission during cytokinesis. Molecular Biology of the Cell 2006;17:3881–3896.

337. Capalbo, L, Montembault, E, Takeda, T, Bassi, ZI, Glover, DM, and D'Avino, PP. The chromosomal passenger complex controls the function of endosomal sorting complex required for transport-III Snf7 proteins during cytokinesis. Open Biology 2012;2.

338. Carlton, JG, Caballe, A, Agromayor, M, Kloc, M, and Martin-Serrano, J. ESCRT-III governs the Aurora B–mediated abscission checkpoint through CHMP4C. Science 2012;336:220–225.

339. Roubinet, C, Decelle, B, Chicanne, G, et al. Molecular networks linked by Moesin drive remodeling of the cell cortex during mitosis. Journal of Cell Biology 2011;195:99–112.

340. Luxenburg, C, Amalia Pasolli, H, Williams, SE, and Fuchs, E. Developmental roles for Srf, cortical cytoskeleton and cell shape in epidermal spindle orientation. Nature Cell Biology 2011;13:203–214.

341. Rodrigues, NTL, Lekomtsev, S, Jananji, S, Kriston-Vizi, J, Hickson, GRX, and Baum, B. Kinetochore-localized PP1-Sds22 couples chromosome segregation to polar relaxation. Nature 2015;524:489.

342. Hiruma, S, Kamasaki, T, Otomo, K, Nemoto, T, and Uehara, R. Dynamics and function of ERM proteins during cytokinesis in human cells. FEBS Letters 2017;591:3296–3309.

343. Yonemura, S, Nagafuchi, A, Sato, N, and Tsukita, S. Concentration of an integral membrane protein, CD43 (leukosialin, sialophorin), in the cleavage furrow through the interaction of its cytoplasmic domain with actin-based cytoskeletons. Journal of Cell Biology 1993;120:437–449.

344. Heil, A. Neue Interaktionen des IQGAP1 Proteins. Dissertation. Westfälische Wilhelms-Universität Münster, 2010.

345. Barret, C, Roy, C, Montcourrier, P, Mangeat, P, and Niggli, V. Mutagenesis of the phosphatidylinositol 4,5-bisphosphate (Pip2) binding site in the Nh2-terminal domain of ezrin correlates with its altered cellular distribution. Journal of Cell Biology 2000;151:1067–1080.

346. Laemmli, BUK. Cleavage of structural proteins during assembly of head of bacteriophage-T4. Nature 1970;227:680–5.

347. Schägger, H and Von Jagow, G. Tricine-sodium dodecyl sulfate-polyacrylamide gel electrophoresis for the separation of proteins in the range from 1 to 100 kDa. Analytical biochemistry 1987;166:368–379.

348. Bass, JJ, Wilkinson, DJ, Rankin, D, et al. An overview of technical considerations for Western blotting applications to physiological research. Scandinavian Journal of Medicine and Science in Sports 2017;27:4–25.

349. Renart, J, Reiser, J, and Stark, G. Transfer of proteins from gels to diazobenzyl oxymethyl-paper and detection with antisera: a method for studying antibody specificity and antigen structure. Proceedings of the National Academy of Sciences of the United States of America 1979;76:3116–3120.

350. Burnette, W. Western Blotting: electrophoretic transfer of proteins from sodium dodecyl sulfate-polyacrylamide gels to unmodified nitrocellulose and radiographic detection with antibody and radioiodinated protein A. Analytical Biochemistry 1981;112:195–203.

351. Dittrich, W and Göhde, W. Automatisches Meß- und Zählgerät für die Teilchen einer Dispersion. Patent DE 1815352A1 I (DE). 1971.

352. Gasnereau, I, Ganier, O, Bourgain, F, Gramont, Ad, Gendron, MC, and Sobczak-Thépot, J. Flow cytometry to sort mammalian cells in cytokinesis. Cytometry Part A 2007;71A:1–7.

353. Glass, GV, Peckham, PD, and Sanders, JR. Consequences of failure to meet assumptions underlying the fixed effects analyses of variance and covariance. Review of Educational Research 1972;42:237–288.

354. Harwell, MR, Rubinstein, EN, Hayes, WS, and Olds, CC. Summarizing Monte Carlo results in methodological research: the one- and two-factor fixed effects ANOVA cases. Journal of Educational Statistics 1992;17:315–339.

355. Lix, LM, Keselman, JC, and Keselman, HJ. Consequences of assumption violations revisited: a quantitative review of alternatives to the one-way analysis of variance "F" test. Review of Educational Research 1996;66:579–619.

356. Charif, R, Granotier-Beckers, C, Bertrand, HC, et al. Association of a platinum complex to a G-quadruplex ligand enhances telomere disruption. Chemical Research in Toxicology 2017;30:1629–1640.

357. Wang, Q, Kieffer-Kwon, KR, Oliveira, TY, et al. The cell cycle restricts activation-induced cytidine deaminase activity to early G1. Journal of Experimental Medicine 2017;214:49–58.

358. Jacobberger, JW, Frisa, PS, Sramkoski, RM, Stefan, T, Shults, KE, and Soni, DV. A new biomarker for mitotic cells. Cytometry Part A 2008;73A:5–15.

359. Takeuchi, K, Sato, N, Kasahara, H, et al. Perturbation of cell adhesion and microvilli formation by antisense oligonucleotides to ERM family members. Journal of Cell Biology 1994;125:1371–1384.

360. Asiedu, M, Wu, D, Matsumura, F, Wei, Q, and Chang, F. Centrosome/spindle pole–associated protein regulates cytokinesis via promoting the recruitment of MyoGEF to the central spindle. Molecular Biology of the Cell 2009;20:1428–1440.

7 Curriculum Vitae

8 Acknowledgement

Finally I would like to thank all those people who made this thesis possible and an unforgettable experience for me.

First of all, I would like to express my very sincere gratitude to Prof. Dr.Volker Gerke for giving me the opportunity to undertake this work and to gather a look into research life under his supervision.

I am indebted and express my respect to Dr.Rathangadhara Chakrapani Nammalwar for guiding my first steps in research and for his endless patience. Further, I would like to thank Anna Lívia Linard Matos and David Grill for their support and help. The good laboratory atmosphere these three achieved together with Frauke Brinkmann contributed substantially to the quality of this thesis.

I am grateful and express thanks to Dr.Matthias Borowski from the IBKF (Institut für Biometrie und Klinische Forschung) for advising me on statistical methods for the analysis of the results gained by flow cytometry.

A very special gratitude goes out to Ariel Wagner-Parker for her linguistic revision.

I owe my gratitude to the Medizinerkolleg (MedK) Münster for embedding a fertile promotion program and for the financial support they granted me.

Finally, I would like to take this opportunity to express a deep sense of gratitude to my beloved parents, to whom I owe my achievements due to their constant sacrifices. Special thanks go to Sophia Maaß for making me a part of your life and believing in me much more than I do.

I am also thankful to all not mentioned persons that inspired me and crossed my path of life.

A Appendix

A.1 List of Figures

A.2 List of Tables

A.3 Abbreviations

ACAP	Arf6 Gtpase-Activating Protein
AKAP	Protein Kinase A anchoring Proteins
Arf6	ADP-ribosylation factor 6
Arp2/3	Actin-related protein 2 and 3
BCA	Bicinchoninic Acid
BCR	B-Cell Receptor
C	cytokinetic
CAK	CDK-activating kinase
CD	cluster of differenciation
Cdc42	Cell division control protein 42 homolog
CDK	Cyclin Dependant Kinase
CENP-E	Centromere-associated Protein E
Cep55	Centrosomal Protein 55
C-ERMAD	C-terminal Association Domain)
CFTR	Cystic Fibrosis Transmembrane Conductance Regulator
CHMP4C	Charged Multivesicular body Protein 4C
CIT-K	Citron Kinase
Cobl	Cordon bleu
CPC	chromosomal Passenger complex
DEPDC1B	Dishevelled, Egl-10 and Pleckstrin domain Containing Protein 1B
Dia1	Diaphanous-related formin 1
DMEM	Dulbecco's Modified Eagle Medium

dmoesin	Moesin in drosophila
DMSO	Dimethyl Sulfoxide
E.coli	Escherichia coli
E4	Elution Buffer
EBP50	ERM-binding phosphoprotein 50
Ect2	epithelial cell transforming 2
EDTA	Ethylenediaminetetraacetic Acid
EGF	Epidermal Growth Factor
Eps8	epidermal growth factor receptor pathway substrate 8
EQ1	Equilibration Buffer
ERM	Ezrin, Radixin, Moesin
ESCRT	endosomal sorting complex required for transport
EVH1	Enabled/VASP homology 1
ezr	ezrin
FACS	Fluorescence Activated Cell Sorting
F-actin	filamentous actin
FCS	Fetal Calf Serum
FERM	Four point 1, Ezrin, Radixin, Moesin
FSC	Forward SCatter
GABA	Gamma-Aminobutyric acid
G-actin	Globular actin
GEF	Guanine nucleotide Exchange Factor
HeLa	Human cervical carcinoma cell line
ICAM	Intercellular Adhesion Molecule
JAM-A	Junctional Adhesion Molecule-A
JNK	c-Jun N-terminal Kinase
KD	Knockdown
KIF	Kinesin Family
KO	Knockout
L7	Lysis Buffer
LB	Lysogeny Broth
LGN	Leucine-Glycine-Asparagine repeat protein
LOK	Lymphocyte-Orientated Kinase
M	mitotic
MAP	Microtubule-Associated Protein
merlin	moesin-ezrin-radixin-like protein
MHC	Myosin Heavy Chain
MKLP	Mitotic Kinesin-Like Protein
MLCK	Myosin Light Chain Kinase
moe	Moesin
MRCK	Myotonic dystrophy kinase-Related Cdc42-binding Kinase
MRLC	Myosin Regulatory Light Chain
Mst4	Mammalian STE20-like protein kinase 4
MT	Microtubule
MYOGEF	Myosin II-interacting guanine nucleotide exchange factor
N3	Precipitation Buffer

N-ERMAD	N-terminal Association Domain)
NHE	Na^+, H^+-exchanger
NHE-RF	NHE regulatory factor
NIK	NF-kappa-B-inducing kinase
NMR	Nuclear Magnetic Resonance
NUMA	NUclear Mitotic Apparatus
Oct4	Octamer-binding transcription factor 4
OD	Optical Density
PBS	Phosphate-Buffered Saline
PDGFR	Platelet-Derived Growth Factor Receptors
PDZ	Post synaptic density protein, Drosophila disc large tumor suppressor and Zonula occludens-1 protein
PFA	Paraformaldehyde
PH	Pleckstrin Homology
P_i	inorganic Phosphate
PI(3)K	Phosphatidylinositol-4,5-bisphosphate 3-Kinase
PIP_2	Phosphatidylinositol 4,5-bisphosphate
PIP_3	Phosphatidylinositol 3,4,5-triphosphate
PKA	Protein Kinase A
PKC	Protein Kinase C
PLK1	Polo-Like Kinase 1
PP1	Protein Phosphatase 1
PRC1	Protein Regulator of Cytokinesis 1
PTB	Phosphotyrosine Binding
PTPRF	Receptor-type tyrosine-protein phosphatase F
R3	Resuspenson Buffer
Rab	Ras-Related Protein
Rac1	Ras-related C3 botulinum toxin substrate 1
RacGAP1	Rac GTPase-activating protein 1
Rap1	Ras-related protein 1
rdx	Radixin
Rho GDI	Rho GDP dissociation inhibitor
RhoA	Ras homolog gene family, member A
Rho GAP	Rho GTPase-activating protein
RIAM	Rap1-Interacting Adhesion Molecule
Rnd3	RhoE
ROCK	Rho Kinase
Sds22	PP1 regulatory subunit Sds22
SDS-PAGE	Sodium-Dodecyl-Sulfate Polyacrylamide Gel-Electrophoresis
siERM	3 siRNAs targeting Ezrin, Radixin and Moesin
siEzr	siRNAs targeting Ezrin
siMoe	siRNAs targeting Moesin
siRdx	siRNAs targeting Radixin
siRM	2 siRNAs targeting Radixin and Moesin
SLK	Sterile 20-like Kinase
SSC	Sideward SCatter

$T_{1/2}$	Half-time
ut	untransfected
W8	Wash Buffer
WH2	Wiskott-Aldrich syndrome protein Homology 2
WT	Wildtype

Abbreviations

A.4 Amino Acide Code

Amino Acid	**3-Letter Code**	**1-Letter Code**
Alanine	Ala	A
Cysteine	Cys	C
Aspartic acid/Aspartate	Asp	D
Glutamic Acid/Glutamate	Glu	E
Phenylalanine	Phe	F
Glycine	Gly	G
Histidine	His	H
Isoleucine	Ile	I
Lysine	Lys	K
Leucine	Leu	L
Methionine	Met	M
Asparagine	Asn	N
Proline	Pro	P
Glutamine	Gln	Q
Arginine	Arg	R
Serine	Ser	S
Threonine	Thr	T
Valine	Val	V
Tryptophan	Trp	W
Tyrosine	Tyr	Y

Amino Acids